Impurity Scattering and Magnetic Field Influence on a Nodal Surface of a d-Wave Superconductor

Dissertation
der Mathematisch-Naturwissenschaftlichen Fakultät
der Eberhard-Karls-Universität Tübingen
zur Erlangung des Grades eines
Doktors der Naturwissenschaften
(Dr. rer. nat.)

vorgelegt von
Aida Zare
aus Shiraz (Iran)

Tübingen
2011

Tag der mündlichen Prüfung:	17.02.2012
Dekan:	Prof. Dr. Wolfgang Rosenstiel
1. Berichterstatter	Prof. Dr. Nils Schopohl
2. Berichterstatter	Prof. Dr. Thomas Dahm

To my parents

Zusammenfassung

In dieser Arbeit wird die Oberfläche von d-Wellen Supraleitern betrachtet. In solchen Supraleitern können gebundene Andreev-Zustände an der Oberfläche entstehen, je nach Orientierung der d-Welle relativ zur Oberflächennormalen. Diese Zustände beeinflussen die Eigenschaften des Supraleiters auf der Längenskala der Kohärenzlänge ξ_0, der Skala ihrer räumlichen Ausdehnung. Die gebundenen Zustände und damit die Eigenschaften der Oberfläche werden durch ihre Rauhigkeit, Fehlstellen, diffuse Streuung oder externe Magnetfelder beeinflußt. Streuungen an Fehlstellen im bulk des Supraleiters sorgen für eine Verbreiterung der bound states, wohingegen der mit einem externen Magnetfeld verbundene Abschirmstrom zu einer Aufspaltung der Zustände führt. Aus diesem Grund werden die Oberflächeneigenschaften für drei verschiedene Fälle betrachtet: erstens mit Störstellen, zweitens unter Einfluß eines externen Magnetfeldes und schließlich bei einer Kombination aus beidem. Die folgenden Ergebnisse basieren auf einer selbstkonsistenten Lösung der Eilenberger-Gleichungen.

Supraleiter mit Störstellen

Es wird allgemein davon ausgegangen, daß in Kuprat-Hochtemperatursupraleitern die Streuzentren in den CuO_2- Ebenen als unitäre Streuer wirken, wohingegen die Streuer zwischen den Kupferoxid-Ebenen schwach abgeschirmt werden und als Born-Streuer in Erscheinung treten. Andererseits ist bereits gezeigt worden, daß Streuung durch Störstellen im Grenzfall der Born-Näherung die Andreev-Zustände deutlich stärker verbreitert als im Grenzfall der unitären Streuung. Daher wird in dieser Arbeit der Einfluß der Streuung durch Störstellen im bulk im Grenzfall der Born-Näherung betrachtet.

Wir können die Verkleinerung des gaps im bulk bei zunehmender Verunreinigung bestätigen und beobachten darüberhinaus, daß die Supraleitung bereits zerstört wird, wenn die mittlere freie Weglänge eine ähnliche Wert wie die Kohärenzlänge erreicht. Dies bedeutet, daß es im Falle der d-Welle keinen "dirty limit" gibt. Wir zeigen weiterhin, daß die Streuung an Störstellen bei $E = 0$ nahe der Oberfläche im Vergleich zum bulk deutlich ansteigt, was auf die Andreev-Zustände zurückgeführt werden kann. Dies führt zu einer Verbreiterung der Andreev-Zustände, welche größer ist als die Streurate im bulk erwarten ließe und daher auch zu einer Abnahme des peaks in der lokalen Zustandsdichte bei $E = 0$ führt. Wir zeigen, daß das Skalierungsverhalten der Amplitude des peaks mit $\sqrt{\ell}$ skaliert, im Gegensatz zu dem Verhalten, welches in Folge der Streuung im bulk zu erwarten wäre ($\propto \ell$).

In einem isotropen s-Wellen Supraleiter gilt Andersons Theorem, welches besagt, daß die Renormier-ung des Paarpotentials durch die anomale Selbstenergie Σ^Fgenau die Renormierung durch die normale Selbstenergie Σ^Gausgleicht, so daß die Zustandsdichte

and T_c durch die Streuung an Störstellen nicht verändert werden. Dies gilt aber nicht mehr notwendigerweise in anisotropen Supraleitern. Im bulk eines d-Wellen Supraleiters verschwindet bekannterweise die anomale Selbstenergie Σ^F. Wir können zeigen, daß dies nahe der Oberfläche wegen der gebrochenen Translationsinvarianz im allgemeinen nicht gilt. Wir zeigen daß eine endliche Renomierung des Paarpotentials nahe der Oberfläche auftritt, außer wenn die Orientierung der Oberfläche hoch symmetrisch zu der Orientierung der d-Welle ist.

Elektromagnetischer response im reinen Supraleiter

Wir können den anomalen Meissner-Effekt bei entsprechender Orientiung des Paarpotentials bestätigen und zeigen, daß dieser im gesamten Temperaturbereich zwischen $0.01T_c$ und $0.9T_c$ auftritt. Durch den anomalen Meissner-Strom steigt das Magnetfeld an der Oberfläche zunächst an, bevor der normal Meissner-Abschirmeffekt überwiegt und das Magnetfeld exponentiell weggedämpft wird. Der Anstieg des Feldes fällt bei tiefen Temperaturen stärker aus und führt seinerseits zu einem Anstieg des Betrags des magnetischen Vektorpotentials. Da andererseits die Eindringtiefe nahe T_c divergiert und das magnetische Vektorpotential das Integral über das Magnetfeld ist, ist mit wachsender Eindringtiefe ebenfalls ein betragsmäßig größeres Vektorpotential zu erwarten. Diese beiden Effekte führen zu einer nichtmonotonen Abhängigkeit des Vektorpotentials an der Oberfläche von der Temperatur. Da das Vektorpotential proportional zur suprafluiden Geschwindigkeit ist, wird die Aufspaltung der peaks in der lokalen Zustandsdichte direkt durch dieses nichtmonotone Verhalten bestimmt. Die Aufspaltung ist sowohl nahe $T = 0$ als auch nahe T_c groß. Entsprechend zeigt auch die Höhe der peaks ein nichtmonotones Verhalten. Die Beobachtung eines solchen Anstiegs der Aufspaltung der peaks könnte im Experiment ein Hinweis auf das Auftreten von anomalen Meissner-Strömen sein. Allerdings nimmt dieser Effekt mit steigendem κ ab.

Die gebundenen Andreev Zustände haben auch einen bedeutenden Einfluß auf den nichtlinearen Meissner-Effekt. Der nichtlineare response-Koeffizient im bulk eines d-Wellen Supraleiters im clean limit zeigt bekanntermaßen einen Anstieg bei tiefen Temperaturen gemäß einer 1/T Abhängigkeit. Dies gilt bis zu Temperaturen von der Größenordnung von $1/\kappa$. Allerdings finden wir, daß durch die Andreev-Zustände der lineare response modifiziert wird. In Kapitel 4 zeigen wir, daß der Anteil der Andreev-Zustände an dem nichtlinearen response einer $1/T^3$ Abhängigkeit folgt, welche schließlich das $1/T$ Verhalten bei hinreichend tiefen Temperaturen im bulk dominiert. Unsere Berechnungen hierzu werden im Rahmen einer lokalen Approximation durchgeführt, welche in der Regel für $\lambda_L \gg \xi_0$ erfüllt ist.

Wir betrachten ferner die Gesamtinduktion L, eine Größe, welche in typischen Intermodulationsexperimenten gemessen wird, und zeigen, daß der Übergang von einem

Verhalten, welches vom bulk dominiert wird, zu einem Verhalten, welches von der Oberfläche bestimmt ist, bei relativ großen Temperaturen $T/T_c \propto 2.4/\sqrt{\kappa}$ stattfindet. Hier ändert sich auch das Vorzeichen des nichtlinearen Koeffizienten. Solche Temperaturen können in Intermodulationsexperimenten leicht erreicht werden. Sie bilden daher eine gute Möglichkeit zur Analyse der gebundenen Andreev-Zustände. Diese führen bei der nichtlinearen Induktion zu einer $1/T^3$ Abhängigkeit und einem Vorzeichenwechsel (einer Änderung um 180 Grad in der relativen Phase).

Um die Gültigkeit der numerischen Rechnungen zu überprüfen und ein tieferes physikalisches Verständnis zu gewinnen, entwickeln wir in Kapitel 5 ein analytisches Modell. Bei tiefen Temperaturen ergibt sich eine gute Übereinstimmung mit den numerischen Ergebnissen.

Einfluß der Streuung an Störstellen auf den elektromagnetischen response

Als nächsten Schritt betrachten wir die Born-Streuung an Störstellen unter Einfluß eines äußeren Magnetfeldes. Wir zeigen, daß die Höhe des peaks in der lokalen Zustandsdichte an der Oberfläche durch die Streurate stark verringert wird. Die Breite des peaks nimmt ebenfalls mit kleinerer mittlerer freier Weglänge zu. Allerdings ändert sich die Breite der Aufspaltung der peaks kaum. Dies liegt daran, daß durch die Aufspaltung der peaks der zur Verfügung stehen Phasenraum für Streuprozesse bei niedrigen Energieen stark abnimmt. Dies wiederum hat zur Folge, daß die Streurate der Quasiteilchen sogar bei kleinen mittleren freien Weglängen klein bleibt. Daraus ergibt sich eine Stabilisierung der peak-Aufspaltung gegenüber Streuung durch Störstellen.

Weiterhin fällt die anomale Selbsenergie unter Einfluß äußerer Magnetfeld auf Null ab, sogar für die hochsymmetrische $\alpha = \pi/4$ Orientierung. Dies hat seine Ursache darin, daß die besondere Reflexionssymetrie im Falle $\alpha = \pi/4$ durch die Richtung des Stromflusses gebrochen wird.

Contents

Chapter 1

Introduction

This work treats the surface properties of d-wave superconductors. The surface is a natural configuration to observe the *Majorana states*, which are recently coming into interest in superconductor-nonsuperconductor interface problems. We start from the general concept of Majorana states and continue with the *nodal surfaces* as an experimentally practical setup to observe such states. We first give a summary on some known results from both theoretical and experimental aspects. The effects of impurities as well as external magnetic fields at such surfaces are discussed in the forthcoming chapters (see chapters 3 and 4). It has to be emphasized that these properties are not only typical for d-wave superconductors, but for all systems showing the Majorana feature. A detailed outline of this work is given at the end of this introduction.

1.1 Majorana-Bogoliubov state

In the Bogoliubov picture of quasiparticles, it can be shown that there exist some states which are invariant under time reversal and particle-hole transformation. These states are known as Majorana states and are explained as follows. Starting from the effective Hamiltonian [1]

$$H_{\text{eff}} = \frac{1}{2}\int \mathrm{d}\boldsymbol{r}\left(\psi_\sigma^\dagger(\boldsymbol{r}), \psi_\sigma(\boldsymbol{r})\right)\mathcal{H}_{\text{BdG}}\begin{pmatrix}\psi_\sigma(\boldsymbol{r})\\ \psi_\sigma^\dagger(\boldsymbol{r})\end{pmatrix}, \tag{1.1}$$

where $\mathcal{H}_{\text{BdG}}$ is the *Bogoliubov-de Gennes* Hamiltonian:

$$\mathcal{H}_{\text{BdG}} = \begin{pmatrix} H_0 & \Delta(\boldsymbol{r}) \\ \Delta*(\boldsymbol{r}) & -H_0^* \end{pmatrix}, \tag{1.2}$$

and

$$H_0 = \frac{1}{2m}\left(-i\hbar\boldsymbol{\nabla} - \frac{e\boldsymbol{A}}{c}\right)^2 + U(\boldsymbol{r}) - \mu, \tag{1.3}$$

one obtains

$$H_{\text{eff}} = \sum_{\sigma,\varepsilon_n>0} \varepsilon_n \gamma^\dagger_{n,\sigma}\gamma_{n,\sigma}. \tag{1.4}$$

Here, ε_n is the energy of the excitation n and $\gamma^\dagger_{n,\sigma}$ is an operator which creates excited states with energy ε_n and spin σ, the so-called *quasiparticles*. This operator is a superposition of particle and hole states

$$\gamma^\dagger_{n,\sigma} = \int \mathrm{d}\boldsymbol{r} \left[u_{n,\sigma}(\boldsymbol{r})\psi^\dagger_\sigma(\boldsymbol{r}) + v_{n,-\sigma}(\boldsymbol{r})\psi_{-\sigma}(\boldsymbol{r})\right], \tag{1.5}$$

where $u_{n,\sigma}(\boldsymbol{r})$ and $v_{n,\sigma}(\boldsymbol{r})$ are the solutions of the coupled Bogoliubov-de Gennes equations

$$\mathcal{H}_{\text{BdG}} \begin{pmatrix} u_{n,\sigma}(\boldsymbol{r}) \\ v_{n,\sigma}(\boldsymbol{r}) \end{pmatrix} = \varepsilon_n \begin{pmatrix} u_{n,\sigma}(\boldsymbol{r}) \\ v_{n,\sigma}(\boldsymbol{r}) \end{pmatrix}. \tag{1.6}$$

The particle-hole symmetry of Bogoliubov-de Gennes equations implies that if $\begin{pmatrix} u_{n,\sigma} \\ v_{n,\sigma} \end{pmatrix}$ is a solution with energy ε_n, there exists always another solution $\begin{pmatrix} -v^*_{n,\sigma} \\ u^*_{n,\sigma} \end{pmatrix}$ with energy $-\varepsilon_n$ [1]. For some cases as in the vortex core or at the nodal surface, this leads to a degeneracy of the operator $\gamma_{n,\sigma}$ at the Fermi level $\varepsilon_n = 0$ [2]; the particle will be its own antiparticle. This state is known as the Majorana state.

In superconductors with nodes in the gap function, the Majorana states are present at the nodal surfaces at the Fermi level. These states which are also known as *zero-energy bound states* are fundamental for understanding the phenomena of the following chapters.

Majorana states are also discussed with regard to interface states between non-superconducting samples and superconductors. Following the work of *Sau et al.* [3], *Alicea* has recently proposed a setup in order to realize the Majorana fermions. It consist of a (110)-grown quantum well coupled to an s-wave superconductor [4]. He showed that by applying an in-plane magnetic field, the system will under certain conditions display an induced unconventional symmetry (a spin-less $p_x + ip_y$ superconductor). This setup hosts Majorana bound states.

Duckheim and *Brouwer* had also studied the spin-orbit interaction at an interface between a half metal and a superconductor [5]. They showed that for the electrons with energy less than the excitation gap, this interface becomes a spin-flip Andreev reflector and therefore, the normally reflecting boundary at the end of the half metal gives rise to a localized Majorana end state.

These states are also of interest in Josephson junctions as well as in vortex cores and in graphene [6, 7]. Contrary to the aforementioned experiments the Majorana states at the nodal surfaces are experimentally quite easy to observe.

1.2 Nodal surfaces

Considering the pairing interaction in a d-wave superconductor to have the form

$$V(\boldsymbol{p}_F, \boldsymbol{p}'_F) = \chi(\boldsymbol{p}_F)\chi(\boldsymbol{p}'_F), \tag{1.7}$$

where $\chi(\boldsymbol{p}_F)$ is a symmetry function, one can determine the pairing potential as a product of two terms, a spatial dependent term $\Delta(\boldsymbol{r}, T)$ and a momentum dependent one $\chi(\boldsymbol{p}_F)$

$$\Delta(\boldsymbol{r}, \boldsymbol{p}_F) = \Delta(\boldsymbol{r}, T)\chi(\boldsymbol{p}_F). \tag{1.8}$$

In contrast to s-wave superconductors which are isotropic, i.e. $\chi(\boldsymbol{p}_F) = 1$, the pairing potential in d-wave superconductors is orientational dependent (see figure 1.1). It leads to nodes in the pairing potential and may lead to a symmetry breaking

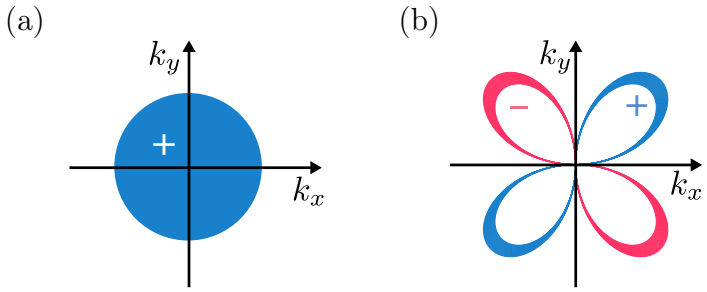

Figure 1.1: The pairing potential for (a) a conventional s-wave symmetry and (b) an unconventional d-wave symmetry. In contrast to the s-wave pairing, the d-wave symmetry is orientational dependent; it changes the sign and magnitude for different directions of the Fermi momentum.

of the surface.

Nodal surfaces are known as the surfaces perpendicular to the pairing node lines, the (110) direction in k space. At such a surface, as can be seen in figure 1.2(a), all the incident trajectories experience a sign change of the gap function after reflection. For *antinodal surfaces*, i.e. (100) direction in k space, the phase of the order parameter for the incoming and outgoing quasiparticle trajectories does not change and one obtains the bulk results (see figure 1.2(b)). For all other orientations of the surface relative to the pairing symmetry, quasiparticles experience a mixture of these two cases. In comparison with the fully nodal direction, the effect of the surface will therefore be reduced.

1.2.1 Zero-energy Andreev bound states

A direct consequence of the change in the pairing phase is the presence of zero-energy Andreev bound states at the surface. Such states exist for specific pairing orientations with respect to the surface normal [8–11].

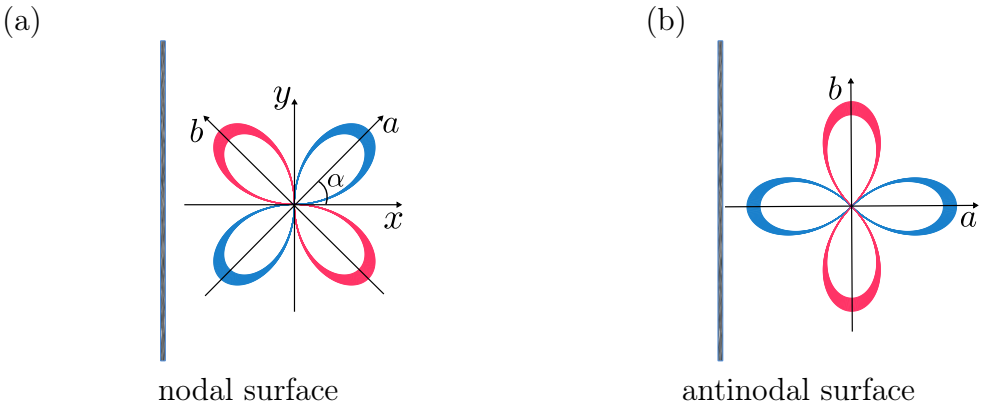

Figure 1.2: The sketch of (a) a nodal surface and (b) an antinodal surface. The trajectories reaching the nodal surface experience a sign change in the pairing potential which results in a zero energy bound states at the surface. On the other hand, for the antinodal surface with no sign change, one obtains the bulk results.

Figure 1.3, compares the local density of states at the surface of a d-wave superconductor for a nodal and an antinodal surface. Since all the trajectories at the nodal surface experience the sign change, the maximum amplitude of the surface bound states is reached. For antinodal surfaces on the other hand, one obtains the bulk results, i.e. no zero-energy bound state. These states can be observed in *scanning tunneling microscopy* experiments as *zero-bias conductance peaks* [12–16].

1.2.2 Effect of impurity scattering

The effect of impurities is one of the main topics in studying superconductivity. Lattice defects or the presence of foreign atoms in the normal metal results in a residual resistance. However it plays a different role in a superconductor. The electrons are scattered by the impurities, therefore the spatial coherence between them may decrease, resulting in a reduced pairing amplitude. Increasing the impurity concentration up to a sufficiently high amount, results in such a small coherence length that its role can be taken over by the mean free path of the electrons [17]. Furthermore, magnetic impurities can flip the spin of the electrons and therefore interfere with the pairing. This results in a reduction of the pairing amplitude [18].

Zero-energy bound states are also affected by any disorder in the superconductor. It is known that surface roughness, surface disorder, or diffuse scattering at the surface leads to a broadening of these states [19, 20]. Furthermore, bulk impurity scattering is known to have the same effect on the bound states [21, 22]. As an example, we refer to the work of *Poenicke et al.* [21], in which an angle-resolved calculation of the density of states is done at the surface of a d-wave superconductor (see figure 1.4). Using the quasiclassical theory, the results are obtained in the Born approximation with two different scattering rates $\Gamma = 0.1T_c$ and $\Gamma = 0.001T_c$.

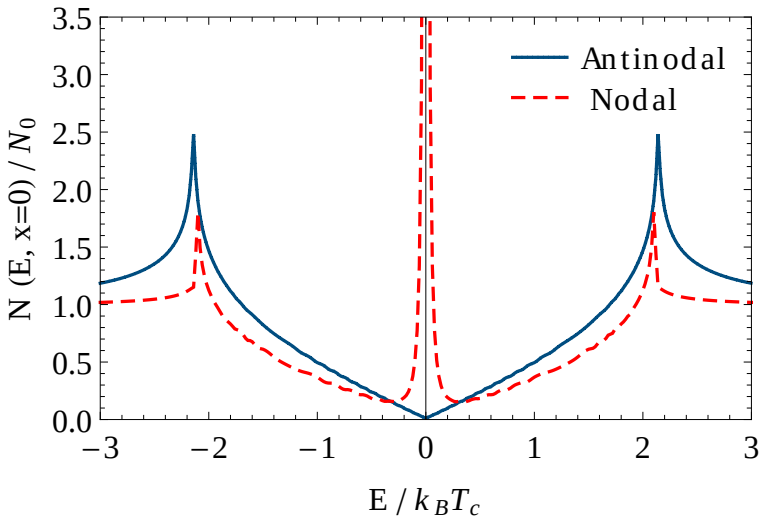

Figure 1.3: The local density of excitation states at $T = 0.1T_c$ for both a nodal and an antinodal surface. The presence of the Andreev bound states is clearly observable as a large peak at energy $E = 0$.

Broadening of the bound states due to the bulk impurities is observed for both scattering strengths, with the stronger broadening being induced by the larger scattering rate.

1.2.3 Effect of magnetic field

The Andreev bound states at the surface are occupied with phase-coherent excitations. These unpaired quasiparticles carry a collective current which exists on the length scale of the coherence length. On the other hand, in the presence of an external magnetic field, a Cooper-pair screening current flows at the surface, decaying on the length scale of the penetration length. The electromagnetic coupling between these two currents leads to a *Doppler shift* in the excitation spectrum which is given by $E \rightarrow E + \boldsymbol{p}_F \cdot \boldsymbol{v}_s$ [23–25]. Here, $\boldsymbol{p}_F$ is the momentum of the excitations and $\boldsymbol{v}_s$ is the superflow current. This means that the states carrying a current comoving the screening current will shift to higher energies, while the countermoving states will shift to lower energies. Since the states with countermoving current are energetically favorable, they will be occupied with more quasiparticles. This results in a counterflowing paramagnetic current at the surface. This current increases with decreasing temperature and for low enough temperatures may lead to a reversal of the total current flow at the surface, resulting in an *anomalous Meissner effect* [23, 26].

Such nonlinear effects are very important in studying the properties of the materials and also in practical applications. Almost all materials behave nonlinearly for certain setup parameters. The nonlinear behavior in a material can be seen for example as *harmonic generation* or *intermodulation distortion*. In the harmonic

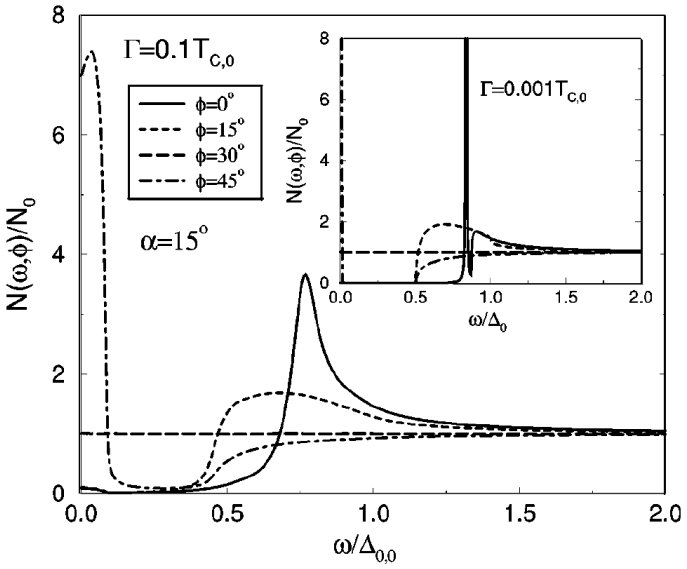

Figure 1.4: Angle-resolved local density of states at the surface of a d-wave superconductor obtained in the Born limit at the temperature $T = 0.01T_c$. One may see the broadening of the bound states in the presence of the bulk impurities. The calculations are done for two different scattering rates $\Gamma = 0.1T_c$ (main plot) and $\Gamma = 0.001T_c$ (inset), implying that increasing the scattering rate results in a larger broadening in the bound states. (Adapted from [21], Copyright © (1999) by the American Physical Society).

generation as sketched in figure 1.5(a), a nonlinear system is excited by a single signal with frequency f_1 and the nonlinear response of the system generates noises at the harmonic frequencies cf_1 where $c \in \{2, 3, \ldots\}$. The intermodulation is however a multi-signal distortion which gives rise to a nonlinear mixing of the primary signals and forming side band signals. Figure 1.5(b) shows schematically the second and third order intermodulation signals, IM2 and IM3 respectively, for a two-signal distortion with the primary signals f_1 and f_2. The IM2 products are observed at $f_1 \pm f_2$, $2f_1$ and $2f_2$, while the IM3 products are found to be at $2f_1 \pm f_2$, $f_1 \pm 2f_2$, $3f_1$ and $3f_2$. Such signals are rarely desired and therefore it may be useful to either remove them or find out when they become significant in order to avoid or reduce them. Knowing the noise frequencies, most unwanted harmonic generations or second order intermodulations can be easily eliminated by filtering methods. However, for third and higher orders, the intermodulation signals sit very close to the primary signals and are therefore not easily distinguishable. So, more accurate intermodulation measurements as well as detailed studies in order to find the onset and behavior of nonlinearities may be useful.

In unconventional superconductors, the nonlinear effects are unavoidable. They emerge as a linear magnetic field dependence of the penetration length at low tem-

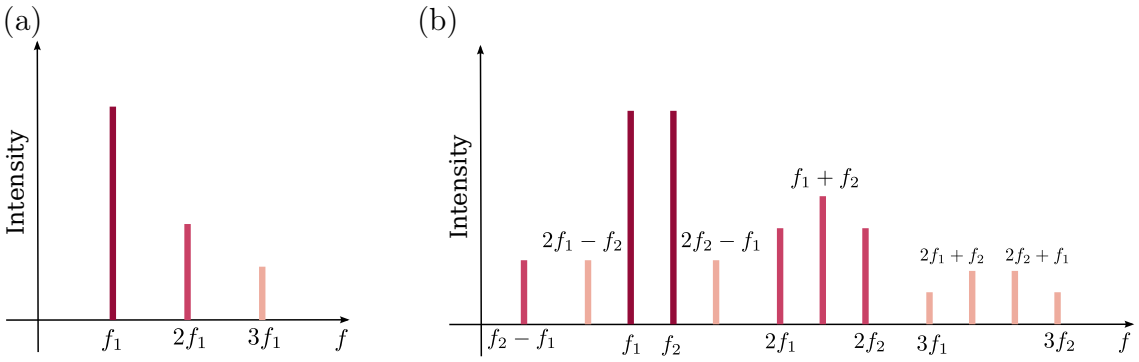

Figure 1.5: (a) Harmonic generation signals resulting from a single signal induced on a nonlinear system. The system's nonlinear responses show up at the integer multiple harmonics of the primary signal. (b) Second and third order intermodulation distortion, resulting from two primary signals f_1 and f_2 applied to a nonlinear system. The system response appears at the frequencies $f_1 \pm f_2$, $2f_1$ and $2f_2$ in the case of IM2 and at frequencies $2f_1 \pm f_2$, $f_1 \pm 2f_2$, $3f_1$ and $3f_2$ in the case of IM3.

peratures, as pointed out by *Yip* and *Sauls* [27, 28]. In order to calculate the nonlinearities, *Dahm* and *Scalapino* also suggested another method based on the temperature dependent intermodulation distortion, in which they had shown that the nonlinearity in the bulk d-wave superconductors follows a $1/T$ law for small temperatures [29, 30]. With very good agreement, this prediction could be also observed in the intermodulation experiments, such as the work done by *Oates* as well as *Benz et al.* [31, 32]. The anomalous Meissner effect has also recently been shown to have a strong influence on the Bean-Livingston surface barrier for entrance of vortices into the superconductor [33]. The nonlocal effects as well as the impurity scattering can however change this behavior and result in a saturation in the limit of low temperatures [34, 35].

1.3 Aims and contents of this work

In the following, chapter 2 deals with the theoretical background required for this work. An overview of the microscopic theory and quasiclassical propagators is given, as the basis of our calculations. Furthermore, the impurity self energies in the Born approximation limit are introduced as tools to consider the impure superconducting model.

We start chapter 3 by introducing the geometry under consideration and the numerical approach to solve the necessary equations and calculate different quantities such as order parameter amplitude, scattering rates, density of states, current density, etc. Then, we discuss the surface effects of a d-wave superconductor, in the presence of nonmagnetic Born impurity scattering, an external magnetic field and

a combination of both effects. We will show that the impurity scattering rate in the presence of the zero-energy Andreev bound states is significantly larger than the known bulk results. It results in a larger broadening of these states than expected from the scattering rate in the bulk.

It is also known that the renormalization of the pairing potential due to the impurities vanishes in the bulk. We can show here, that due to the broken translational symmetry, this is not generally the case near the surface. Except for the case where the orientation of the surface is highly symmetric with respect to the orientation of the d-wave, we obtain a nonzero renormalization of the pairing potential at the surface.

Applying an external magnetic field will change the situation; the scattering rate at the surface is influenced by the field and the splitting of the Andreev bound states due to the magnetic field turns out to be quite robust against Born impurity scattering. The renormalization of the pairing potential on the other hand is nonzero for all surface orientations relative to the d-wave.

A significant influence of the surface bound states on the nonlinear Meissner effect is also observed by looking at the variation of the surface vector potential versus applied magnetic field. We show that the anomalous surface current leads to a strong modification of linear response properties. It gives us enough motivation to study the nonlinear Meissner effect extensively, which is discussed in chapter 4.

In chapter 4 we study the influence of the anomalous surface current on the nonlinear Meissner effect. Calculating the nonlinear response coefficient, we find the temperature dependence of the zero-energy bound states contribution to follow a $1/T^3$ law. For sufficiently low temperatures, it dominates the known bulk $1/T$ behavior.

We show that the crossover from bulk dominated behavior to surface dominated behavior occurs at temperatures about $T/T_c \sim 1/\sqrt{\kappa}$, which is a comparatively large temperature. The experimental possible range to observe such an effect is between this crossover temperature and $T/T_c \sim 1/\kappa$, where the nonlocal effects will dominate. To probe the existence of surface Andreev bound states, one has to look for the $1/T^3$ behavior in the given temperature range. Such a measurement can be done by intermodulation distortion experiments as tools to probe the d-wave symmetry and the Andreev bound states.

To provide a physical understanding of the numerical calculations done on the nonlinear Meissner effect, we propose a model which can be solved analytically in chapter 5. The results are in good agreement with the numerical results at low temperatures.

Chapter 2

Theoretical background

In this chapter, the necessary theoretical background will be discussed. In particular, the quasiclassical theory is introduced, which provides the appropriate tool for the determination of spatially varying thermodynamic quantities. Almost all calculations were carried out within this framework. Furthermore, Anderson's theorem for impure isotropic superconductors is discussed. We will make a comparison between this theorem and our numerical results at the surface in chapter 3. In the whole work, we have treated the impurities in the Born approximation limit. Therefore, an introduction to the Born impurities and the associated self energies is given.

2.1 Microscopic theory

With spatially inhomogeneous problems at arbitrary temperatures, one may encounter many difficulties in solving the Schrödinger equation using a many body Hamiltonian. In order to handle such problems appropriately, Gor'kov was the first to apply the Green's function formalism to the theory of superconductivity. The so called Matsubara Green's functions are introduced in subsection 2.1.1, treating time as an imaginary parameter. This allows for using the time ordering operator in formulating the Green's functions in a very compact form, thereby rendering Gibbs ensemble averaging possible (see equation (2.5)). In subsection 2.1.2, Dyson's equation is shown, using the diagram technique. It is a compact form of writing the Green's functions in the presence of impurities, which are included in the so called self energy term.

As these functions are still complicated and depend on many parameters, it would be useful to define more simplified functions. This will be demonstrated in subsection 2.1.3, where the propagators in the quasiclassical limit, i.e. when $k_F\xi \gg 1$, are introduced. They are the energy integrated Matsubara Green's functions and thus independent of the energy. With an analytic continuation to the real axis, one can find measurable quantities, like the density of states.

In order to solve the quasiclassical equations, numerical methods need to be

employed, often leading to complex, time consuming calculations. The Riccati parametrization of the quasiclassical propagators, which is introduced in the last subsection 2.1.4, leads to speedy calculations with stable solutions. In this approach, just two one-dimensional initial value differential equations for scalar parameters $a(s)$ and $b(s)$ (introduced below) need to be solved in order to find the parametrized quasiclassical parameters.

2.1.1 Matsubara Green's functions

Since its introduction to non-relativistic quantum field theory [17, 36, 37], the formalism of *Green's functions* has also become one of the basic tools in condensed matter physics. For problems at finite temperature, the usual method in statistical physics to calculate the temperature dependence of thermodynamic quantities directly is very complicated. It involves solving the Schrödinger equation with many body Hamiltonian using perturbation theory. The perturbation series usually includes an infinite number of terms. In order to work with complex systems, it is therefore important to find a formalism that takes into account only the essential elements and simplifies the problem in an acceptable way. Here, the diagram technique can be very helpful. It relies on Green's functions and supplies a way to build a complete structure of the problem within any used approximation.

The method of Green's functions in the relativistic field theory was first introduced during the late 40s and early 50s by *Hans Bethe*, *Tomonaga*, *Schwinger*, *Feynman*, and *Dyson* through the procedure known as renormalization. In considering spatially inhomogeneous problems in superconductivity at arbitrary temperatures (which can neither be explained by the Ginzburg-Landau theory, valid only near the transition temperature, nor by the BCS theory, which is valid only for homogeneous superconductors) the work of *Gor'kov* [38, 39] is of fundamental importance. He introduced the method of Green's functions into the theory of superconductivity. The Green's functions, also termed quantum field propagators, are dynamic variables which do only contain the information of a system necessary to derive the interesting experimental quantities. Beyond that, working with this formalism in non-stationary systems, one needs to find the time dependent Green's function in order to know the evolution of the system and the non-equilibrium excitations. In order to generalize the diagram technique to finite temperature problems, *Gor'kov* and *Eliashberg* conceived a method, using the temperature (Matsubara) Green's function. Unlike ordinary Green's functions, the Matsubara functions depend on an *imaginary time* parameter. It means that the real parameter t describing time evolution is generalized to a path in the complex time plane. The purpose of this imaginary time is that it allows the Green's function to be written in a compact form with ordered quantum field operators. By using the time ordering operator T_τ, all the quantum field operators are placed in order of decreasing time τ. In this way, averaging over thermal fluctuations in the Gibbs ensemble becomes possible.

For the special case of thermal equilibrium, complex time evolution is restricted to the imaginary axis [40]

$$t = i\tau \quad \text{with } \tau \in [-\beta, \beta]\,,$$

where $\beta = 1/k_B T$ denotes the inverse thermal energy.

In the diagram technique, the temperature Green's function for fermions is defined as [17]

$$\begin{aligned} &G_{\sigma_1\sigma_2}(\boldsymbol{r}_1, \tau_1; \boldsymbol{r}_2, \tau_2) \\ &= \begin{cases} -\mathrm{Tr}\{e^{\beta(\Omega+\mu\hat{N}-\hat{H})} e^{(\hat{H}-\mu\hat{N})(\tau_1-\tau_2)} \psi_{\sigma_1}(\boldsymbol{r}_1) e^{-(\hat{H}-\mu\hat{N})(\tau_1-\tau_2)} \psi^\dagger_{\sigma_2}(\boldsymbol{r}_2)\} & \text{for } \tau_1 > \tau_2 \\ \mathrm{Tr}\{e^{\beta(\Omega+\mu\hat{N}-\hat{H})} e^{-(\hat{H}-\mu\hat{N})(\tau_1-\tau_2)} \psi^\dagger_{\sigma_2}(\boldsymbol{r}_2) e^{(\hat{H}-\mu\hat{N})(\tau_1-\tau_2)} \psi_{\sigma_1}(\boldsymbol{r}_1)\} & \text{for } \tau_1 < \tau_2 \end{cases} \end{aligned} \tag{2.1}$$

where

$$e^{-\beta\Omega} = \mathrm{Tr}\{e^{-\beta(\hat{H}-\mu\hat{N})}\}.$$

Here, $\psi_{\sigma_1}(\boldsymbol{r}_1)$ and $\psi^\dagger_{\sigma_1}(\boldsymbol{r}_2)$ are the fermionic creation and annihilation field operators and the symbol Tr{...} denotes the ordinary Gibbs statistical average. As can be seen, these Green's functions depend only on the time difference $\tau = \tau_1 - \tau_2$.

An important property of such Green's functions is obtained by rewriting $G(\tau < 0)$ using a cyclic permutation of the operators [17]

$$\begin{aligned} G(\tau < 0) &= \mathrm{Tr}\{e^{\beta\Omega} e^{(\hat{H}-\mu\hat{N})\tau} \psi(\boldsymbol{r}_1) e^{-(\hat{H}-\mu\hat{N})[\tau+\beta]} \psi^\dagger(\boldsymbol{r}_2)\} \\ &= \mathrm{Tr}\{e^{\beta(\Omega+\mu\hat{N}-\hat{H})} e^{(\hat{H}-\mu\hat{N})[\tau+\beta]} \psi(\boldsymbol{r}_1) e^{-(\hat{H}-\mu\hat{N})[\tau+\beta]} \psi^\dagger(\boldsymbol{r}_2)\}. \end{aligned}$$

Comparing with (2.1) results in

$$G(\tau) = -G(\tau + \beta) \qquad \text{for } -\beta < \tau < 0. \tag{2.2}$$

This property shows that the Matsubara Green's functions can be expanded in a Fourier series [41] with Fourier coefficients

$$G(i\varepsilon_n) = \int_0^\beta d\tau e^{i\varepsilon_n \tau} G(\tau), \tag{2.3}$$

where $\varepsilon_n = (2n+1)\pi/\beta$ denotes the discrete Matsubara frequency for fermions and is the conjugate variable to the imaginary time τ.

In order to write the Green's function in a more simplified form, the field operators are written in the imaginary time Heisenberg picture [17]

$$\begin{aligned} \hat{\psi}_{\sigma_1}(\boldsymbol{r}, \tau) &= e^{(\hat{H}-\mu\hat{N})\tau} \psi_{\sigma_1}(\boldsymbol{r}) e^{-(\hat{H}-\mu\hat{N})\tau} \\ \hat{\bar{\psi}}_{\sigma_1}(\boldsymbol{r}, \tau) &= e^{(\hat{H}-\mu\hat{N})\tau} \psi^\dagger_{\sigma_1}(\boldsymbol{r}) e^{-(\hat{H}-\mu\hat{N})\tau}. \end{aligned} \tag{2.4}$$

One can see that

$$\left[\hat{\psi}_{\sigma_1}(\boldsymbol{r}, \tau)\right]^\dagger = \hat{\bar{\psi}}_{\sigma_1}(\boldsymbol{r}, -\tau),$$

which means that these two operators are no longer Hermitian conjugate of each other, unless $\tau = 0$. Using the operators defined in equation (2.4), one can write the equation (2.1) as

$$G_{\sigma_1\sigma_2}(\boldsymbol{r}_1,\tau_1;\boldsymbol{r}_2,\tau_2) = -\mathrm{Tr}\{e^{(\Omega+\mu\hat{N}-\hat{H})/T}T_\tau(\hat{\psi}_{\sigma_1}(\boldsymbol{r}_1,\tau_1)\hat{\bar{\psi}}_{\sigma_2}(\boldsymbol{r}_2,\tau_2))\} \quad (2.5)$$

$$\equiv \left\langle T_\tau(\hat{\psi}_{\sigma_1}(\boldsymbol{r}_1,\tau_1)\hat{\bar{\psi}}_{\sigma_2}(\boldsymbol{r}_2,\tau_2))\right\rangle, \quad (2.6)$$

where T_τ is the T-ordering operator which orders the time-dependent operators in time

$$T_\tau\left(\psi(\tau_1)\psi(\tau_2)\psi(\tau_3)\right) = \psi(\tau_3)\psi(\tau_1)\psi(\tau_2) \qquad \text{if} \quad \tau_3 > \tau_1 > \tau_2.$$

The Matsubara Green's functions relevant for superconductivity theory at finite temperature are written in the so-called Wigner representation, which is a spatial Fourier transformation with respect to the relative coordinate $\boldsymbol{s} = \boldsymbol{r}_1 - \boldsymbol{r}_2$. This mixed representation which depends on the relative momentum $\boldsymbol{p}$, the conjugate variable to $\boldsymbol{s}$, as well as the center of mass coordinate $\boldsymbol{r} = (\boldsymbol{r}_1 + \boldsymbol{r}_2)/2$, is useful as long as the coherence length ξ is large compared to the inter-atomic distance. Furthermore, the system is assumed to be in thermal equilibrium, so that the Green's functions depend only on the difference of the two imaginary times $\tau = \tau_1 - \tau_2$. Using equation (2.3), the Green's functions in the Wigner representation have the following form [40]:

$$G_{\sigma_1,\sigma_2}(\boldsymbol{r},\boldsymbol{p},i\varepsilon_n) = \int_V d^3s e^{-\frac{i}{\hbar}\langle\boldsymbol{p},\boldsymbol{s}\rangle}\int_0^\beta d\tau e^{i\varepsilon_n\tau}\left\langle -T_\tau\left[\hat{\psi}_{\sigma_1}\left(\boldsymbol{r}+\frac{\boldsymbol{s}}{2},\tau\right)\hat{\bar{\psi}}_{\sigma_2}\left(\boldsymbol{r}-\frac{\boldsymbol{s}}{2},0\right)\right]\right\rangle_{\beta,\mu}$$

$$F_{\sigma_1,\sigma_2}(\boldsymbol{r},\boldsymbol{p},i\varepsilon_n) = \int_V d^3s e^{-\frac{i}{\hbar}\langle\boldsymbol{p},\boldsymbol{s}\rangle}\int_0^\beta d\tau e^{i\varepsilon_n\tau}\left\langle -T_\tau\left[\hat{\psi}_{\sigma_1}\left(\boldsymbol{r}+\frac{\boldsymbol{s}}{2},\tau\right)\hat{\psi}_{\sigma_2}\left(\boldsymbol{r}-\frac{\boldsymbol{s}}{2},0\right)\right]\right\rangle_{\beta,\mu}$$

$$\bar{F}_{\sigma_1,\sigma_2}(\boldsymbol{r},\boldsymbol{p},i\varepsilon_n) = \int_V d^3s e^{-\frac{i}{\hbar}\langle\boldsymbol{p},\boldsymbol{s}\rangle}\int_0^\beta d\tau e^{i\varepsilon_n\tau}\left\langle -T_\tau\left[\hat{\bar{\psi}}_{\sigma_1}\left(\boldsymbol{r}+\frac{\boldsymbol{s}}{2},\tau\right)\hat{\bar{\psi}}_{\sigma_2}\left(\boldsymbol{r}-\frac{\boldsymbol{s}}{2},0\right)\right]\right\rangle_{\beta,\mu}$$

$$\bar{G}_{\sigma_1,\sigma_2}(\boldsymbol{r},\boldsymbol{p},i\varepsilon_n) = \int_V d^3s e^{-\frac{i}{\hbar}\langle\boldsymbol{p},\boldsymbol{s}\rangle}\int_0^\beta d\tau e^{i\varepsilon_n\tau}\left\langle -T_\tau\left[\hat{\bar{\psi}}_{\sigma_1}\left(\boldsymbol{r}+\frac{\boldsymbol{s}}{2},\tau\right)\hat{\psi}_{\sigma_2}\left(\boldsymbol{r}-\frac{\boldsymbol{s}}{2},0\right)\right]\right\rangle_{\beta,\mu}$$

where each of these functions are composed of two creation and annihilation operators. In the theory of superconductivity, not only the normal Matsubara Green's function $G_{\sigma_1,\sigma_2}(\boldsymbol{r},\boldsymbol{p},i\varepsilon_n)$ and its complex conjugate $\bar{G}_{\sigma_1,\sigma_2}(\boldsymbol{r},\boldsymbol{p},i\varepsilon_n)$ are of importance, but also the anomalous Green's function $F_{\sigma_1,\sigma_2}(\boldsymbol{r},\boldsymbol{p},i\varepsilon_n)$ together with its complex conjugate $\bar{F}_{\sigma_1,\sigma_2}(\boldsymbol{r},\boldsymbol{p},i\varepsilon_n)$. These four functions are used to build the entries of Matsubara propagator $\hat{\mathcal{G}}(\boldsymbol{r},\boldsymbol{p},i\varepsilon_n)$ in Nambu space (see subsection 2.1.3), which allows a diagrammatic treatment of the superconducting system

$$\hat{\mathcal{G}}(\boldsymbol{r},\boldsymbol{p},i\varepsilon_n) = \begin{pmatrix} G(\boldsymbol{r},\boldsymbol{p},i\varepsilon_n) & F(\boldsymbol{r},\boldsymbol{p},i\varepsilon_n) \\ -\bar{F}(\boldsymbol{r},\boldsymbol{p},i\varepsilon_n) & -\bar{G}(\boldsymbol{r},\boldsymbol{p},i\varepsilon_n) \end{pmatrix}. \tag{2.7}$$

Both the diagonal and off diagonal elements of the Matsubara propagator (the so-called normal and anomalous propagators) are related by

$$\begin{aligned} \bar{G}_{\sigma_1,\sigma_2}(\boldsymbol{r},\boldsymbol{p},i\varepsilon_n) &= -G_{\sigma_2,\sigma_1}(\boldsymbol{r},-\boldsymbol{p},-i\varepsilon_n) \\ \bar{F}_{\sigma_1,\sigma_2}(\boldsymbol{r},\boldsymbol{p},i\varepsilon_n) &= F^*_{\sigma_2,\sigma_1}(\boldsymbol{r},\boldsymbol{p},-i\varepsilon_n). \end{aligned} \tag{2.8}$$

2.1.2 Dyson's equation

For superconducting alloys with a large amount of random impurities, Abrikosov and Gor'kov in 1958 had developed a method in which they assumed that the physical properties of the superconductor can be obtained by averaging over all the impurity potentials [42]. The Hamiltonian representing the interaction between impurity atoms and the electrons is given by [17]

$$H_{int} = \sum_a H_a,$$

where

$$H_a = \int u(\boldsymbol{r}-\boldsymbol{r}_a)\psi^\dagger(x)\psi(x)d\boldsymbol{r}.$$

$u(\boldsymbol{r}-\boldsymbol{r}_a)$ is the potential by which each impurity atom at position $\boldsymbol{r}_a$ interacts with the electrons at position $\boldsymbol{r}$.

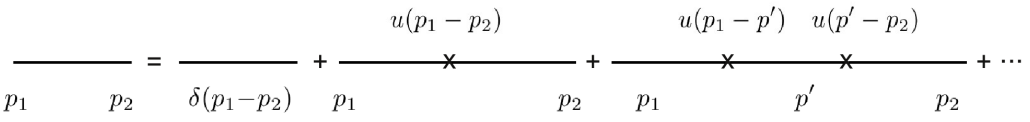

Figure 2.1: Schematic interaction diagram of the perturbation theory. Each line on the right hand side denotes the unperturbed Green's function $\hat{G}^0$ and each cross refers to the impurity vertex.

In order to determine the Green's functions for a system of interacting particles, one can use the diagrammatic perturbation theory. Considering this interaction as a perturbation and starting from the Green's functions for free, non-interacting particles, $\hat{G}^0$, which are still easy to specify, it is possible to expand the Green's functions in a perturbation series, which is determined through summing the interaction terms of the Hamiltonian shown in figure 2.1. In this diagram, each line on the right side is connected to $\hat{G}^0$ and each cross denotes the impurity vertex. The Green's function then is written as [42]

$$\begin{aligned}\hat{G}(\boldsymbol{r}_1,\boldsymbol{r}_2) = &\int \frac{d^3p_1}{(2\pi)^3}\hat{G}^0(\boldsymbol{p}_1)e^{i\boldsymbol{p}_1(\boldsymbol{r}_1-\boldsymbol{r}_2)} \\ &- \sum_a \int \frac{d^3p_1 d^3p_2}{(2\pi)^6} e^{i(\boldsymbol{p}_1\boldsymbol{r}_1-\boldsymbol{p}_2\boldsymbol{r}_2)} e^{-i(\boldsymbol{p}_1-\boldsymbol{p}_2)\boldsymbol{r}_a}\hat{G}^0(\boldsymbol{p}_1)u(\boldsymbol{p}_1-\boldsymbol{p}_2)\hat{G}^0(\boldsymbol{p}_2) \\ &+ \sum_{a,b} \int \frac{d^3p_1 d^3p_2 d^3p'}{(2\pi)^9} e^{i(\boldsymbol{p}_1\boldsymbol{r}_1-\boldsymbol{p}_2\boldsymbol{r}_2)} e^{-i(\boldsymbol{p}_1-\boldsymbol{p}')\boldsymbol{r}_a} e^{-i(\boldsymbol{p}'-\boldsymbol{p}_2)\boldsymbol{r}_b} \\ &\times \hat{G}^0(\boldsymbol{p}_1)u(\boldsymbol{p}_1-\boldsymbol{p}')\hat{G}^0(\boldsymbol{p}')u(\boldsymbol{p}'-\boldsymbol{p}_2)\hat{G}^0(\boldsymbol{p_2}) - ... \quad (2.9)\end{aligned}$$

Due to the randomly distributed impurities, it is reasonable to replace the summation over the impurity positions with an integration over their coordinates

$$\sum_a \to n_{imp}\int d^3r_a,$$

where n_{imp} is the impurity concentration.

In contrast to ordinary quantum mechanics, in quantum statistics it is often impossible to truncate perturbation expansions without large errors. Therefore, the graphical representations of the perturbation terms, which are called *Feynman diagrams*, are taken into account up to infinite orders (see figure 2.2). Using the momentum representation on the left hand side, equation (2.9) may be written in the simplified form below

$$\hat{G}(\boldsymbol{p}_1) = \hat{G}^0(\boldsymbol{p}_1) + \frac{n_{imp}}{(2\pi)^3}\hat{G}^0(\boldsymbol{p}_1)\int |u(\boldsymbol{p}_1-\boldsymbol{p}_2)|^2\,\hat{G}(\boldsymbol{p}_2)\hat{G}(\boldsymbol{p}_1)d\boldsymbol{p}_2.$$

Introducing the total self energy as

$$\hat{\Sigma}(\boldsymbol{p}_1) = n_{imp}\int \frac{d^3p_2}{(2\pi)^3}\,|u(\boldsymbol{p}_1-\boldsymbol{p}_2)|^2\,\hat{G}(\boldsymbol{p}_2), \quad (2.10)$$

the total Green's function will have the form

$$\hat{G} = \hat{G}^0 + \hat{G}^0\,\hat{\Sigma}\,\hat{G}. \quad (2.11)$$

This relation is known as *Dyson's equation*. It contains all the impurity terms summarized in the so-called *self energy* $\hat{\Sigma}$, a generalized effective field which each particle sees due to its interaction with all other particles of the system. This equation can be represented by the use of Feynman diagrams as in figure 2.2.

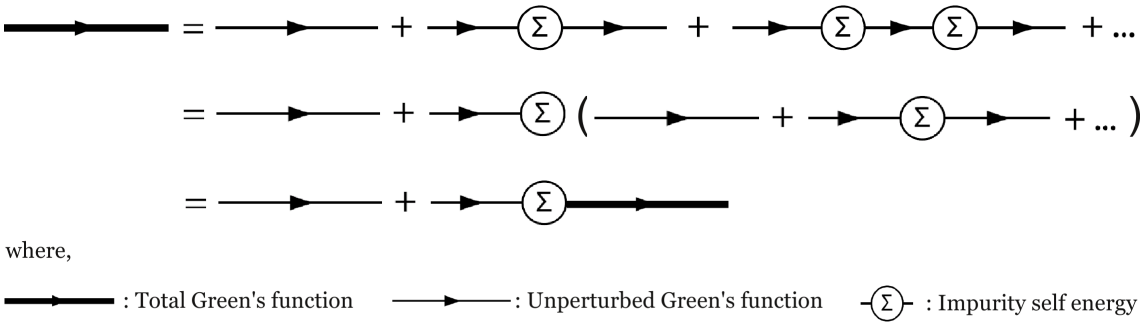

Figure 2.2: Dyson's equation in the form of the Feynman diagrams. The self energy term contains all the possible impurity terms.

Dyson's equation is exact, since the self energy $\hat{\Sigma}$ contains all the possible terms, as can be seen in figure 2.3(a). However, for different approximations, the self energy terms are only evaluated up to a specified order. For example, in the Hartree-Fock approximation, which is of low-order, it is reduced to the first two terms [43] (see figure 2.3(b)).

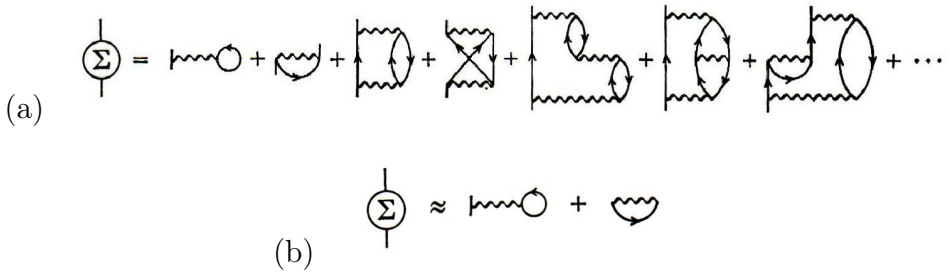

Figure 2.3: (a) Self energy in the form of the Feynman diagrams, consisting of all possible interaction terms. (b) the lowest order approximation for the self energy, the so-called Hartree-Fock approximation [43].

2.1.3 Quasiclassical propagators

Starting from Dyson's equation, Gor'kov [38, 39] succeeded in deriving a system of coupled differential equations for the elements of the Matsubara propagator for $k_F\xi \gg 1$,

$$\left(\hat{\mathcal{H}} - \hat{\Sigma} - \partial_F - \xi_k\right)\hat{\mathcal{G}}(\boldsymbol{r}, \boldsymbol{p}, i\varepsilon_n) = \begin{pmatrix} \sigma^0 & 0 \\ 0 & \sigma^0 \end{pmatrix} = \hat{\mathbf{1}}. \tag{2.12}$$

This matrix equation is called *Gor'kov equation*. Here, the Bogoliubov matrix $\hat{\mathcal{H}}$ is the unperturbed Hamiltonian of the fermionic quasiparticle excitations near the Fermi level [40]. The excitations have a group velocity parallel or anti-parallel to the Fermi velocity and their energy E is related to the Matsubara frequency ε_n via $i\varepsilon_n \to E + i0^+$. The Bogoliubov matrix is a function of $\boldsymbol{r}$, $\hat{\boldsymbol{p}}$ and $i\varepsilon_n$ and is given as

$$\hat{\mathcal{H}} = \begin{pmatrix} i\varepsilon_n + \left\langle \boldsymbol{v}_F, \frac{e}{c}\boldsymbol{A} \right\rangle + \gamma B_z & \gamma(B_x - iB_y) & -\Delta_x + i\Delta_y & \Delta_0 + \Delta_z \\ \gamma(B_x + iB_y) & i\varepsilon_n + \left\langle \boldsymbol{v}_F, \frac{e}{c}\boldsymbol{A} \right\rangle - \gamma B_z & \Delta_0 + \Delta_z & \Delta_x + i\Delta_y \\ \Delta_x^* + i\Delta_y^* & \Delta_0^* - \Delta_z^* & -i\varepsilon_n - \left\langle \boldsymbol{v}_F, \frac{e}{c}\boldsymbol{A} \right\rangle + \gamma B_z & \gamma(B_x + iB_y) \\ -\Delta_0^* - \Delta_z^* & -\Delta_x^* + i\Delta_y^* & \gamma(B_x - iB_y) & -i\varepsilon_n - \left\langle \boldsymbol{v}_F, \frac{e}{c}\boldsymbol{A} \right\rangle - \gamma B_z \end{pmatrix}$$

$$= \begin{pmatrix} \left(i\varepsilon_n + \left\langle \boldsymbol{v}_F, \frac{e}{c}\boldsymbol{A} \right\rangle\right)\sigma^0 + \gamma \langle \boldsymbol{B}, \boldsymbol{\sigma} \rangle & \left(\Delta_0 \sigma^0 + \langle \boldsymbol{\Delta}, \boldsymbol{\sigma} \rangle\right) i\sigma^y \\ i\sigma^y \left(\Delta_0^* \sigma^0 + \langle \boldsymbol{\Delta}^*, \boldsymbol{\sigma} \rangle\right) & -\sigma^y \left[\left(i\varepsilon_n + \left\langle \boldsymbol{v}_F, \frac{e}{c}\boldsymbol{A} \right\rangle\right)\sigma^0 + \gamma \langle \boldsymbol{B}, \boldsymbol{\sigma} \rangle\right] \sigma^y \end{pmatrix}.$$

This is a 4×4 matrix structure in a four dimensional product space of spin and particle-hole variables, the so-called *Nambu space*. The 2×2 super-matrix refers to the particle-hole degree of freedom and the 2×2 sub-matrices refer to spin.

$\hat{\Sigma}(\boldsymbol{r}, \boldsymbol{p}, i\varepsilon_n)$ is the self energy matrix and is given by

$$\hat{\Sigma}(\boldsymbol{r}, \boldsymbol{p}, i\varepsilon_n) = \begin{pmatrix} \Sigma^G(\boldsymbol{r}, \boldsymbol{p}, i\varepsilon_n) & \Sigma^F(\boldsymbol{r}, \boldsymbol{p}, i\varepsilon_n) \\ -\bar{\Sigma}^F(\boldsymbol{r}, \boldsymbol{p}, i\varepsilon_n) & -\bar{\Sigma}^G(\boldsymbol{r}, \boldsymbol{p}, i\varepsilon_n) \end{pmatrix}. \tag{2.13}$$

The Hamiltonian $\hat{\mathcal{H}}$ contains several terms: The spin effect $\gamma \langle \boldsymbol{B}, \boldsymbol{\sigma} \rangle$, that is the influence of the magnetic field $\boldsymbol{B}(\boldsymbol{r}) = \boldsymbol{\nabla} \times \boldsymbol{A}(\boldsymbol{r})$ on the magnetic moment. The orbital effect $\left\langle \boldsymbol{v}_F, \frac{e}{c}\boldsymbol{A} \right\rangle$, which describes the coupling of the magnetic field with the moving charges. And also the pairing potential $\Delta(\boldsymbol{r}, \hat{\boldsymbol{p}})$, i.e. the *pairing strength* of the Cooper pairs. The parameter γ is the gyromagnetic ratio and indicates the magnitude of the coupling energy between the magnetic field and spin, a term which is related to Pauli paramagnetism.

Furthermore, $\boldsymbol{\sigma}$ denotes the vector with the Pauli matrices $\sigma^x, \sigma^y, \sigma^z$ as components, and the matrix σ^0 is the identity matrix

$$\sigma^0 = \begin{pmatrix} 1 & 0 \\ 0 & 1 \end{pmatrix} = \hat{1},\ \sigma^x = \begin{pmatrix} 0 & 1 \\ 1 & 0 \end{pmatrix},\ \sigma^y = \begin{pmatrix} 0 & -i \\ i & 0 \end{pmatrix},\ \sigma^z = \begin{pmatrix} 1 & 0 \\ 0 & -1 \end{pmatrix}.$$

The operator ∂_F in equation (2.12) is the projection of the gradient of the Fermi velocity, i.e. the derivative in the direction of $\boldsymbol{v}_F(\hat{\boldsymbol{p}})$

$$\partial_F = \left\langle \boldsymbol{v}_F, \frac{\hbar}{i}\boldsymbol{\nabla}_r \right\rangle,$$

and ξ_k is the kinetic energy of quasiparticles in the vicinity of the Fermi surface

$$\xi_F = \frac{\hbar}{2m^*} \langle \boldsymbol{p} + \boldsymbol{p}_F, \boldsymbol{p} - \boldsymbol{p}_F \rangle .$$

In 1968, *Eilenberger* succeeded in a further simplification of the Gor'kov equation [44]. He introduced the quasiclassical propagator $\hat{\mathfrak{g}}$ by integrating the Matsubara propagator over the kinetic energy of quasiparticles

$$\begin{aligned} \hat{\mathfrak{g}}(\boldsymbol{r}, \boldsymbol{p}, i\varepsilon_n) &= \mathbb{P} \int_{-\omega_c}^{\omega_c} d\xi_k \hat{\mathcal{G}}(\boldsymbol{r}, \boldsymbol{p}, i\varepsilon_n) \\ &= \pi i \begin{pmatrix} g(\boldsymbol{r}, \hat{\boldsymbol{p}}, i\varepsilon_n) & -if(\boldsymbol{r}, \hat{\boldsymbol{p}}, i\varepsilon_n) \\ i\bar{f}(\boldsymbol{r}, \hat{\boldsymbol{p}}, i\varepsilon_n) & -\bar{g}(\boldsymbol{r}, \hat{\boldsymbol{p}}, i\varepsilon_n) \end{pmatrix}, \end{aligned} \tag{2.14}$$

where he chose the integral cut-off at the Debye frequency ω_c. Assuming an almost constant electronic density of states around the Fermi energy, Eilenberger and Larkin and Ovchinnikov [45] derived a matrix equation, which still allowed the full solution of the problem, but does not require any additional integration over ξ_k

$$\partial_F \hat{\mathfrak{g}} = \left[\hat{\mathcal{H}} - \hat{\Sigma}, \hat{\mathfrak{g}} \right]. \tag{2.15}$$

Furthermore they proved the validity of the following normalization condition, which is essential to solve the problem

$$\hat{\mathfrak{g}} . \hat{\mathfrak{g}} = -\pi^2 \hat{1}. \tag{2.16}$$

Following the symmetry relations stated in equation (2.8) and due to the fact that these properties are not affected by the ξ_k-integration, the four matrix entries of the Eilenberger propagator inherit the same symmetry properties of the normal and anomalous Green's functions [46]

$$\bar{g}_{\sigma_1,\sigma_2}(\boldsymbol{r}, \hat{\boldsymbol{p}}, i\varepsilon_n) = -g_{\sigma_2,\sigma_1}(\boldsymbol{r}, -\hat{\boldsymbol{p}}, -i\varepsilon_n) \tag{2.17}$$

$$\bar{f}_{\sigma_1,\sigma_2}(\boldsymbol{r}, \hat{\boldsymbol{p}}, i\varepsilon_n) = f^*_{\sigma_2,\sigma_1}(\boldsymbol{r}, \hat{\boldsymbol{p}}, -i\varepsilon_n) \tag{2.18}$$

$$f_{\sigma_1,\sigma_2}(\boldsymbol{r}, -\hat{\boldsymbol{p}}, -i\hat{\varepsilon}_n) = f_{\sigma_1,\sigma_2}(\boldsymbol{r}, \hat{\boldsymbol{p}}, i\hat{\varepsilon}_n) \tag{2.19}$$

$$g^*_{\sigma_1,\sigma_2}(\boldsymbol{r}, \hat{\boldsymbol{p}}, -i\hat{\varepsilon}_n) = g_{\sigma_1,\sigma_2}(\boldsymbol{r}, \hat{\boldsymbol{p}}, i\hat{\varepsilon}_n) \tag{2.20}$$

These symmetry relations, together with the normalization condition in equation (2.16), result in an important property of the propagator $\hat{\mathfrak{g}}$:

$$\mathrm{Tr}\{\hat{\mathfrak{g}}\} = \mathrm{Tr}\{g\} - \mathrm{Tr}\{\bar{g}\} = 0. \tag{2.21}$$

In this work, we consider only the spin-singlet pairing, leading to a simplified version of the Eilenberger equation:

$$-i\hbar \boldsymbol{v}_F . \boldsymbol{\nabla} \hat{g}(\boldsymbol{r}, \boldsymbol{p}_F, i\varepsilon_n) = \left[\begin{pmatrix} i\varepsilon_n + \boldsymbol{v}_F . \frac{e}{c} \boldsymbol{A}(\boldsymbol{r}) & -\Delta(\boldsymbol{r}, \boldsymbol{p}_F) \\ \Delta^\dagger(\boldsymbol{r}, \boldsymbol{p}_F) & -i\varepsilon_n - \boldsymbol{v}_F . \frac{e}{c} \boldsymbol{A}(\boldsymbol{r}) \end{pmatrix}, \hat{g}(\boldsymbol{r}, \boldsymbol{p}_F, i\varepsilon_n) \right], \tag{2.22}$$

where $\boldsymbol{p}_F = \hbar \boldsymbol{k}_F$ denotes a point on the Fermi surface FS and $\boldsymbol{r}$ is a point in position space. Solving this ordinary differential equation together with the normalization condition (2.16), one can find the quasiclassical propagators $f(\boldsymbol{r}, \boldsymbol{p}_F, i\varepsilon_n)$ and $g(\boldsymbol{r}, \boldsymbol{p}_F, i\varepsilon_n)$. Using these propagators, the observable quantities in thermal equilibrium are determined [46], such as the *pairing potential*

$$\Delta(\boldsymbol{r}, T) = V N_0 \pi k_B T \sum_{|\varepsilon_n|<\omega_c} \langle \chi(\boldsymbol{p}_F)\, f(\boldsymbol{r}, \boldsymbol{p}_F, i\varepsilon_n) \rangle_{FS}\,, \tag{2.23}$$

the *electrical current*

$$\boldsymbol{j}(\boldsymbol{r}, T) = 2eN_0 v_F k_B \pi T \sum_{|\varepsilon_n|<\omega_c} \langle \hat{\boldsymbol{v}}_F \cdot g(\boldsymbol{r}, \boldsymbol{p}_F, i\varepsilon_n) \rangle_{FS}\,. \tag{2.24}$$

and the *local density of states*

$$N(E, \boldsymbol{r}) = -N_0 \,\mathrm{Im}\, \langle g(\boldsymbol{r}, \boldsymbol{p}_F, i\varepsilon_n \to E + i\delta) \rangle_{FS}\,, \tag{2.25}$$

where N_0 is the density of states at the Fermi level in the normal phase, which is constant in an isotropic case.

In the *bulk* of a superconductor, where the pairing potential $\Delta(\boldsymbol{r}, \boldsymbol{p}_F)$ is independent of $\boldsymbol{r}$, the Fermi surface calculation of the Eilenberger propagator considerably simplifies, yielding:

$$\hat{g}_{bulk}(\boldsymbol{p}_F, i\varepsilon_n) = \frac{-\pi}{\sqrt{\varepsilon_n^2 + |\Delta(\boldsymbol{p}_F)|^2}} \cdot \begin{pmatrix} i\varepsilon_n & -\Delta(\boldsymbol{p}_F) \\ \Delta^\dagger(\boldsymbol{p}_F) & -i\varepsilon_n \end{pmatrix}. \tag{2.26}$$

In general, to solve the Eilenberger equation, one needs to find $\Delta(\boldsymbol{r}, \boldsymbol{p}_F)$ and also $\boldsymbol{B}(\boldsymbol{r}) = \boldsymbol{\nabla} \times \boldsymbol{A}(\boldsymbol{r})$ from the Maxwell's equation $\boldsymbol{\nabla} \times \boldsymbol{B}(\boldsymbol{r}) = \mu_0 \boldsymbol{J}(\boldsymbol{r})$. However $\boldsymbol{J}(\boldsymbol{r})$ and $\Delta(\boldsymbol{r}, \boldsymbol{p}_F)$ themselves depend on $\hat{g}(\boldsymbol{r}, \boldsymbol{p}_F, i\varepsilon_n)$. Therefore, a nonlinear self consistent problem needs to be solved, which usually has to be done numerically.

2.1.4 Riccati parametrization

The Riccati parametrization of the quasi-classical propagator was introduced by Schopohl [46, 47] as a means to simplify and stabilize numerical solutions of the Eilenberger equations. Through an appropriate parametrization of the Eilenberger equations, the quasiclassical propagators can be calculated by solving scalar differential equations of Riccati type. This means that instead of solving the Bogoliubov-de Gennes eigenvalue problem, one can easily solve a simple initial value problem.

A good approximation for crystals with a layer structure in the c-axis is often a cylindrical Fermi surface with translational invariance in c-axis direction in position space. Considering this cylindrical Fermi surface together with the set $\{\hat{\boldsymbol{a}}, \hat{\boldsymbol{b}}, \hat{\boldsymbol{c}}\}$ as

an orthonormal basis in position space, one can define a characteristic straight line, referred to as the trajectory, in the direction of the Fermi velocity $\boldsymbol{v}_F$ by

$$\begin{aligned} \boldsymbol{r}(s) &= x\hat{\boldsymbol{v}} + y\hat{\boldsymbol{u}} + z\hat{\boldsymbol{v}} \times \hat{\boldsymbol{u}} \\ &\equiv r_a(s)\hat{\boldsymbol{a}} + r_b(s)\hat{\boldsymbol{b}} + r_c(s)\hat{\boldsymbol{c}}, \end{aligned} \tag{2.27}$$

where $-\infty < s < \infty$. $\hat{\boldsymbol{u}}$ and $\hat{\boldsymbol{v}}$ are unit vectors oriented respectively perpendicular and parallel to the Fermi velocity $\boldsymbol{v}_F$. Along such a trajectory, the directional derivative of the quasiclassical propagator in the Eilenberger equation (2.22) becomes equivalent to an ordinary derivative

$$\hbar \boldsymbol{v}_F.\boldsymbol{\nabla}\hat{g}(\boldsymbol{r}, \boldsymbol{p}_F, i\varepsilon_n) \equiv \hbar \boldsymbol{v}_F \frac{\partial}{\partial s}\hat{g}(\boldsymbol{r}(s), \boldsymbol{p}_F, i\varepsilon_n).$$

The variables $\Delta(\boldsymbol{r})$, $\boldsymbol{A}(\boldsymbol{r})$ and $\hat{g}(\boldsymbol{r}, \boldsymbol{p}_F, i\varepsilon_n)$ are considered only on these trajectories. Along the trajectories, all other variables remain constant and the notation can be simplified to:

$$\begin{aligned} \Delta(s) &= \Delta\left[\boldsymbol{r}(s), \boldsymbol{p}_F\right] \\ i\bar{\varepsilon}_n(s) &= i\varepsilon_n + \frac{e}{c}\boldsymbol{v}_F \cdot \boldsymbol{A}\left[\boldsymbol{r}(s)\right] \\ \hat{g}(s) &= \hat{g}\left[\boldsymbol{r}(s), \boldsymbol{p}_F, i\varepsilon_n\right]. \end{aligned} \tag{2.28}$$

Now, as described in detail in reference [46], the quasiclassical Propagator $\hat{g}(s)$ can be parametrized in the form

$$\hat{g}(s) = \frac{-i\pi}{1 + a(s)b(s)} \begin{pmatrix} 1 - a(s)b(s) & 2ia(s) \\ -2ib(s) & -1 + a(s)b(s) \end{pmatrix}. \tag{2.29}$$

Here $a(s)$ and $b(s)$ are two *scalar* complex quantities which solve the following differential equations

$$\hbar v_F \frac{\partial}{\partial s}a(s) + \left[2\bar{\varepsilon}_n(s) + \Delta^\dagger(s)a(s)\right]a(s) - \Delta(s) = 0 \tag{2.30}$$

$$\hbar v_F \frac{\partial}{\partial s}b(s) - \left[2\bar{\varepsilon}_n(s) + \Delta(s)b(s)\right]b(s) + \Delta^\dagger(s) = 0. \tag{2.31}$$

These differential equations are of *Riccati* type and can be solved as an *initial value problem* by using the suitable initial values in order to have stable solutions. When $i\varepsilon_n$ is on the upper half-plane imaginary axis, the function $a(s)$ should be solved from the bulk value at $s \to -\infty$ towards increasing s values in order to stay stable, while the function $b(s)$ should be solved from $s \to +\infty$ towards decreasing s values. So the differential equations (2.30) and (2.31) can be solved with initial values $a(s \to -\infty)$ and $b(s \to +\infty)$ respectively. These initial values are the bulk solutions which are

obtained by neglecting the gradient term in equations (2.30) and (2.31)

$$a(-\infty) = \frac{\Delta(-\infty)}{\bar{\varepsilon}_n + \sqrt{\bar{\varepsilon}_n^2 + |\Delta(-\infty)|^2}} \tag{2.32}$$

$$b(+\infty) = \frac{\Delta^\dagger(-\infty)}{\bar{\varepsilon}_n + \sqrt{\bar{\varepsilon}_n^2 + |\Delta(+\infty)|^2}} \tag{2.33}$$

Now, one can find the two normal $g(\boldsymbol{r}, \boldsymbol{p}_F, i\varepsilon_n)$ and anomalous $f(\boldsymbol{r}, \boldsymbol{p}_F, i\varepsilon_n)$ propagators as

$$g(\boldsymbol{r}, \boldsymbol{p}_F, i\varepsilon_n) = -i\frac{1 - a(s)b(s)}{1 + a(s)b(s)} \tag{2.34}$$

$$f(\boldsymbol{r}, \boldsymbol{p}_F, i\varepsilon_n) = \frac{2a(s)}{1 + a(s)b(s)}. \tag{2.35}$$

In the next chapter, we discuss how to use these quasiclassical propagators in order to find experimentally relevant quantities, such as the pairing potential, the current density or the density of states.

2.2 Impurities

Until the discovery of anisotropic superconductors, measurements done on physical properties in s-wave superconductors had shown that they are robust against nonmagnetic impurities. This was also confirmed by Anderson's theorem which is discussed shortly in subsection 2.2.1. However, this is not the case anymore when the pairing potential is not isotropic, for example in a d-wave superconductor. In this thesis we have treated the impurities in the Born approximation limit, explained in subsection 2.2.2. Both diagonal and off-diagonal impurity self energies, which are used to renormalize the order parameter and the energy, are also introduced.

2.2.1 Anderson's theorem

Anderson [48] was the first one to point out that the nonmagnetic impurities do not affect the properties of the bulk s-wave superconductors. This can be well observed from the measurements done for the density of states, critical temperature and the pairing potential. In the presence of impurities, the pairing potential Δ and the energy ε_n will be renormalized due to the impurity self energies. In the Born

approximation for an isotropic s-wave superconductor, one obtains [18]

$$\tilde{\varepsilon}_n = \varepsilon_n + \frac{1}{2}\left(\frac{1}{\tau_a} + \frac{1}{\tau_b}\right)\frac{\tilde{\varepsilon}_n}{\left(\tilde{\varepsilon}_n^2 + \tilde{\Delta}^2\right)^{1/2}} \tag{2.36}$$

$$\tilde{\Delta} = \Delta + \frac{1}{2}\left(\frac{1}{\tau_a} - \frac{1}{\tau_b}\right)\frac{\tilde{\Delta}}{\left(\tilde{\varepsilon}_n^2 + \tilde{\Delta}^2\right)^{1/2}}, \tag{2.37}$$

where τ_a and τ_b are the scattering and spin-flip lifetimes corresponding to the non-magnetic and magnetic impurities, respectively. Defining the parameter $u = \tilde{\varepsilon}_n/\tilde{\Delta}$ and using equation (2.37), one can find [18]

$$\frac{\varepsilon_n}{\Delta} \propto u\left[1 - \frac{1}{\tau_b\Delta\left(1+u^2\right)^{1/2}}\right] \tag{2.38}$$

and the pairing amplitude will become

$$\Delta \propto \sum_u \left(1+u^2\right)^{-1/2}. \tag{2.39}$$

It shows that the pairing potential depends only on the ratio of $\tilde{\varepsilon}_n/\tilde{\Delta}$. On the other hand, if no magnetic impurity is present, the spin-flip lifetime becomes infinite and therefore the equation (2.38) reduces to

$$\frac{\varepsilon_n}{\Delta} = u = \frac{\tilde{\varepsilon}_n}{\tilde{\Delta}}. \tag{2.40}$$

The pairing equation is then independent of the impurities, thus the gap and transition temperature will remain unchanged due to the impurities.

In chapter 3, it is shown that for a d-wave superconductor, the bulk renormalization of the pairing potential vanishes, due to the zero Fermi surface average caused by the sign change in the d-wave pairing. Therefore, d-wave superconductors are sensitive to the impurity concentrations (see section 3.4).

2.2.2 Born approximation

To study the behavior of a superconductor with randomly distributed impurities, one can use perturbation theory. As discussed in the literature, for homogeneous systems with low impurity density, where the effect of the scattering potential is small, the physical properties may be obtained by averaging over the impurity positions [18, 42]. All possible interactions between electrons and impurities can be included in the *self energy* term shown in a diagrammatic form in figure 2.4. In this sketch, the dashed lines denote the scattering potential, the solid line indicates the unperturbed Green's

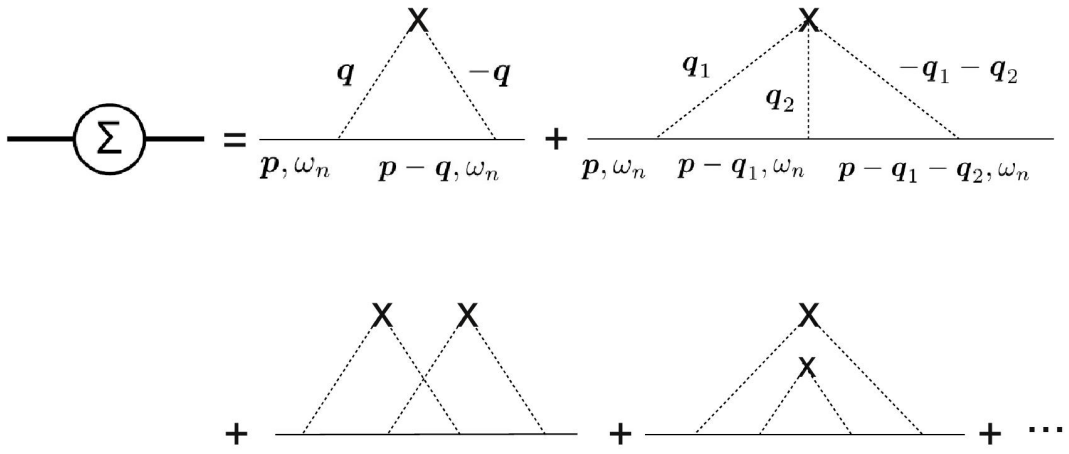

Figure 2.4: Possible interactions between electrons and impurities, included in the self energy term of a system with randomly distributed impurities. The dashed lines indicate the scattering potential, the solid line is the unperturbed Green's function and each cross is an impurity averaged factor $n_i\,\delta_{\sum \boldsymbol{q},0}$. The total momentum entering each impurity vertex is zero, while the energy carried by the electron remains unchanged [18]. For very weak impurities, one considers only the first term, i.e. with one impurity vertex and the lowest interactions; the so-called Born approximation. To account for the interaction caused by a significantly large impurity center, known as *unitary scatterer*, one may sum over all terms with one impurity vertex, but all possible interactions, i.e. the first two terms and the similar terms with more interaction lines. This approximation is known as *T-matrix approximation*.

function and each cross is an impurity averaged factor $n_i\,\delta_{\sum \boldsymbol{q},0}$ [49]. As can be seen, the energy carried by the electron remains unchanged while the total momentum which enters each impurity vertex is zero. This feature arises from the fact that the scattering is elastic, therefore each dashed line carries zero energy [18].

In the limit of very weak impurities, it is reasonable to make an approximation in the self energy up to the first term shown in figure 2.4. Thus

$$\Sigma^0(\boldsymbol{r},\boldsymbol{p},i\varepsilon_n) \;=\; n_i \sum_{\boldsymbol{q}} V(\boldsymbol{q})V(-\boldsymbol{q})G^0(\boldsymbol{r},\boldsymbol{p}-\boldsymbol{q},i\varepsilon_n). \tag{2.41}$$

Using the relation $V(-\boldsymbol{q}) = V^*(\boldsymbol{q})$ for real potentials, and with $\boldsymbol{p}' = \boldsymbol{p} - \boldsymbol{q}$, one obtains [18]

$$\Sigma^0(\boldsymbol{r},\boldsymbol{p},i\varepsilon_n) = n_i \sum_{\boldsymbol{p}'} \left|V(\boldsymbol{p}-\boldsymbol{p}')\right|^2 G^0(\boldsymbol{r},\boldsymbol{p}',i\varepsilon_n).$$

The electrons near the Fermi surface are normally responsible for the transport properties and therefore of the most interest. Considering these electrons and changing

the summation to an integral over the Fermi surface [18, 50, 51], the self energy will be determined from an angular average over the Fermi surface, $\langle \cdots \rangle_{FS}$, therefore being independent of the Fermi momentum:

$$\Sigma^0(\boldsymbol{r}, i\varepsilon_n) = \frac{\pi}{\hbar} n_i N_0 \left\langle |V(\boldsymbol{p} - \boldsymbol{p}_F)|^2 G^0(\boldsymbol{r}, \boldsymbol{p}_F, i\varepsilon_n) \right\rangle_{FS}. \tag{2.42}$$

For simplicity, we will restrict ourselves to s-wave scattering. Thus, the scattering potential will also be independent of the Fermi momentum, i.e. $V(\boldsymbol{p}-\boldsymbol{p}_F) = \text{const.} = V_0$, with V_0 being the strength of the impurity potential. Then, equation (2.42) can be written as

$$\Sigma^0(\boldsymbol{r}, i\varepsilon_n) = \frac{\pi}{\hbar} n_i N_0 |V_0|^2 \left\langle G^0(\boldsymbol{r}, \boldsymbol{p}_F, i\varepsilon_n) \right\rangle_{FS}. \tag{2.43}$$

Substituting the unperturbed Green's function with the full Green's function, leads to the self-consistent Born approximation:

$$\Sigma(\boldsymbol{r}, i\varepsilon_n) = \frac{\pi}{\hbar} n_i N_0 |V_0|^2 \left\langle G(\boldsymbol{r}, \boldsymbol{p}_F, i\varepsilon_n) \right\rangle_{FS}. \tag{2.44}$$

At last, the diagonal and off-diagonal impurity self energies in the self-consistent Born approximation are given by

$$\Sigma^F(\boldsymbol{r}, i\varepsilon_n) = \frac{1}{2\tau} \left\langle f(\boldsymbol{r}, \boldsymbol{p}_F, i\varepsilon_n) \right\rangle_{FS} \tag{2.45}$$

$$\Sigma^G(\boldsymbol{r}, i\varepsilon_n) = \frac{1}{2\tau} \left\langle g(\boldsymbol{r}, \boldsymbol{p}_F, i\varepsilon_n) \right\rangle_{FS}, \tag{2.46}$$

where τ is the scattering lifetime in the bulk:

$$\frac{1}{\tau} = \frac{2}{\hbar} \pi N_0 n_i |V_0|^2. \tag{2.47}$$

Chapter 3

Surface effects in d-wave superconductors

In this chapter we investigate the influence of bulk impurity scattering at the surface of a d-wave superconductor. We will see that the existence of Andreev bound states results in a significant increase of the scattering rate at the surface in comparison with the bulk. The influence of these states on transport properties for two different cases, with and without an external magnetic field, is investigated. The main results obtained in this chapter are published in [52].

The impurity scattering in the Born limit has been shown to be much more effective in broadening the Andreev bound states than impurity scattering in the unitary limit [21, 22]. As an example we refer to the work by Tanaka et al., in which they studied the influence of bulk impurities on the tunneling conductance spectra in a junction consisting of a normal metal, an insulator and a d-wave superconductor (n-I-d junction). Within the framework of the quasiclassical theory, they could compare the zero-bias conductance peak resulting from the zero energy Andreev bound states. The result was a significant broadening of these states in the Born approximation limit, in comparison to the unitary limit. In figure 3.1 this difference is shown. They could also confirm Anderson's theorem by showing a robustness against the impurities for a s-wave superconductor.

In high-T_c cuprate compounds it is believed that scatterers within the CuO_2 planes act as unitary scatterers. Such scattering should have little influence on the Andreev bound states. Recently however, it has been recognized that scatterers sitting between the CuO_2 planes are poorly screened and act as Born scatterers [51, 53, 54]. These impurities are thus expected to have a dominating influence on the broadening of the Andreev bound states. For these reasons in this work we will focus on the influence of impurity scattering in the self-consistent Born approximation. Throughout this text we will quantify the impurity scattering in terms of its mean free path $\ell = v_F\tau$ relative to the zero temperature bulk coherence length in the superclean limit $\xi_0 = \hbar v_F/\pi\Delta_0$.

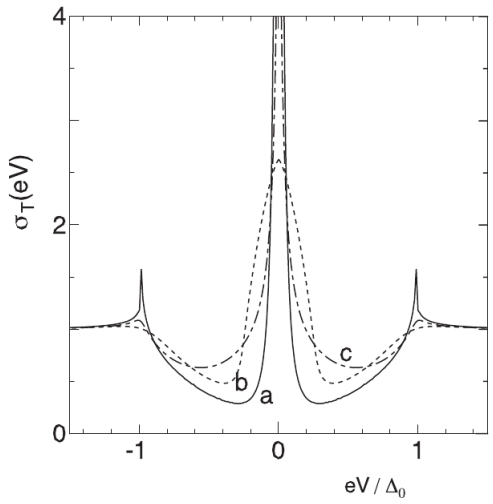

Figure 3.1: The normalized tunneling conductance in a two dimensional n-I-d junction with $\alpha = \frac{\pi}{4}$. This plot compares three different cases: the clean limit (a), the Born approximation limit with $\hbar\Delta_0/2\tau = 0.1$ and $\sigma = 0$ (b) and finally the unitary limit with $\hbar\Delta_0/2\tau = 0.1$ and $\sigma = 0.99$ (c). $\hbar/2\tau$ denotes the normal scattering rate while σ is the strength of a simple impurity potential. Δ_0 is the bulk gap in the clean limit. One can see that for a same scattering rate, Born approximation leads to a much larger broadening in the zero energy peak than the unitary limit. (Adapted from [22], Copyright © (2001) by the American Physical Society).

3.1 Geometry

The Geometry under investigation in this dissertation is shown in figure 3.2. It consists of a superconducting area in the half space $x > 0$. The superconductor is assumed to have a d-wave pairing potential with the pairing symmetry

$$\chi(\boldsymbol{p}_F) = \cos\,[2(\theta - \alpha)]. \tag{3.1}$$

The angle α determines the relative orientation of the d-wave pairing with respect to the surface normal and θ indicates the direction of the Fermi velocity. Furthermore, an external magnetic field $\boldsymbol{B} = B_{ext}\,\boldsymbol{e}_z$ is applied parallel to the z-axis, which is assumed to remain smaller than the field of first vortex penetration. For simplicity, we consider a cylindrical Fermi surface with the c-axis oriented parallel to the z-axis. Therefore, we can assume translational invariance both along the y-axis as well as along the z-direction. Due to the external magnetic field, a vector potential $\boldsymbol{A}$ exists parallel to the surface and is given by $\boldsymbol{B} = \boldsymbol{\nabla} \times \boldsymbol{A}$. Using the Coulomb gauge, i.e. $\boldsymbol{\nabla} \cdot \boldsymbol{A} = 0$, the Maxwell's equation $\boldsymbol{\nabla} \times \boldsymbol{B} = \mu_0 \boldsymbol{j}$ is given by

$$-\boldsymbol{\Delta A} = \mu_0 \boldsymbol{j}, \tag{3.2}$$

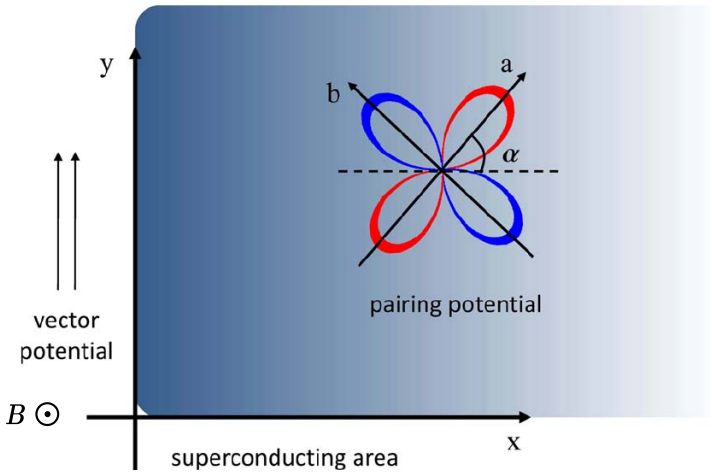

Figure 3.2: Sketch of the investigated geometry. It presents a d-wave superconducting area for $x > 0$ with a pairing potential oriented in the α direction relative to the surface normal. The direction of the external magnetic field and the resulting vector potential is also shown.

where $\boldsymbol{j}$ is the total current density inside the superconductor. In this gauge, the vector potential is proportional to the superfluid velocity $\boldsymbol{v}_s$ [55]

$$\boldsymbol{v}_s(\boldsymbol{r}) = \frac{1}{2m}\left(\hbar\boldsymbol{\nabla}\phi(\boldsymbol{r}) - \frac{2e}{c}\boldsymbol{A}(\boldsymbol{r})\right). \tag{3.3}$$

$\boldsymbol{\nabla}\phi(\boldsymbol{r})$ is the gradient of the phase of the pairing potential: $\Delta(\boldsymbol{r}) = |\Delta(\boldsymbol{r})|\, e^{i\phi(\boldsymbol{r})}$. To solve the second order differential equation (3.2), one needs the boundary conditions which are determined by the behavior of the magnetic field; it is equal to the external field at the surface, penetrates into the superconductor continuously and decays to zero in the bulk:

$$\boldsymbol{B}(x=0) = B_{ext}\,, \quad \boldsymbol{B}(x\to\infty) = 0. \tag{3.4}$$

Making a gauge transformation, the gradient $\boldsymbol{\nabla}\phi(\boldsymbol{r})$ is set to zero in the problem investigated in this dissertation.

To find the superconducting properties at a given point $\boldsymbol{r}$ in the half-space $x > 0$, one should first solve the Riccati equations (2.30) and (2.31), using the initial values (2.32) and (2.33). In the presence of the magnetic field and impurities, both Matsubara energies and the pair potential will be renormalized as

$$i\bar{\varepsilon}_n \to i\tilde{\varepsilon}_n[\boldsymbol{R}(s),\varepsilon_n] \;\; = \;\; i\varepsilon_n + \frac{e}{c}\boldsymbol{v}_F\cdot\boldsymbol{A}[\boldsymbol{R}(s)] - \Sigma^G[\boldsymbol{R}(s),\varepsilon_n] \tag{3.5}$$

$$\Delta \to \tilde{\Delta}[\boldsymbol{R}(s),\varepsilon_n,T] = \Delta[\boldsymbol{R}(s),T]\,\chi(\boldsymbol{p}_F) + \Sigma^F[\boldsymbol{R}(s),\varepsilon_n]. \tag{3.6}$$

The Riccati equations should be solved along real space trajectories $\boldsymbol{R}(s) = \boldsymbol{r} + s\hat{\boldsymbol{v}}_F$ [47], i.e. all the possible trajectories which go through point $\boldsymbol{r}$ with the angle θ, running parallel to the Fermi velocity $\boldsymbol{v}_F$ (see figure 3.3).

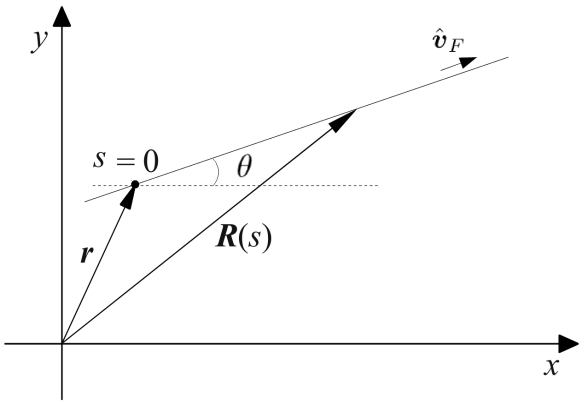

Figure 3.3: Schematic diagram of one trajectory in the direction of the Fermi velocity $\hat{\boldsymbol{v}}_F$. To find the superconductor's properties at point $\boldsymbol{r}$, one needs to consider all the possible trajectories which go through this point, i.e. all the directions of the Fermi velocity, $\theta \in [0, 2\pi]$. Parameter s shows the trajectory's path which is assumed to be zero at the given point $\boldsymbol{r}$. The vector $\boldsymbol{R}(s)$ indicates the position of the quasiparticle on the s-axis.

3.2 Numerical approach

The observables discussed in this dissertation may be directly calculated using the quasiclassical propagators. The components of the quasiclassical propagator, $f(\boldsymbol{r}, \boldsymbol{p}_F, i\varepsilon_n)$ and $g(\boldsymbol{r}, \boldsymbol{p}_F, i\varepsilon_n)$, are in general functions of the pair potential $\Delta(\boldsymbol{r}, \boldsymbol{p}_F)$, functions of the current density $\boldsymbol{j}(\boldsymbol{r})$ via the vector potential $\boldsymbol{A}(\boldsymbol{r})$, and also functions of $\Sigma^F(\boldsymbol{r}, \boldsymbol{p}_F, i\varepsilon_n)$ and $\Sigma^G(\boldsymbol{r}, \boldsymbol{p}_F, i\varepsilon_n)$ via $\tilde{\varepsilon}_n(\boldsymbol{r}, i\varepsilon_n)$ and $\tilde{\Delta}(\boldsymbol{r}, i\varepsilon_n)$ respectively. Therefore, the four equations (2.23), (2.24), (2.45) and (2.46), are coupled self-consistent equations which usually must be solved numerically.

3.2.1 Numerical iterative procedure

The algorithm shown in figure 3.4, explains briefly the self-consistent iterative calculations. We start with an initial guess for the functions $\Delta(\boldsymbol{r}, T)$, $\Sigma^F(\boldsymbol{r}, i\varepsilon_n)$, $\Sigma^G(\boldsymbol{r}, i\varepsilon_n)$ and $\boldsymbol{A}(\boldsymbol{r})$. These are used to solve the Riccati equations (2.30) and (2.31) along all real space trajectories with specular reflection on the surface $x = 0$. From the solutions we find the propagators $f(\boldsymbol{r}, \boldsymbol{p}_F, i\varepsilon_n)$ and $g(\boldsymbol{r}, \boldsymbol{p}_F, i\varepsilon_n)$ (equations (2.34) and (2.35)). These are used to obtain the updated self energies $\Sigma^F(\boldsymbol{r}, i\varepsilon_n)$ and $\Sigma^G(\boldsymbol{r}, i\varepsilon_n)$ (equations (2.45) and (2.46)), the current density $\boldsymbol{j}(\boldsymbol{r}, T)$ (equation

(2.24)), and the updated pair potential $\Delta(\boldsymbol{r}, T)$ (equation (2.23)). This procedure iterates until the self consistency of the solutions is achieved.

The second step is to solve the Maxwell's equation (3.2). To do so, we used the relaxation method [56, 57]. Using the estimated functions $\boldsymbol{A}(\boldsymbol{r})$ and $\boldsymbol{B}(\boldsymbol{r})$ together with the updated variables from the first step, $\Delta(\boldsymbol{r}, T)$, $\Sigma^F(\boldsymbol{r}, i\varepsilon_n)$, $\Sigma^G(\boldsymbol{r}, i\varepsilon_n)$ and $\boldsymbol{j}(\boldsymbol{r}, T)$, integration of equation (3.2) yields an updated vector potential and magnetic field .

The whole procedure is iterated until the functions $\Delta(\boldsymbol{r}, T)$, $\Sigma^F(\boldsymbol{r}, i\varepsilon_n)$, $\Sigma^G(\boldsymbol{r}, i\varepsilon_n)$ and $\boldsymbol{A}(\boldsymbol{r})$ converge. One may note that the self energies $\Sigma^F(\boldsymbol{r}, i\varepsilon_n)$ and $\Sigma^G(\boldsymbol{r}, i\varepsilon_n)$ and the propagators $f(\boldsymbol{r}, \boldsymbol{p}_F, i\varepsilon_n)$ and $g(\boldsymbol{r}, \boldsymbol{p}_F, i\varepsilon_n)$ are calculated self-consistently this way.

After convergence, a final iteration is run, in which all equations are solved directly for real frequencies $i\varepsilon_n \to E + i\delta$ in order to perform an analytic continuation for the local density of states and the self energies. δ is an infinitesimal parameter and is used in order to regularize the poles of the propagators. In our calculations without impurities, it is set to $\delta = 0.007\, k_B T_c$, while in the presence of impurities it is chosen to be zero. There, the impurity self energies may prevent the divergence of the propagators.

3.2.2 Evaluation of the equations

Determining the coupling constant VN_0

VN_0 is a constant quantity, therefore we calculate it in the bulk and for the temperatures near T_c. Using the bulk propagator equation (2.26), one can rewrite the equation (2.23) as

$$\Delta_{\text{bulk}} = VN_0 \pi k_B T \sum_{|\varepsilon_n|<\omega_c} \left\langle \frac{\Delta_{\text{bulk}} \chi^2(\boldsymbol{p}_F)}{\sqrt{\varepsilon_n^2 + |\Delta_{\text{bulk}} \chi(\boldsymbol{p}_F)|^2}} \right\rangle_{FS} . \tag{3.7}$$

At $T \to T_c$, the Gap equation (3.7) can be linearized around $T = T_c$ [28] as

$$\frac{1}{VN_0} = \pi k_B T_c \sum_{|\varepsilon_n|<\omega_c} \left\langle \frac{\chi^2(\boldsymbol{p}_F)}{|\varepsilon_n|} \right\rangle_{FS} . \tag{3.8}$$

Adding and subtracting the right hand side of the equation (3.8) and using the weak coupling approximation, i.e. $\omega_c \gg 2\pi k_B T_c$, the coupling constant for a given temperature T and cut off ω_c can be replaced by

$$[VN_0]^{-1} \;\to\; \left\langle \chi^2(\boldsymbol{p}_F) \right\rangle_{FS} \left(\sum_{|\varepsilon_n|<\omega_c} \frac{1}{2n+1} + ln\left(\frac{T}{T_c}\right) \right) .$$

This calculation is done for a superconductor with d-wave symmetry. For a s-wave superconductor in which the pairing is independent of momentum, it will be smaller by a factor of $1/\langle\chi^2(\boldsymbol{p}_F)\rangle_{FS}$:

$$[VN_0]_{s\text{-wave}} = \frac{1}{\langle\chi^2(\boldsymbol{p}_F)\rangle_{FS}}\,[VN_0]_{d\text{-wave}}\,.$$

Summation over all the Matsubara frequencies

To evaluate the equations (2.23) and (2.24), one should sum the averaged functions $\langle\chi(\boldsymbol{p}_F)f(\boldsymbol{r},\boldsymbol{p}_F,i\varepsilon_n)\rangle_{FS}$ and $\langle\hat{\boldsymbol{v}}_F\cdot g(\boldsymbol{r},\boldsymbol{p}_F,i\varepsilon_n)\rangle_{FS}$ over all the Matsubara frequencies up to a cut-off frequency ω_c. The cut-off frequency must be chosen sufficiently large so that the results are independent of ω_c.

In order to calculate the gap amplitude, one needs a Fermi surface average over all momenta $\boldsymbol{p}_F$. Therefore, due to the symmetry property of the quasiclassical propagator, equation (2.19), the summation over the Matsubara frequencies for fermions can be restricted to the positive frequencies:

$$\sum_{|\varepsilon_n|<\omega_c} \to 2\sum_{0<\varepsilon_n<\omega_c} = 2\sum_{n=0}^{n_{max}},$$

where $n_{max} = \frac{1}{2}\left(\frac{\omega_c}{\pi k_B T} - 1\right)$. Due to the symmetry relation (2.20), it can be seen that this is also the case when we want to determine the current density, since only the real part of $g(\boldsymbol{r},\boldsymbol{p}_F,i\hat{\varepsilon}_n)$ is considered.

Fermi surface averaging

In this work, the Fermi surface is assumed to be cylindrical with the c-axis oriented parallel to the z-axis. Therefore, the Fermi velocity in the xy-plane is determined by $\boldsymbol{v}_F = v_F(\cos\theta\hat{\boldsymbol{x}} + \sin\theta\hat{\boldsymbol{y}})$, where the angle θ is measured relative to the x-axis and v_F is assumed to remain constant. Thus the average over the Fermi surface may be represented as

$$\langle\cdots\rangle_{FS} = \frac{1}{2\pi}\int_0^{2\theta}\cdots\, d\theta.$$

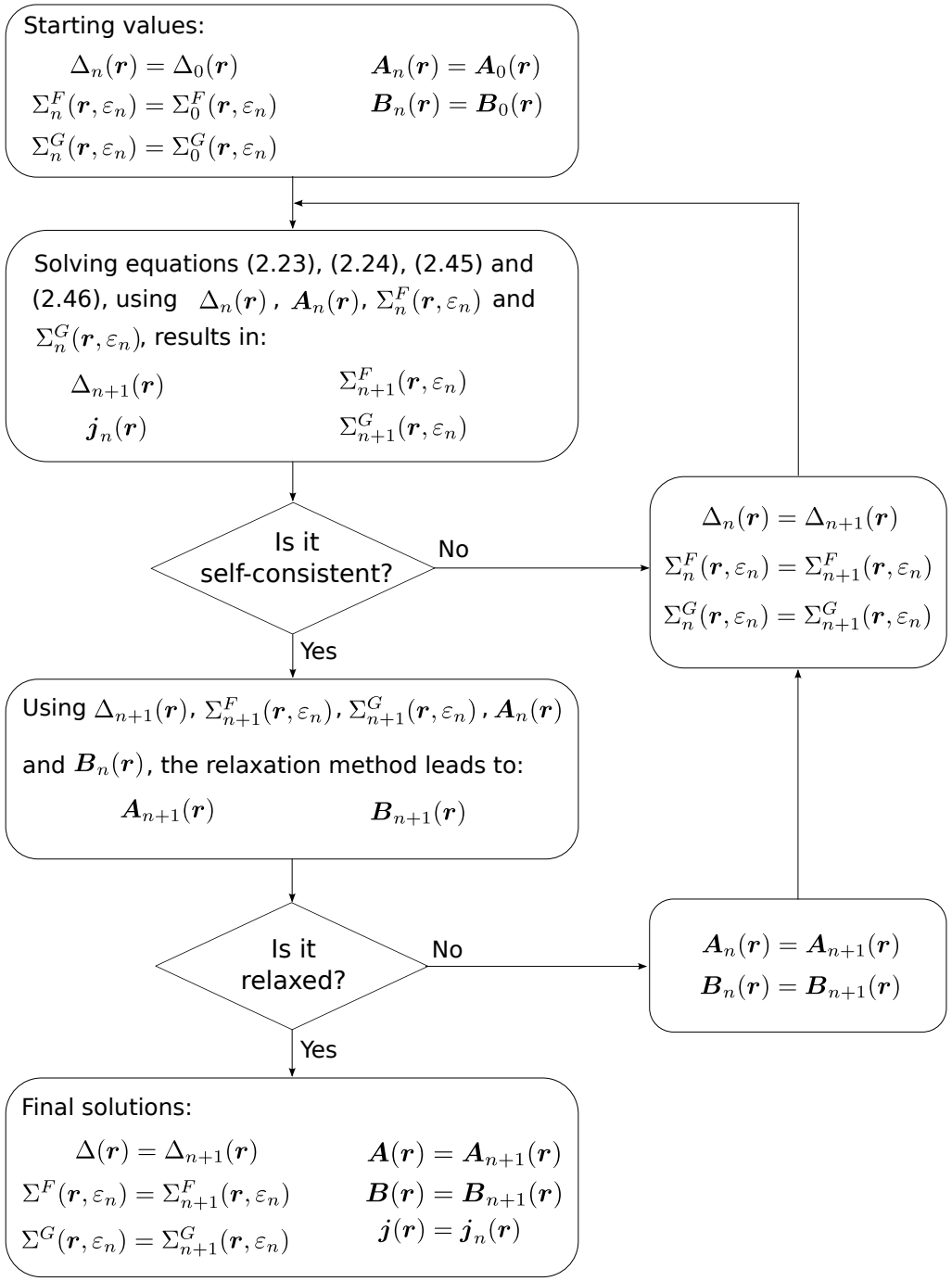

Figure 3.4: The schematic algorithm indicating the numerical procedure. It starts with an initial guess for the functions $\Delta(\boldsymbol{r}, T)$, $\Sigma^F(\boldsymbol{r}, i\varepsilon_n)$, $\Sigma^G(\boldsymbol{r}, i\varepsilon_n)$ and $\boldsymbol{A}(\boldsymbol{r})$, solves the Riccati equations and determines an updated set of variables. The procedure iterates until a self-consistency of the solutions is achieved. The resulting functions are used to solve the Maxwell's equation, the solutions of which are the updated functions $\boldsymbol{A}(\boldsymbol{r})$ and $\boldsymbol{B}(\boldsymbol{r})$. The whole process iterates until a convergence of all the functions is achieved.

3.2.3 Normalization

All the quantities calculated in this work are dimensionless normalized parameters.

- Any length is scaled to $\pi\xi_0$, where ξ_0 is the zero temperature coherence length without impurities and is given by $\xi_0 = \frac{\hbar v_F}{\pi\Delta(\hat{T}=0)} = \frac{\hbar v_F}{\pi\Delta_0}$.

- Temperature is normalized to the critical temperature T_c and all quantities with energy dimension are normalized to $k_B T_c$:

$$\hat{T} \equiv \frac{T}{T_c}, \quad \hat{\varepsilon}_n \equiv \frac{\varepsilon_n}{k_B T_c}, \quad \hat{\omega}_c \equiv \frac{\omega_c}{k_B T_c}, \quad \hat{\Sigma}(\hat{\boldsymbol{r}}, i\varepsilon_n) \equiv \frac{\Sigma(\hat{\boldsymbol{r}}, i\varepsilon_n)}{k_B T_c}. \tag{3.9}$$

  The gap equation (2.23) is of the form

$$\hat{\Delta}\left(\hat{\boldsymbol{r}}, T\right) \equiv \frac{\Delta\left(\hat{\boldsymbol{r}}, T\right)}{k_B T_c} = V N_0 \pi \hat{T} \sum_{|\hat{\varepsilon}_n|<\hat{\omega}_c} \left\langle \chi(\boldsymbol{p}_F) f(\hat{\boldsymbol{r}}, \boldsymbol{p}_F, i\hat{\varepsilon}_n) \right\rangle_{FS}. \tag{3.10}$$

- The normalization of the current density is obtained from

$$\hat{\boldsymbol{j}}\left(\hat{\boldsymbol{r}}, T\right) = \frac{\boldsymbol{j}\left(\hat{\boldsymbol{r}}, T\right)}{e N_0 v_F k_B T_c} = 2\pi \hat{T} \sum_{|\hat{\varepsilon}_n|<\hat{\omega}_c} \left\langle \hat{\boldsymbol{v}}_F \cdot g\left(\hat{\boldsymbol{r}}, \boldsymbol{p}_F, i\hat{\varepsilon}_n\right) \right\rangle_{FS}. \tag{3.11}$$

- Maxwell's equation $\boldsymbol{\nabla} \times \boldsymbol{B} = \mu_0 \boldsymbol{j}$ is also normalized as follows

$$\boldsymbol{\nabla} \times \boldsymbol{B} = \mu_0 e N_0 v_F k_B T_c \hat{\boldsymbol{j}}\left(\hat{\boldsymbol{r}}, T\right)$$

$$\begin{aligned} \Rightarrow \hat{\boldsymbol{j}}\left(\hat{\boldsymbol{r}}, T\right) &= \frac{1}{\mu_0 e N_0 v_F k_B T_c} \boldsymbol{\nabla} \times \boldsymbol{B} \\ &= \lambda_L^2 \frac{e}{c} v_F \frac{1}{k_B T_c} \boldsymbol{\nabla} \times \boldsymbol{B}, \end{aligned} \tag{3.12}$$

  where the London penetration depth at $\hat{T} = 0$ is defined as:

$$\lambda_L^{-2}(\hat{T}=0) = \frac{e^2}{c} \mu_0 N_0 v_F^2. \tag{3.13}$$

  Using the Ginzburg-Landau parameter $\kappa = \frac{\lambda_L(\hat{T}=0)}{\xi_0}$, equation (3.12) may be written as

$$\hat{\boldsymbol{j}}\left(\hat{\boldsymbol{r}}, T\right) = \kappa^2 \xi_0^2 \frac{e}{c} v_F \frac{1}{k_B T_c} \boldsymbol{\nabla} \times \boldsymbol{B}.$$

  Defining the normalized gradient and magnetic field as

$$\hat{\boldsymbol{\nabla}} = \pi \xi_0 \boldsymbol{\nabla} \tag{3.14}$$

$$\hat{\boldsymbol{B}} = \frac{\boldsymbol{B}}{\frac{c}{e}\frac{1}{v_F} k_B T_c \frac{1}{\xi_0}}, \tag{3.15}$$

  one obtains the normalized Maxwell's equation

$$\hat{\boldsymbol{j}}\left(\hat{\boldsymbol{r}},T\right)=\kappa^{\mathbf{2}}\hat{\boldsymbol{\nabla}}\times\hat{\boldsymbol{B}}. \tag{3.16}$$

- To find the normalization of the vector potential, we use the fact that it should fulfill the relation $\hat{\boldsymbol{\nabla}}\times\hat{\boldsymbol{A}}=\hat{\boldsymbol{B}}$. So

$$\xi_0\boldsymbol{\nabla}\times\hat{\boldsymbol{A}}=\frac{\boldsymbol{B}}{\frac{c}{e}\frac{1}{v_F}k_BT_c\frac{1}{\xi_0}}.$$

  Comparing with $\boldsymbol{\nabla}\times\boldsymbol{A}=\boldsymbol{B}$, one obtains

$$\hat{\boldsymbol{A}}=\frac{\boldsymbol{A}}{\frac{c}{e}\frac{1}{v_F}k_BT_c}. \tag{3.17}$$

- The Matsubara equation (3.5) can be then normalized using equation (3.17)

$$i\hat{\tilde{\varepsilon}}_n=\frac{i\tilde{\varepsilon}_n}{k_BT_c}=i\hat{\varepsilon}_n+\hat{\boldsymbol{v}}_F\cdot\hat{\boldsymbol{A}}-\hat{\Sigma}^G. \tag{3.18}$$

- For the normalization of the Riccati equations, we rewrite first the equation (2.30), dividing all the terms by k_BT_c

$$\pi\xi_0\hat{\Delta}_0\frac{\partial}{\partial s}\hat{a}(s)+\left[2\hat{\tilde{\varepsilon}}_n(s)+\hat{\tilde{\Delta}}^{\dagger}(s)\hat{a}(s)\right]\hat{a}(s)-\hat{\tilde{\Delta}}(s)=0.$$

  Using the space normalization $\hat{s}\equiv\frac{s}{\pi\xi_0}$, one finds

$$\hat{\Delta}_0\frac{\partial}{\partial\hat{s}}\hat{a}(\hat{s})+\left[2\hat{\tilde{\varepsilon}}_n(\hat{s})+\hat{\tilde{\Delta}}^{\dagger}(\hat{s})\hat{a}(\hat{s})\right]\hat{a}(\hat{s})-\hat{\tilde{\Delta}}(\hat{s})=0. \tag{3.19}$$

  The same result is obtained for equation (2.31):

$$\hat{\Delta}_0\frac{\partial}{\partial\hat{s}}\hat{b}(\hat{s})-\left[2\hat{\tilde{\varepsilon}}_n(\hat{s})+\hat{\tilde{\Delta}}(\hat{s})\hat{b}(\hat{s})\right]\hat{b}(\hat{s})+\hat{\tilde{\Delta}}^{\dagger}(\hat{s})=0. \tag{3.20}$$

3.3 Surface effects in the clean limit

In a super clean limit, no impurity is assumed and therefore both diagonal and off-diagonal self energies are zero. Solving equation (2.23) for a nodal surface ($\alpha=\pi/4$), antinodal surface ($\alpha=0$) and an orientation between these two ($\alpha=\pi/8$), one can find the spatial variation of the pairing amplitude for different temperatures (see figure 3.5). For both orientation angles $\alpha=\pi/4$ and $\alpha=\pi/8$, a suppression of the order parameter at the surface is observed. It vanishes for $\alpha=\pi/4$ while reduces to a finite value for $\alpha=\pi/8$. This effect is due to the presence of the Andreev bound states which are not there for $\alpha=0$. On the other hand, going far from the surface results in a constant bulk value of the order parameter for both angles. This is the same result that one obtains for the orientation angle $\alpha=0$ presented in figure 3.5(a). For all angles, increasing the temperature reduces the amplitude of the pairing symmetry until the superconductivity is totally destroyed.

(a) $\alpha = 0$

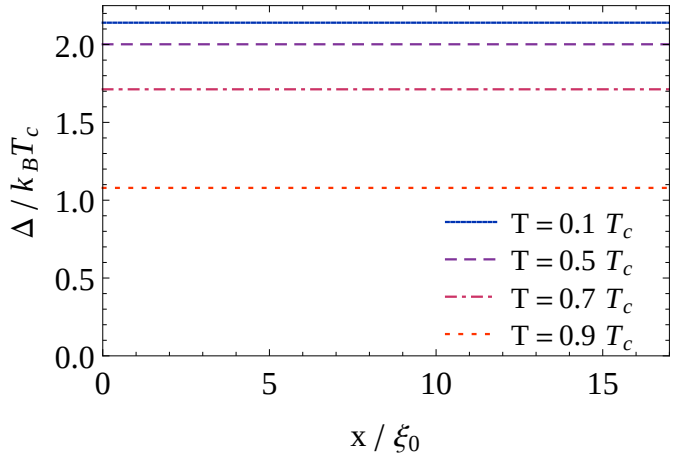

(b) $\alpha = \frac{\pi}{4}$

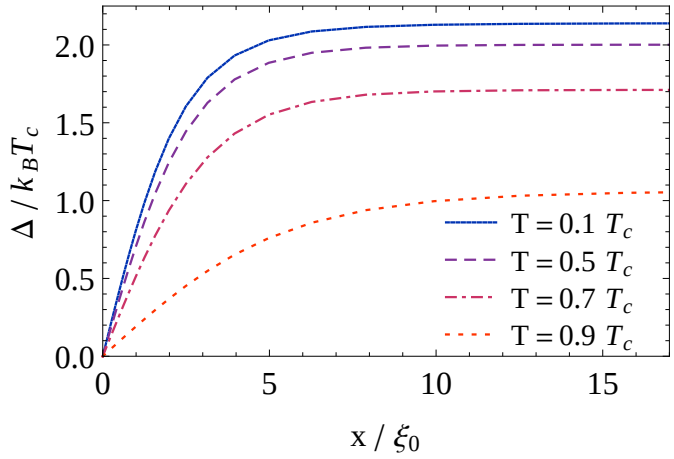

(c) $\alpha = \frac{\pi}{8}$

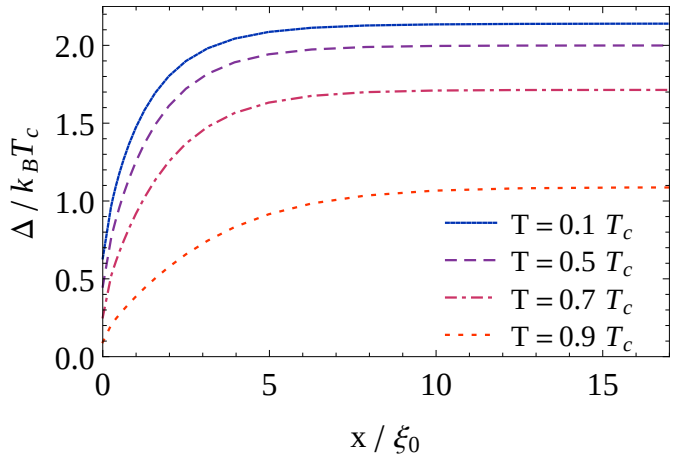

Figure 3.5: Spatial variation of the order parameter for different temperatures and (a) an antinodal surface ($\alpha = 0$), (b) a nodal surface ($\alpha = \pi/4$) and (c) an orientation in between ($\alpha = \pi/8$).

Furthermore, solving equation (2.25) for the same angles as above, gives us the opportunity to observe the existence of the zero energy Andreev bound states for specific orientations of the pairing symmetry relative to the surface normal. The result is presented in figure 3.6 for a temperature of $T = 0.1T_c$ and at the surface,

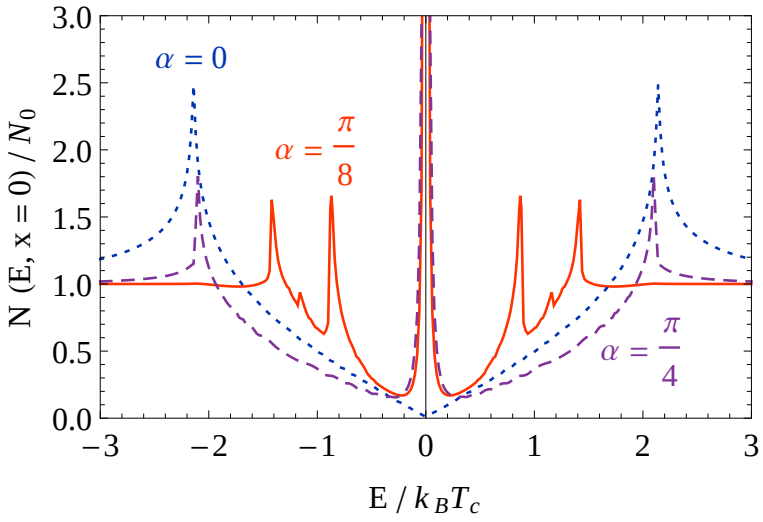

Figure 3.6: Density of bound states at the surface of a super clean d-wave superconductor for a nodal surface $\alpha = \pi/4$ (dashed), antinodal surface $\alpha = 0$ (dotted) and orientation angle $\alpha = \pi/8$ (solid). The zero-energy Andreev bound states are observed for $\alpha = \pi/4$ and $\alpha = \pi/8$, while one obtains the bulk behavior for $\alpha = 0$. Temperature is set to $T = 0.1T_c$.

$x = 0$. One may see that for d-wave orientation $\alpha = 0$, the bound states are absent. This is due to the fact that the quasiparticles will not experience a change in the sign of the pairing potential while reflecting from the surface. The effect of the surface is then defeated and one obtains the bulk behavior. Increasing the angle α leads to a gradual increase in the spectral weight of the Andreev bound states until it reaches a maximum at $\alpha = \pi/4$.

In addition to the zero energy peaks, there exist some other peaks which can be interpreted by looking at the momentum-resolved data. The peaks near $\pm 2k_BT_c$ for $\alpha = 0$ and $\alpha = \pi/4$, together with the peaks near $\pm 1.4k_BT_c$ for $\alpha = \pi/8$ are coming from quasiparticles, which approach the surface perpendicular, i.e. $\theta = 0$. They are related to $\Delta_{\text{bulk}} \cos 2\alpha$. On the other hand, as is shown in figure 3.5(c) for $\alpha = \pi/8$, the self-consistent calculation leads to a much smaller value of gap at the surface than in the bulk. Therefore, grazing angle quasiparticles mostly experience the reduced surface gap value, creating a gap edge around $\pm 0.9k_BT_c$ for this orientation angle. This is not the case for $\alpha = \pi/4$ due to the zero gap value at the surface, nor for $\alpha = 0$ due to the spatially constant gap. In figure 3.7, we have plotted the angle-resolved density of states for the case of $\alpha = \pi/8$ and two groups of trajectories: perpendicular to the surface ($\theta \sim 0$) and parallel to the surface ($\theta \sim \pi/2$). We

can observe the significant spectral weight of the bound states near $\pm 1.4 k_B T_c$ and $\pm 0.9 k_B T_c$ respectively.

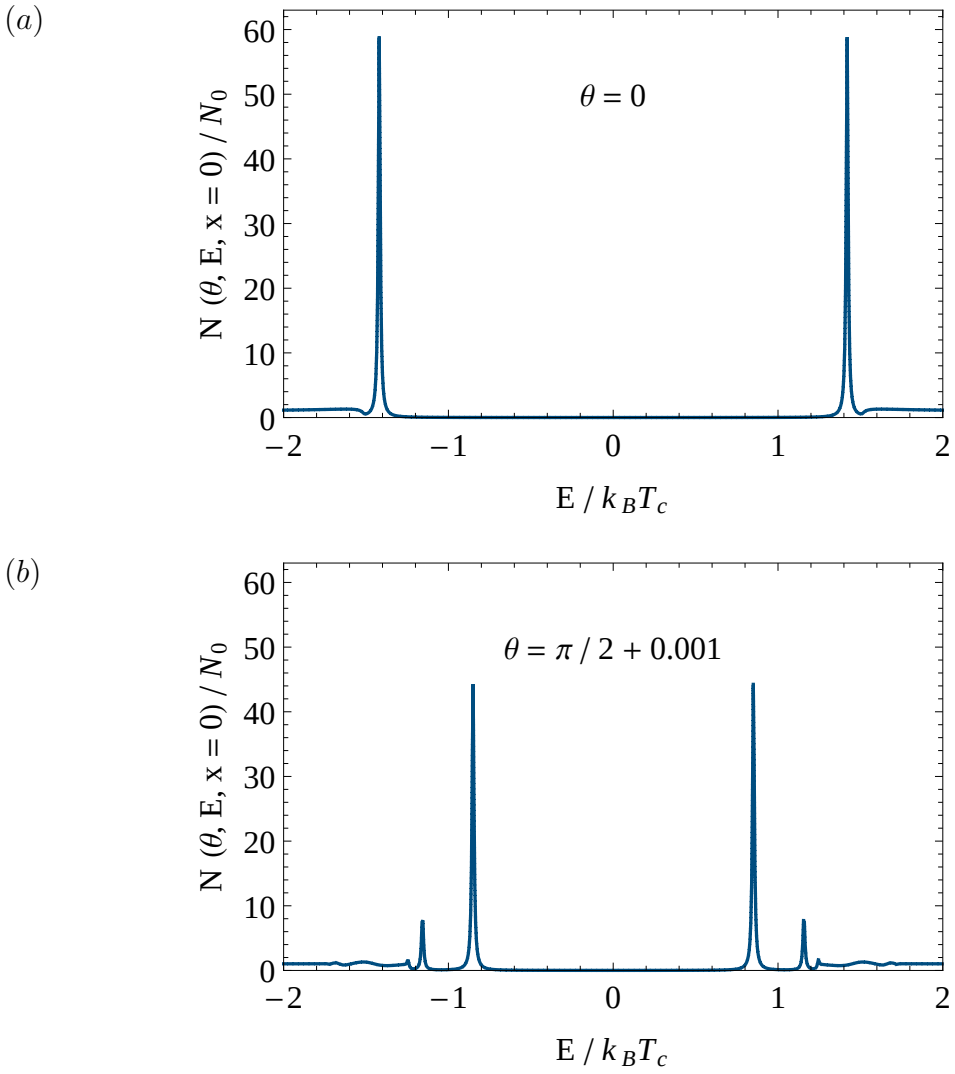

Figure 3.7: Angle-resolved density of states at the surface for orientation $\alpha = \pi/8$ at $T = 0.1 T_c$. In (a), the quasiparticles running perpendicular to the surface are considered, while in (b) the ones moving parallel to the surface. The bound states with the spectral weight $\Delta_{\text{bulk}} \cos 2\alpha$ are visible around $E \sim \pm 1.4 k_B T_c$ and the gap edge due to the grazing angles around $E \sim \pm 0.9 k_B T_c$.

3.4 Surface effects in the presence of impurity scattering

In this section we consider a superconductor containing Born impurity scatterers for the case that no external magnetic field is applied. In the bulk, the impurity scattering leads to the pair breaking. This results in a decrease of the bulk order parameter amplitude. In figure 3.8, the bulk value of the pairing potential for

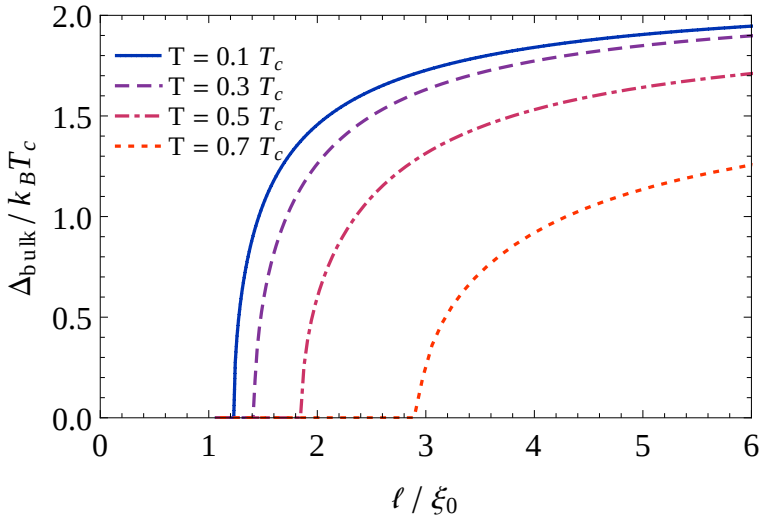

Figure 3.8: Bulk value of the pair potential as a function of normalized mean-free path ℓ/ξ_0 for different temperatures. For the values of the mean-free path comparable to the coherence length, the pair potential vanishes and therefore there exists no real dirty limit for d-wave superconductors.

different impurity concentrations is plotted. One can see that decreasing ℓ leads to an almost linear reduction of the gap until the mean free path becomes comparable to the finite temperature coherence length. Below that, the pairing amplitude is suppressed and decreases rapidly to zero. Therefore, one can say that for d-wave superconductors no real dirty limit exists; there is no need to consider the dirty limit, as long as the material is in a superconducting state.

Reduction of the pairing potential amplitude not only happens in the bulk, but also for all distances from the surface. The spatial variation of the pairing potential for different impurity concentrations is shown in figure 3.9. A comparison between different angles of the pairing potential relative to the surface normal is also given.

(a) $\alpha = 0$

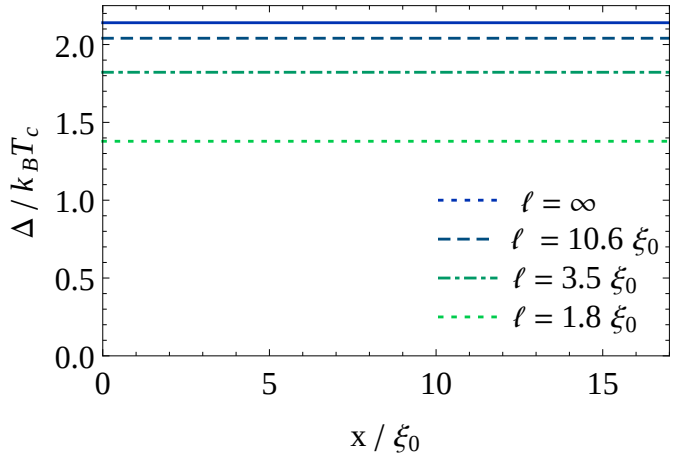

(b) $\alpha = \frac{\pi}{4}$

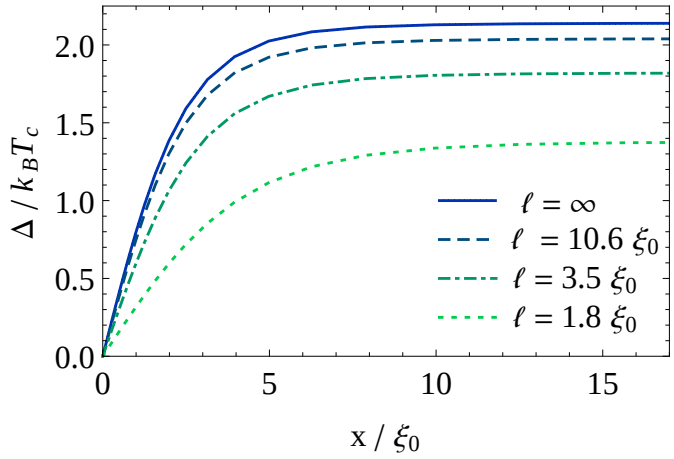

(c) $\alpha = \frac{\pi}{8}$

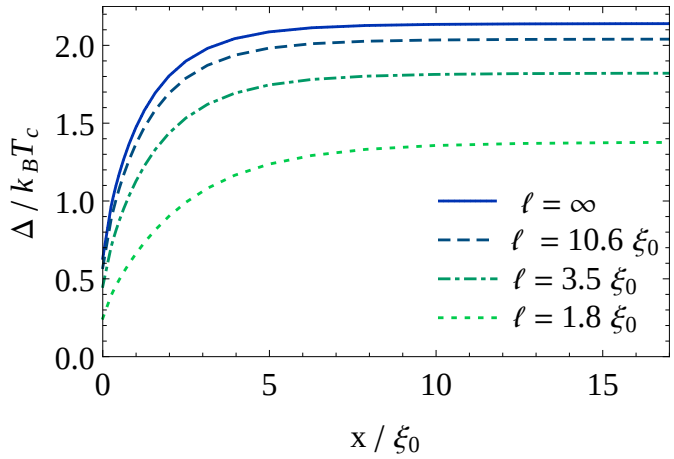

Figure 3.9: Dependency of the spatial variation of pairing potential on the impurity concentration. The calculations are done at $T = 0.1T_c$ and for $\alpha = 0$ (a), $\alpha = \pi/4$ (b) and $\alpha = \pi/8$ (c). It can be seen that for all the distances from the surface, the gap amplitude reduces with increasing impurity concentration.

In the following, we will first focus on an intermediate angle of $\alpha = \pi/8$, where the spectral weight is neither absent nor fully developed. As the Andreev bound states are more emphasized at lower temperatures, we choose the temperature $T = 0.1T_c$ for most of the calculations.

In the bulk of d-wave superconductors, the anomalous self-energy Σ^F is zero while the normal self-energy Σ^G is constant. Figure 3.10 shows how the impurities

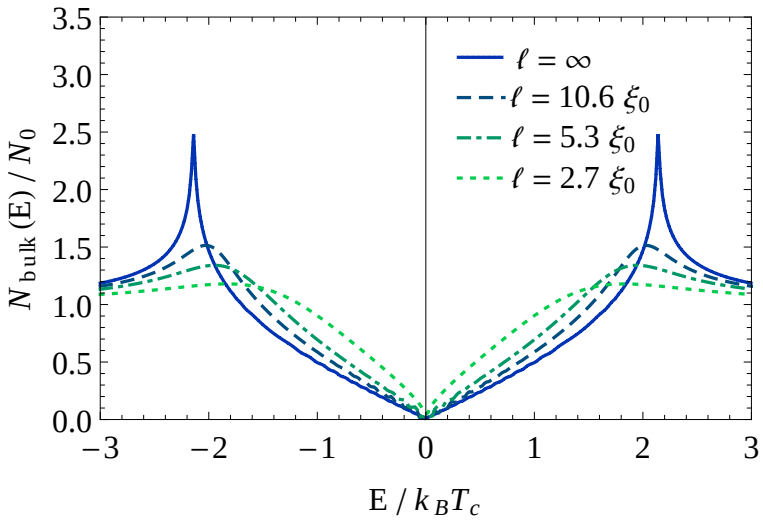

Figure 3.10: Local density of states in the bulk for different mean free paths. The coherence peak smears out even for low scattering rates. This plot is for $T = 0.1T_c$ and $\alpha = \pi/8$. Due to the symmetry however, the result is the same in the bulk for any given α.

affect the density of states in the bulk. We can see that the coherence peak smears out even for low impurity concentrations. Also, it moves to lower energies since the bulk order parameter reduces by higher impurity concentrations.

In the presence of the Andreev bound states at the surface, one expects different results. Since the local quasiparticle scattering rate is given by the negative imaginary part of the normal self-energy $-\mathrm{Im}\ \Sigma^G$, we have considered this quantity in figure 3.11. There, the temperature is chosen to be $T = 0.1T_c$ and the mean-free path is $\ell = 2.7\xi_0$. As could be expected, the largest quasiparticle scattering rate is observed at the surface and for $E = 0$. Far from the surface, it reduces to the bulk constant value. For the present set of variables, figure 3.11(b) indicates that the surface effects result in a scattering rate around 12 times larger than in the bulk. The physical understanding of the surface effects here can be gained from equation (2.46). The zero-energy bound states are low energy states which are more effective for the scattering process. Presence of zero-energy Andreev bound states at this low energy, creates a larger phase space for such states. Therefore, the impurity scattering process becomes more significant at the surface than in the bulk.

(a)

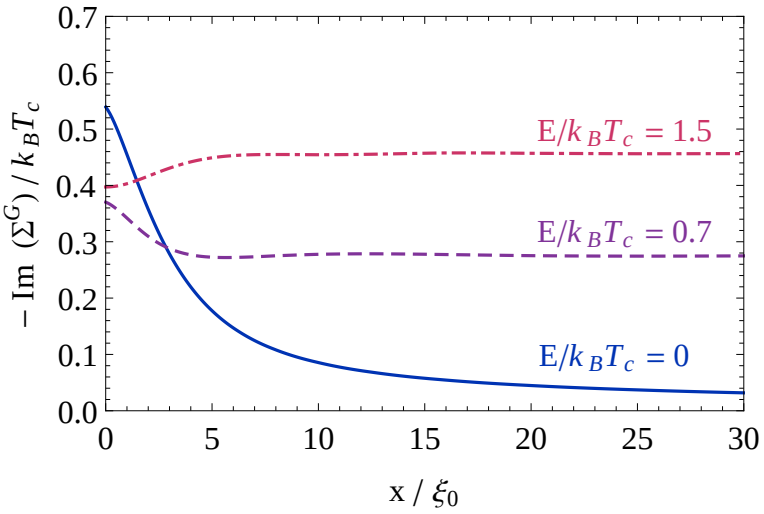

(b)

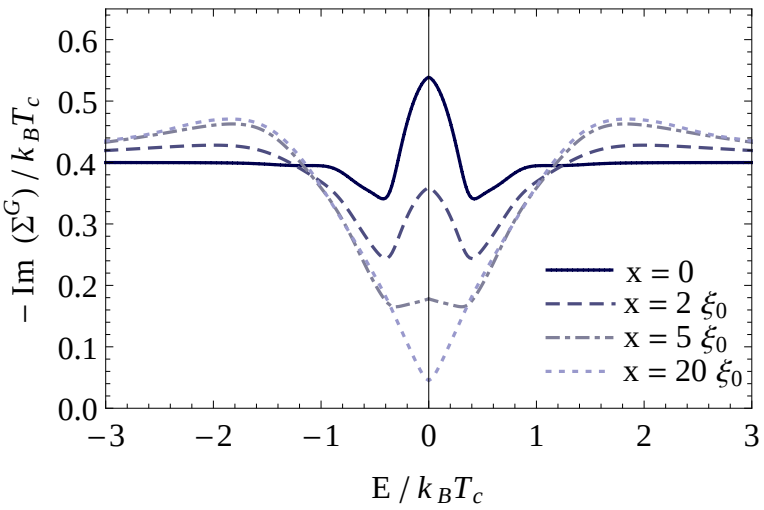

Figure 3.11: The negative imaginary part of the normal self-energy $-\mathrm{Im}\ \Sigma^G$, indicating the scattering rate. This parameter is plotted as a function of distance from the surface in part (a) and as a function of the energy in part (b). For both cases the orientation angle $\alpha = \pi/8$, the temperature $T = 0.1T_c$ and the mean-free path $\ell = 2.7\xi_0$ is chosen. A significant scattering rate is gained at the surface, as a result of the zero-energy Andreev bound states.

The considerable scattering rate at the surface can affect the density of states. The broadening expected from known results, can be well observed in figure 3.12. This broadening is proportional to the impurity scattering rate and goes hand in hand with a decrease in the height of the zero-energy peak with increasing the impurities. The calculation is done for the angle $\alpha = \pi/8$ and temperature $T = 0.1T_c$. In the presence of impurities the gap features due to the perpendicular or grazing quasiparticles are quickly washed out.

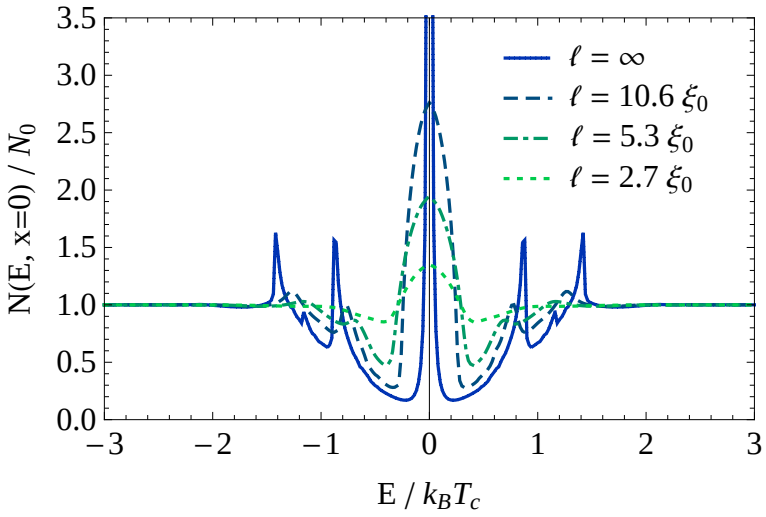

Figure 3.12: Impurity dependence of the local density of states at the surface for the temperature $T = 0.1T_c$ and the orientation angle $\alpha = \pi/8$. Increasing the scattering rate results in a decrease in the zero-energy peak height and consequently a broadening of the peak width.

3.4.1 How large is the scattering rate at the surface?

In order to have a better illustration of what impurity scattering does to the surface density of states, we make a hypothetical calculation. Therefore, we calculate again the density of states at the surface, but this time by using the bulk scattering rate at the surface, i.e. $\Sigma^G(\boldsymbol{r}) = \Sigma^G(\boldsymbol{r} \to \infty) = \text{constant}$. Then, the result is compared with the calculation using the spatial dependence $\Sigma^G(\boldsymbol{r})$ obtained from a self-consistent procedure. The comparison is shown in figure 3.13. It can be seen that the hypothetical calculation leads to a much sharper zero-energy peak in comparison with the self-consistent calculation. This implies that the Born impurity scattering is much stronger at the surface than in the bulk. The presence of the Andreev bound states at the surface creates a larger number of available scattering channels, which in turn leads to a stronger broadening of the Andreev bound states.

In order to find a better illustration of the broadening, we demonstrate the change in the peak height of the local density of states at zero energy due to decreasing the mean free path. The peak height is proportional to the inverse of the local quasiparticle scattering rate:

$$\frac{N(E=0)}{N_0} \sim \frac{k_B T_c}{-\text{Im}\ \Sigma^G(E=0)}. \tag{3.21}$$

On the other hand, one can use equation (2.46) to write the local quasiparticle scattering rate as:

$$-\text{Im}\ \Sigma^G(E=0) = \frac{1}{2\tau}\frac{N(E=0)}{N_0}. \tag{3.22}$$

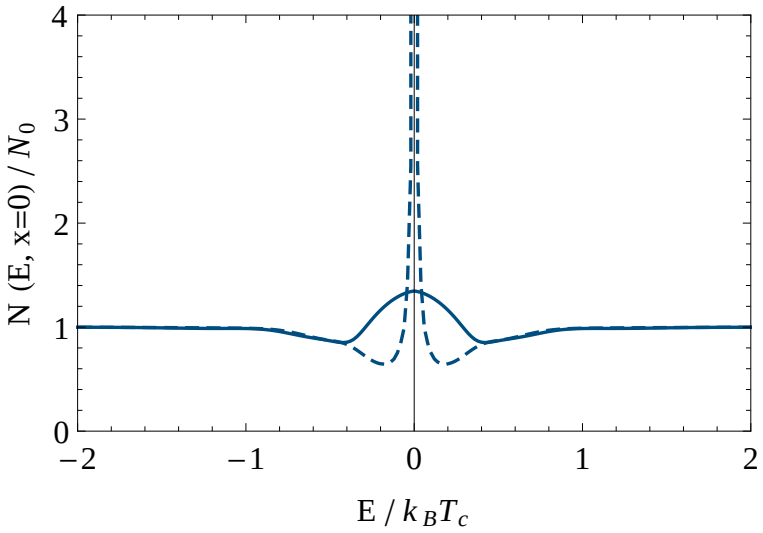

Figure 3.13: A measure of the change of the local density of states at the surface due to the impurity scattering. It compares the local density of states at the surface obtained from a self-consistent calculation for the self-energy Σ^G (the solid curve) with a hypothetical calculation using a constant bulk value for Σ^G (the dashed curve). Temperature is chosen to be $T = 0.1T_c$, orientation angle $\alpha = \frac{\pi}{8}$, and mean-free path $\ell = 2.7\xi_0$.

Solving for peak height leads to the expression

$$\frac{N(E=0)}{N_0} \sim \sqrt{2\tau k_B T_c} \sim \sqrt{\frac{\ell}{\xi_0}}. \tag{3.23}$$

It shows that the dependency of the peak height to the mean free path is proportional to $\sim \sqrt{\ell}$. In comparison to the bulk behavior of the peak height which is proportional to $\sim \ell$, a stronger impurity effect near the surface is reached. Relation (3.23) is plotted in figure 3.14. The numerical results obtained from the self-consistent calculation are also shown as filled circles, implying a very good agreement with the analytical results. Two different orientations $\alpha = \pi/4$ and $\alpha = \pi/8$ are also compared in figure 3.14. Since the maximum number of bound states are present for $\alpha = \pi/4$, the corresponding plot shows a largest slope, indicating a larger scattering strength.

3.4.2 Gap renormalization and Anderson's theorem

As discussed in subsection 2.2.1, Anderson has shown in his theorem that in an isotropic s-wave superconductor, the pairing potential and consequently the critical temperature as well as the density of states remain unaffected by nonmagnetic impurity scattering. Because of the system symmetry, the renormalization of the pair

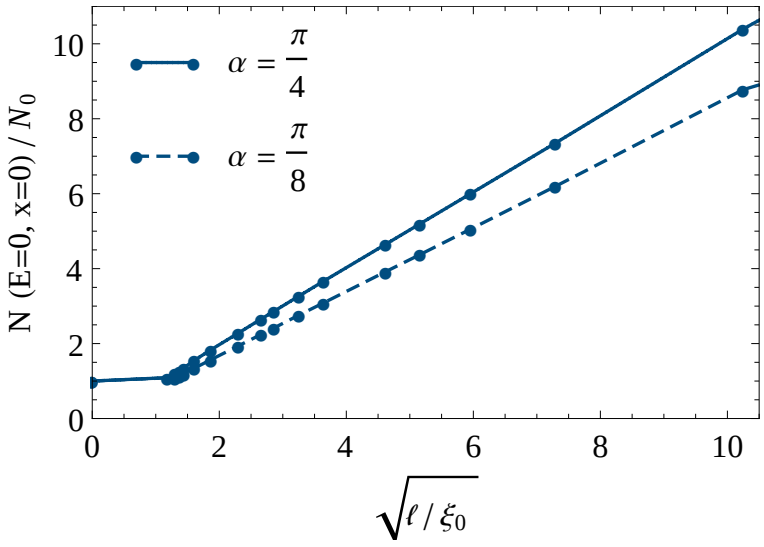

Figure 3.14: Zero energy density of states at the surface as a function of $\sqrt{\frac{\ell}{\xi_0}}$ for two different orientations $\alpha = \frac{\pi}{4}$ (solid) and $\alpha = \frac{\pi}{8}$ (dashed). The points are the numerical self-consistence results, which are in a very good agreement with the analytical calculation. Furthermore, the solid curve has a larger slope, implying a stronger scattering rate at this orientation. Temperature is $T = 0.1T_c$.

potential due to the anomalous self-energy Σ^F compensates the renormalization due to the normal self-energy Σ^G, such that their ratio remains constant and independent of the scattering. However, this is not necessarily the case in an anisotropic superconductor [58].

Unlike the normal self-energy Σ^G, it is known that the anomalous self-energy Σ^F vanishes in the bulk of a d-wave superconductor. The reason originates in the fact that due to the sign change of the pairing potential, the Fermi surface average becomes zero. This is eventually the reason why nonmagnetic impurity scattering is much more destructive to unconventional superconductors than to conventional ones. It was believed that the same situation holds at the surface of a d-wave superconductor and the gap renormalization was not taken into account. However, our study could establish that this is not generally true anymore near the surface. Due to the breaking of translational invariance near the surface, the incident and reflected quasiparticles experience different pairing potentials. Therefore different momenta k_F and $-k_F$ become inequivalent. The elimination due to the sign change is not anymore the case here and it leads to finite values of the anomalous self-energy Σ^F at the surface. Figure 3.15 shows how Σ^F varies with the distance from the surface and energy for $\alpha = \frac{\pi}{8}$. It decreases to zero in the bulk for all energies. Only for some special highly symmetric orientations of the surface relative to the pairing symmetry, the gap renormalization vanishes. These symmetric orientations are obtained when the pairing orientation relative to the surface normal is an integer

multiple of $\pi/4$. This can be seen clearly by making an α-dependent calculation of anomalous self-energy Σ^F, the result of which is plotted in figure 3.15(c). It shows that for all the energies, Σ^F vanishes for $\alpha = \frac{n\pi}{4}$ where $n \in \mathbb{Z}$.

(a)

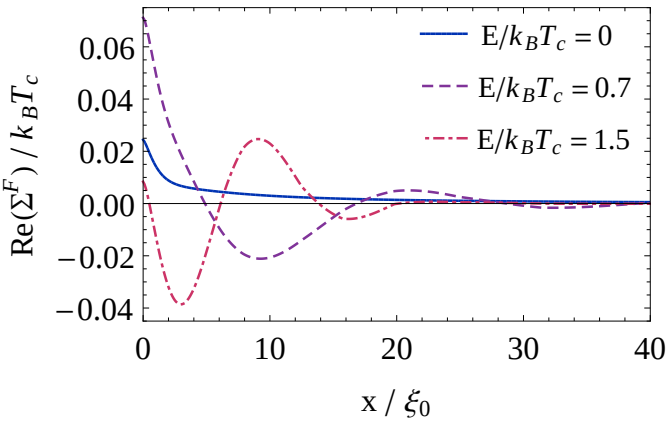

(b)

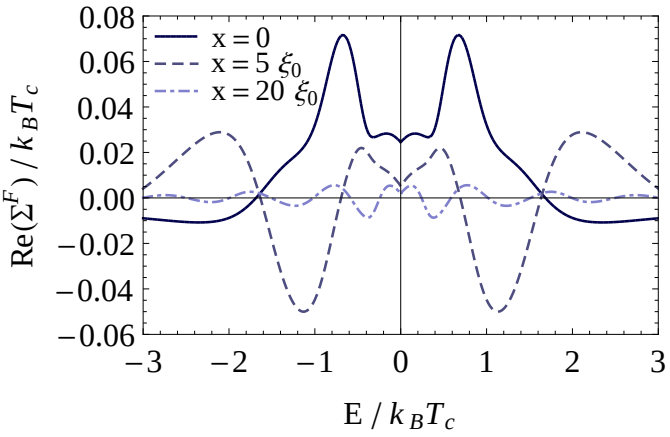

(c)

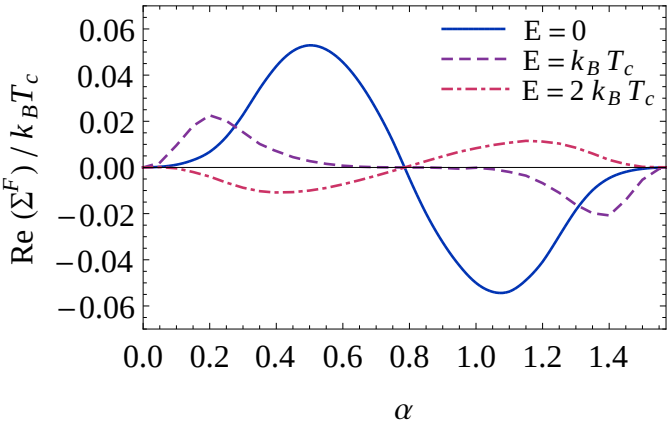

Figure 3.15: (a) Spatial dependence and (b) energy dependence of the real part of the self-energy Σ^F, implying a non-zero renormalization of the gap at the surface. In both cases, the orientation is given by $\alpha = \frac{\pi}{8}$, the mean-free path $\ell = 2.7\xi_0$, and the temperature is $T = 0.1T_c$. In (c), the real part of Σ^F at the surface vs orientation angle α is plotted. This is done for the same mean-free path as above, but at the temperature $T = 0.5T_c$. It shows that for all energies at the surface, the anomalous self-energy becomes finite except when α is an integer multiple of $\pi/4$.

3.5 Influence of an external magnetic field

In this section the influence of an external magnetic field at the surface of a d-wave superconductor is discussed. The discussion consists of two parts, the clean limit[1] and in the presence of the impurity scattering. As was explained in subsection 1.2.3, an external magnetic field splits the Andreev bound states at the surface. Furthermore, the screening current at the surface leads to a Doppler shift, implying a paramagnetic quasiparticle current. This anomalous current exists on the length scale of the coherence length and converts to the Meissner current far from the surface.

In the first part of the following section, we demonstrate these phenomena. Furthermore, we will report a nonmonotonous temperature dependence of the vector potential at the surface, which leads to a nonmonotonous influence on the size of the peak splitting. The nonlinear variation of the surface vector potential versus external magnetic field, is another significant result obtained in this part. It lead us to an in-depth study of the influence of the Andreev bound states on the nonlinear Meissner effect, the result of which is presented in chapter 4. The strength of the influence of the impurities on these magnetic effects is the content of the second part.

Since both for orientation $\alpha = \pi/4$ as well as for low temperatures the spectral weight of the Andreev bound states is strongest, we will stay with such a set of parameters, in order to illustrate the effects mentioned above more clearly. The low temperature regime is chosen to be $T = 0.1T_c$. Furthermore, the influence of the anomalous Meissner effect becomes more pronounced for small values of the Ginzburg-Landau parameter κ. Hence, in the first part we chose the value $\kappa = 10$. This value of κ is quite small in comparison of hole doped high-T_c cuprates, but may be relevant for some low T_c electron doped cuprates [59]. In the second part however, we chose $\kappa = 63$ which is a more realistic value for the hole doped high-T_c cuprates.

3.5.1 Magnetic influence in the clean limit

An external magnetic field is applied in the z direction. The screening current running parallel to the surface leads to a zero magnetic field in the interior of the superconductor. It is well known that in an isotropic superconductor, this current decays exponentially with increasing distance from the surface. However, due to the quasiparticle backflow in the presence of the Andreev bound state, the total current takes on a different shape. In order to demonstrate this difference, we did the calculations for different surfaces: an antinodal surface with $\alpha = 0$ and a nodal surface with $\alpha = \pi/4$. Figure 3.16 shows the total current density (equation 2.24)

[1] Most of the results on the influence of the magnetic field in the clean limit for $\kappa = 10$ have been published previously in reference [57].

for selected temperatures as a function of the distance from the surface. For $\alpha = 0$, the usual Meissner current is observed which has its maximum at the surface and decreases exponentially into the bulk. However, the nodal surface shows a different feature: in a distance of the order of the spatial extension of the bound states, $x \sim 3\xi_0$, the quasiparticle backflow dominates the screening current. As a result, the total current flows in an opposite direction to the screening current, as was previously shown in references [23, 26]. For $x \gtrsim 3\xi_0$, the bound states are not dominant anymore and the total current converts to the Meissner exponentially decaying current.

Looking at the surface current $j(x = 0)$ for different temperatures (figure 3.16(c)), one can see that this anomalous current persists for the full temperature range between $0.01T_c$ and $0.9T_c$. This is an evidence for the presence of Andreev bound states at the nodal d-wave surface for any temperature.

Next, we discuss the magnetic field associated with the current distribution in the interior of the superconductor. For both nodal and antinodal surfaces, the magnetic field is shown in figure 3.17. Without the Andreev bound states, an exponentially decaying magnetic field is observed for all the selected temperatures for $\alpha = 0$. On the other hand, with the anomalous Meissner current flowing at a nodal surface, the magnetic field initially increases before the normal Meissner screening sets in and eventually screens out the magnetic field exponentially. This initial increase occurs again up to a distance of $\sim 3\xi_0$ from the surface. With the value of $\kappa = 10$ we have used here, the field increases by more than a factor of 2 relative to the external field. As can be seen from equation (2.24), the smaller the penetration length, the larger the current density. Therefore, for smaller values of κ the field increase becomes more pronounced.

(a) $\alpha = 0$

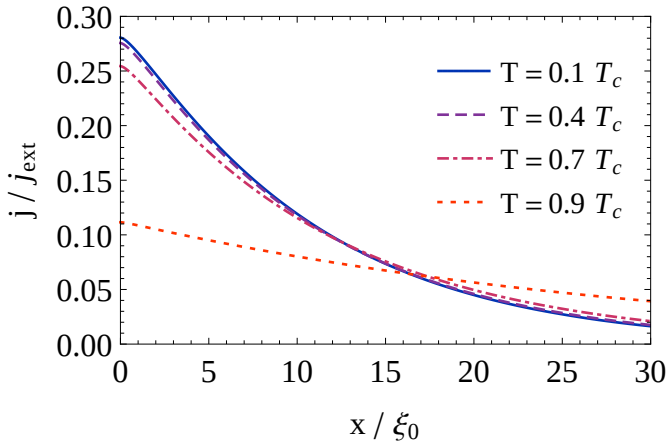

(b) $\alpha = \frac{\pi}{4}$

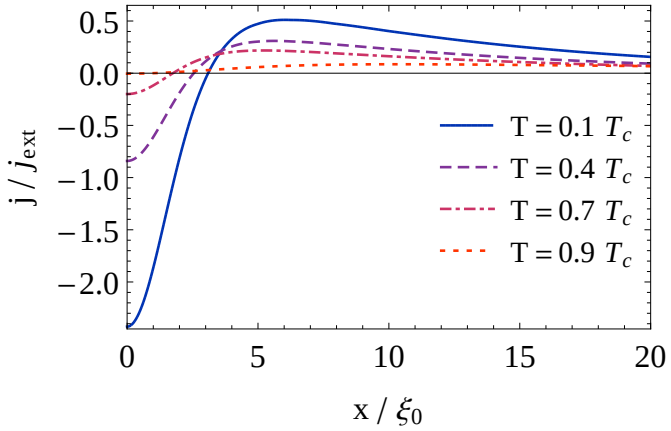

(c) $\alpha = \frac{\pi}{4}$

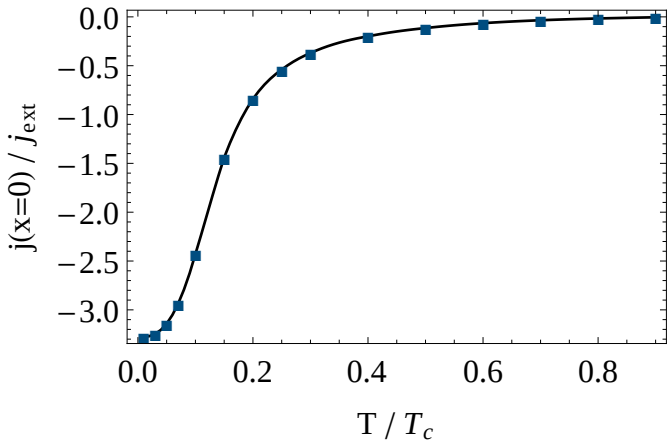

Figure 3.16: Current density distribution in the presence of an external magnetic field $B_{ext} = 0.02B_{c2}$ for orientation $\alpha = 0$ (a) and $\alpha = \frac{\pi}{4}$ (b). Due to the zero-energy bound states, the current shows an anomalous behavior in case (b), the range of it is about $x \sim 3\xi_0$. In (c), the temperature dependence of the anomalous surface current for orientation $\alpha = \frac{\pi}{4}$ is plotted. Existence of the Andreev bound states is observed for the full temperature range. For all plots, the current density has been normalized to $j_{ext} = \frac{B_{ext}}{\mu_0 \lambda_L}$.

(a) $\alpha = 0$

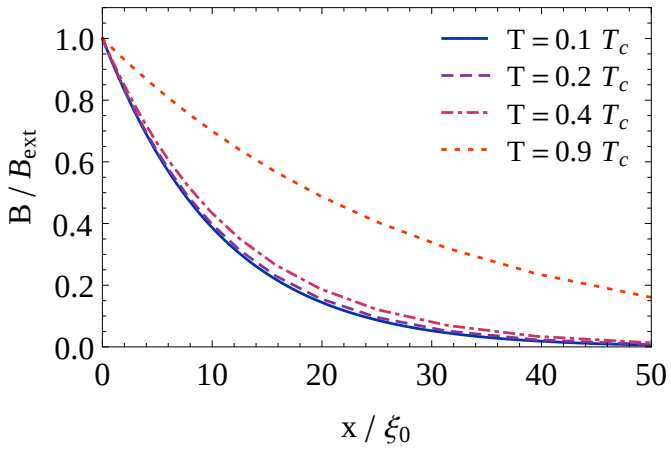

(b) $\alpha = \frac{\pi}{4}$

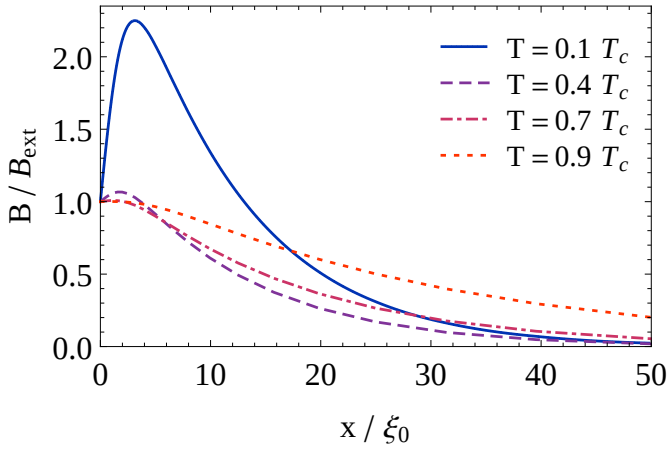

(c) $\alpha = \frac{\pi}{4}$

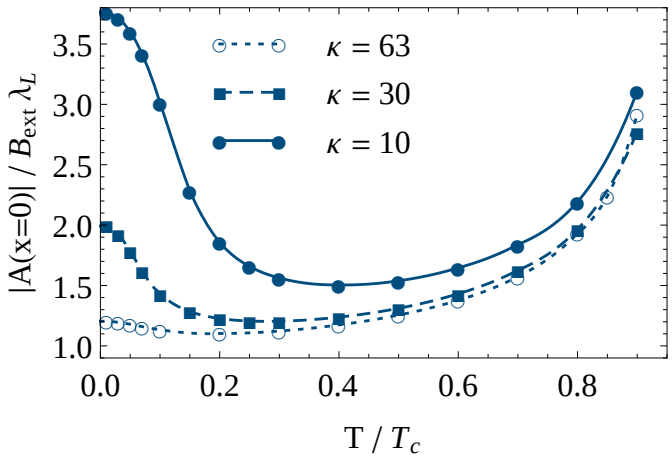

Figure 3.17: The spatial dependence of the magnetic field for orientation angles (a) $\alpha = 0$ and (b) $\alpha = \frac{\pi}{4}$ with an external magnetic field $B_{ext} = 0.02B_{c2}$. (c) Temperature dependence of the surface vector potential for orientation $\alpha = \frac{\pi}{4}$. Results are shown for $\kappa = 10$ and $B_{ext} = 0.02B_{c2}$ (filled circles), $\kappa = 30$ and $B_{ext} = 0.006B_{c2}$ (squares), $\kappa = 63$ and $B_{ext} = 0.006B_{c2}$ (open circles). Due to the peak in the magnetic field, a nonmonotonous behavior of the vector potential is observed at low temperatures which is more emphasized for smaller values of κ.

As a next step, we look at the temperature dependence of the modulus of the vector potential at the surface. As is shown in figure 3.17(c), the temperature dependence is nonmonotonous; the vector potential increases both toward low temperatures as well as toward T_c. The behavior near T_c can be explained as follows: the vector potential is the integral of the magnetic field. Therefore, for a fixed external magnetic field, the vector potential depends on the penetration depth; the larger the penetration length, the larger the vector potential. On the other hand, the penetration depth diverges near T_c, implying an increase of the vector potential near T_c. The increase of the surface vector potential toward low temperatures has a different physical origin; it is directly related to the anomalous Meissner effect and the field increase shown in figure 3.17(b). There, different values of κ are also compared. It is clear that increasing the parameter κ makes the anomalous behavior less pronounced, resulting in a reduced increase of the low temperature surface vector potential. The high temperature increase which has nothing to do with the Andreev bound states, remains almost the same for all κ values.

Studying the magnetic dependence of the vector potential at the surface, could give us the chance to detect another intrinsic property of the Andreev bound states. Their presence at the surface is found to have a significant influence on the nonlinear Meissner effect. This effect is presented in figure 3.18. For an orientation angle $\alpha = 0$, i.e. similar to the bulk results, one finds a linear dependence of the vector potential on the applied magnetic field, consistent with the known bulk studies on the nonlinear Meissner effect. For $\alpha = \pi/4$ however, sizable nonlinear corrections are visible, as a result of the Andreev bound states. Furthermore, looking at the low-field range of the order of $\sim 10^{-5} B_{c2}$, shown in figure 3.18(b), one observes again a linear response for both cases, with a considerable larger slope for $\alpha = \pi/4$.

We suppose that this surface related effect may have an significant influence on the nonlinear Meissner effect in d-wave superconductors and intermodulation distortion measurements in high-T_c microwave resonators [27, 31, 34]. Therefore, it is desirable to make a more detailed study regarding this nonlinear behavior. In chapter 4 we will give an explicit discussion about the strength and temperature dependence of the nonlinear Meissner effect at the surface.

(*a*)

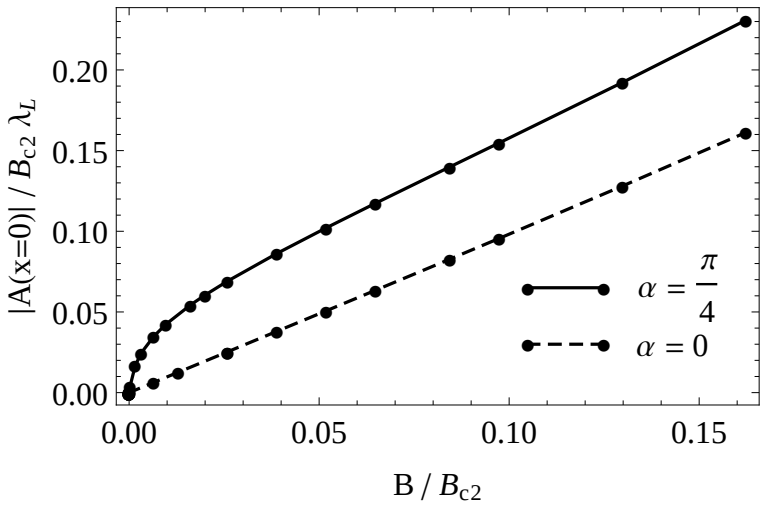

(*b*)

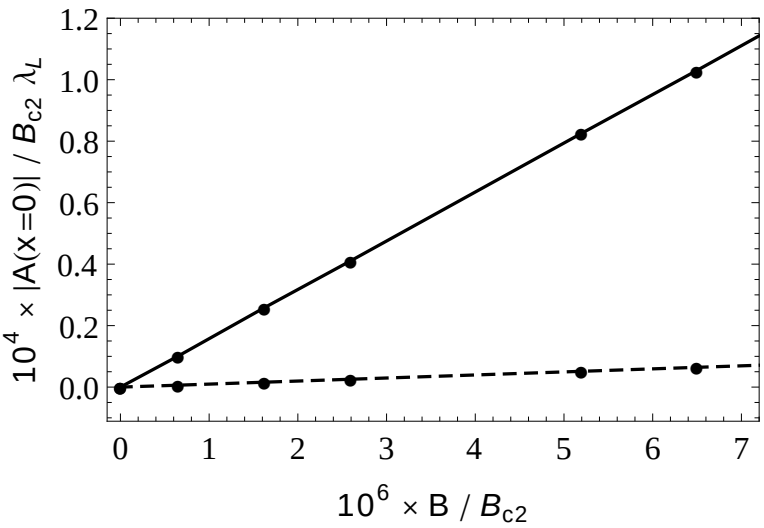

Figure 3.18: (a) Surface vector potential as a function of the external magnetic field B/B_{c2} for temperature $T = 0.1T_c$ and $\kappa = 10$. The solid line shows the result for $\alpha = \frac{\pi}{4}$ and the dashed line for $\alpha = 0$. In part (b) the low-field range is shown.

Due to the known results [23], we expect to observe the peak splitting in the local density of states imposed by the screening currents at the surface. Since the vector potential is proportional to the superfluid velocity, the nonmonotonous temperature dependence of the vector potential discussed above, has a direct influence on the size of the peak splitting in the local density of states. This effect can be clearly seen in figure 3.19, where the local density of states at the surface is plotted for different temperates. Both for low and high temperatures the splitting is significantly larger than the temperature range in between. Consequently, the peak height shows a nonmonotonous temperature dependence. Existence of such an increase in the peak splitting toward low temperatures, though less pronounced for higher values of κ, can be used as an experimental observation of the anomalous Meissner currents.

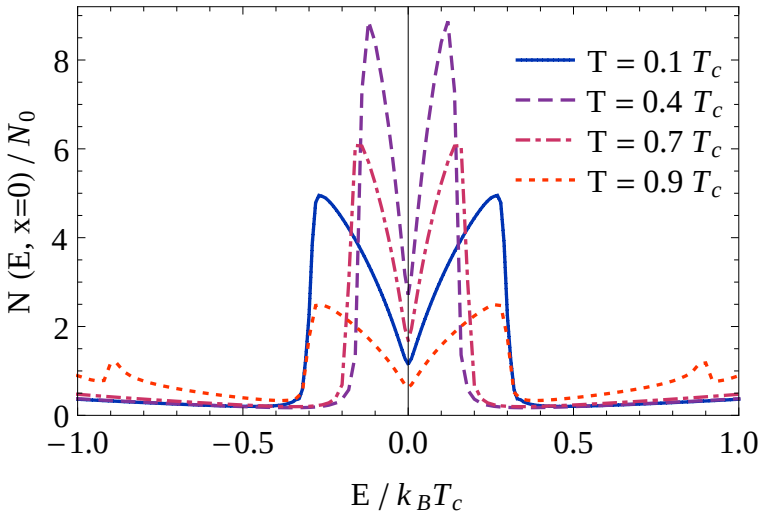

Figure 3.19: Nonmonotonous splitting of the local density of states for orientation $\alpha = \frac{\pi}{4}$ at different temperatures. The magnetic field is $B = 0.02 B_{c2}$.

3.5.2 Magnetic influence in the presence of impurity scattering

Until now we have discussed two cases, impurity scattering without an external magnetic field and the electromagnetic response in the clean limit. Now it may be interesting to know how the impurity scattering influences the magnetic properties at the surface. Therefore, we consider an external magnetic field at the surface of a d-wave superconductor which contains impurity scatterers.

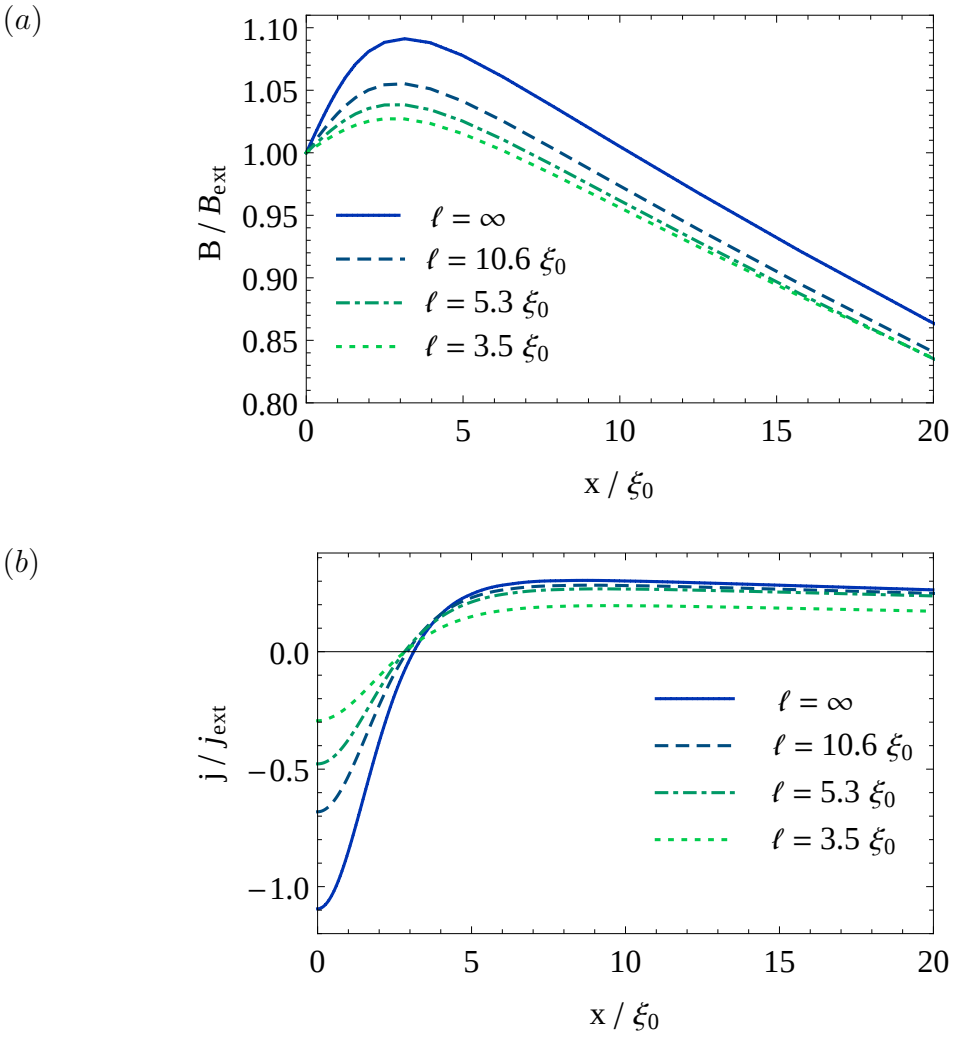

Figure 3.20: (a) Spatial variation of the external magnetic field for $\alpha = \pi/4$ and different impurity concentrations. (b) Current density distribution for the same orientation angle. For both plots, $T = 0.1T_c$, $\kappa = 63$ and the external magnetic field is $B_{ext} = 0.02B_{c2}$. In both plots, one can see that the anomalous behavior due to the zero-energy Andreev bound states reduces with increasing the impurity concentration.

Since the hole doped high-T_c cuprates have a larger value of Ginzburg-Landau parameter, we chose $\kappa = 63$ in the following calculations. Presence of impurity centers reduces the anomalous effects due to the surface bound states. The peak height in the magnetic field at the surface, as well as the anomalous surface current, are reduced with increasing impurity concentration. This effect is presented in figures 3.20(a) and (b) respectively.

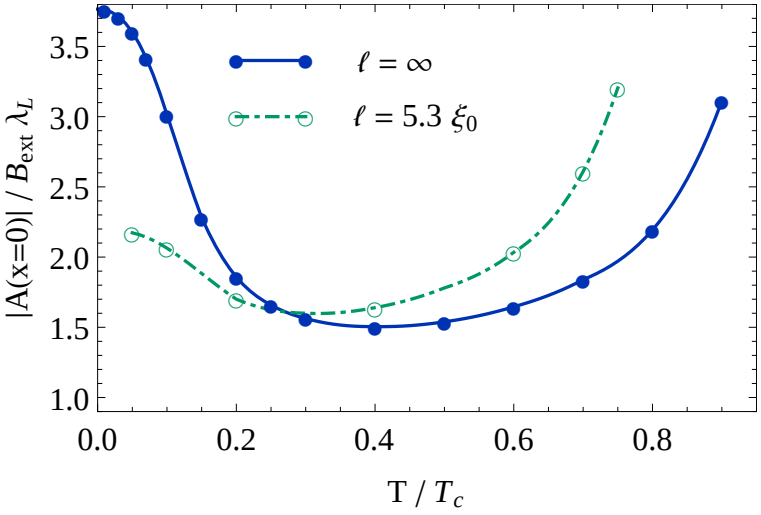

Figure 3.21: A comparison between the surface vector potential in a clean limit (filled circles) with the case including impurity scattering (open circles). The comparison is done for the following set of parameters: $\alpha = \pi/4$, $\kappa = 10$, $B_{ext} = 0.02B_{c2}$ and $\ell = 5.3\xi_0$ and the lines are guide to the eye. The low temperature increase is reduced by the impurity scattering. The increase near T_c however, is unaffected by the impurities and is only shifted to lower temperatures, due to the reduction of the bulk critical temperature with increasing impurity scattering.

The next step is to look at the impurity effect on the nonmonotonous surface vector potential presented in the previous section. Figure 3.21 gives us a comparison between two different cases, a clean superconductor and a superconductor with mean-free path $\ell = 5.3\xi_0$. The low temperature increase of the vector potential is reduced by the impurity scattering, while the increase toward T_c is shifted to lower temperatures. The latter is due to the reduction of the bulk critical temperature with increasing impurity scattering.

Regarding the density of states, one might expect that impurity scattering will wash out the peak splitting. The obtained results presented in figure 3.22(a) show a more complex behavior, however. The broadening of the zero-energy peak expected from the impurity scattering is neatly visible; the peak height is merely reduced and the peak width grows with decreasing mean-free path. The size of the peak splitting however, is robust against the impurity scattering and it remains almost the same for all values of mean-free path.

(a)

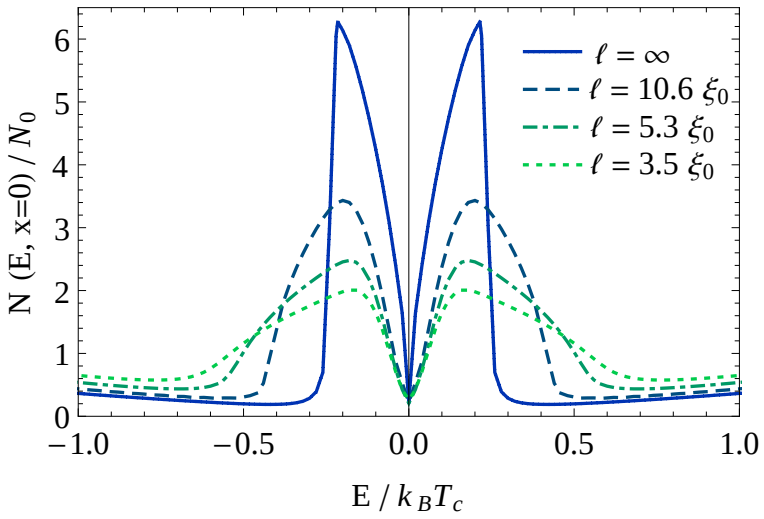

(b)

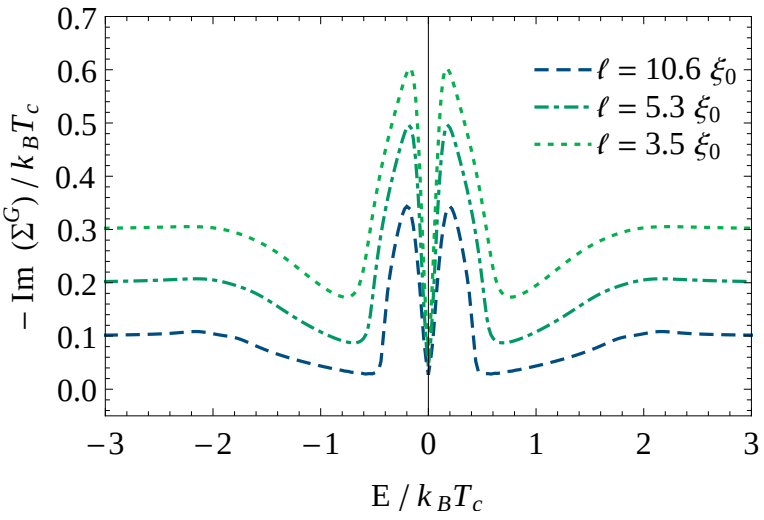

Figure 3.22: (a) Surface density of states for different impurity concentrations. Due to the impurity scattering, a significant reduction of the peak height and a growth of the peak width is observed. However, it has almost no influence on the size of the peak splitting. (b) Negative imaginary part of the self-energy Σ^G at the surface which determines the scattering strength. The external magnetic field is set to $B = 0.006 B_{c2}$, the temperature is $T = 0.1 T_c$ and the orientation angle is $\alpha = \frac{\pi}{4}$. Due to the Doppler-shift, the available states for the scattering process split, leading to a very small scattering rate near zero energy. Hence, the peak splitting remains unchanged against the impurity scattering.

In order to understand this surprising behavior, it is useful to look at the energy dependence of the scattering rate $\mathrm{Im}(\Sigma^G)$ for the selected impurity mean-free paths. As figure 3.22(b) shows, the quasiparticle scattering rate takes a comparatively small value around zero energy and is almost unchanged with decreasing mean-free path.

Furthermore, one can see the splitting in the scattering rate, with a width growing as the impurity concentration increases. The small scattering rate at low energies is a direct consequence of the peak splitting; due to the splitting, the available phase space for scattering processes is strongly reduced around zero energy, resulting in a small scattering rate even for small mean-free paths.

The peak splitting is present for almost all magnetic field ranges, as can be seen in figure 3.23. Applying a very small magnetic field, leads to an immediate decrease of the density of zero-energy bound states to almost zero. When the magnetic field is increased, the peak splitting does not evolve as a dip near zero energy, which gradually becomes deeper, but instead the splitting opens up like a curtain.

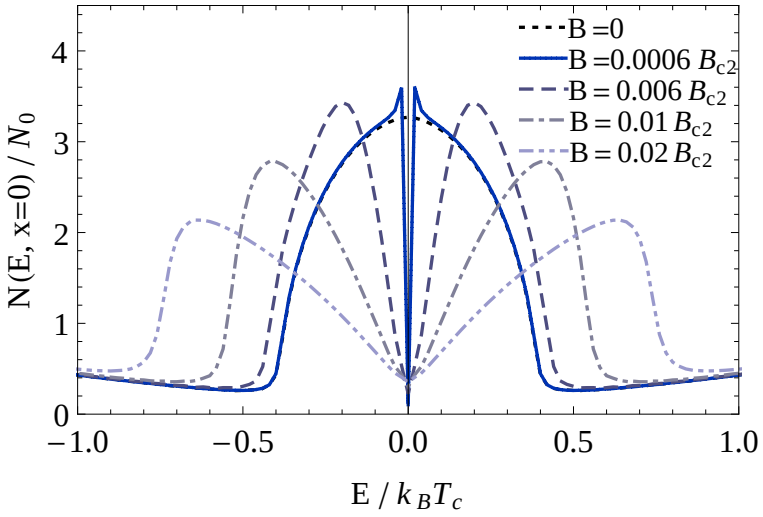

Figure 3.23: Local density of states at the surface for different external magnetic fields. The mean-free path is taken to be $\ell = 10.6\xi_0$, the temperature is $T = 0.1T_c$ and the orientation angle $\alpha = \frac{\pi}{4}$. One can see that once the external magnetic field is turned on, the density of zero-energy bound states drop to nearly zero.

As we pointed out above, in the absence of an external magnetic field the anomalous self-energy Σ^F does not vanish except for certain highly symmetric angles $\alpha = \frac{n\pi}{4}$ with $n \in \mathbb{Z}$. However, in the presence of an external magnetic field we find that even for integer multiples of $\pi/4$, the anomalous self-energy Σ^F does not vanish anymore. This is due to the fact that imposing an external magnetic field leads to a screening current flowing at the surface which can break the special reflection symmetries presented for such orientations. This gap renormalization decays far from the surface, as is shown in figure 3.24.

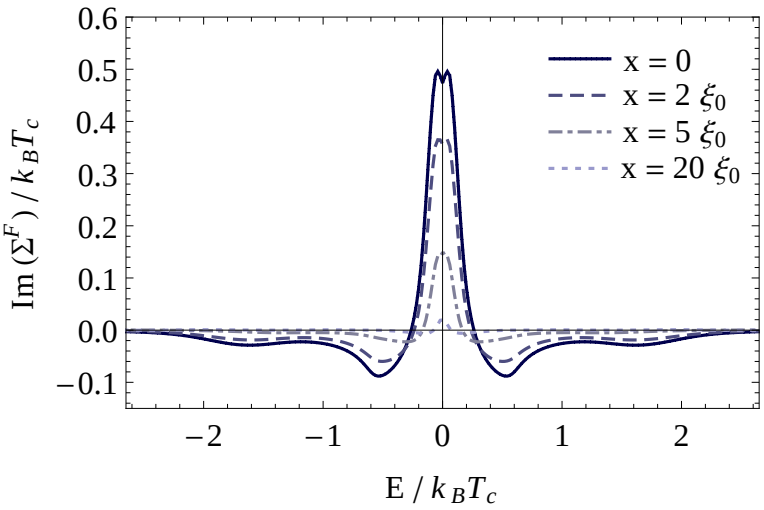

Figure 3.24: Evidence of the gap renormalization in the presence of an external magnetic field. The plot shows the imaginary part of the off-diagonal self-energy with external magnetic field $B = 0.006B_{c2}$ for orientation $\alpha = \frac{\pi}{4}$, temperature $T = 0.1T_c$ and $\ell = 3.5\xi_0$. The reflection symmetries at the surface are broken due to the surface screening current, implying a nonzero Σ^F even for $\alpha = \pi/4$ at the surface.

Chapter 4

Nonlinear Meissner effect

In this chapter, we study the influence of the surface Andreev bound states on the nonlinear Meissner effect. We found a strong modification of linear response properties in chapter 3 (see figure 3.18). Here, we want to examine the influence of this anomalous behavior on the nonlinear Meissner effect at the surface. In the following section, we give a brief explanation of the nonlinear Meissner effect and the theoretical as well as experimental evidences obtained in earlier work. These studies indicate that the linear response in the bulk follows a $1/T$ law at low temperatures, a result which we can confirm with our numerical calculations at an antinodal surface. After that in section 4.2, we will consider the contribution of surface Andreev bound states on the nonlinear Meissner effect. We can demonstrate that the nonlinear response coefficient shows a $1/T^3$ upturn for low temperatures which will dominate the bulk $1/T$ behavior at a temperature of $T/T_c \sim 1/\sqrt{\kappa}$. Finally, the total inductance L is calculated in section 4.3. This is a quantity which actually may be probed in typical intermodulation experiments, since the total response of the system, linear as well as nonlinear, is probed in such experiments.

The following calculations are done for a d-wave superconductor in the clean limit. The main results obtained in this chapter and chapter 5 are published in [60].

4.1 Nonlinear Meissner effect in bulk d-wave superconductors

In the limit of $\xi \ll \lambda$, the spatial variation of the superfluid condensate velocity $\boldsymbol{v}_s$ is very slow in comparison with the spatial variation of the quasiparticles, implying a uniform superflow on the scale of ξ [27, 30]. Therefore, the current density is given by

$$\boldsymbol{j} = ne\boldsymbol{v}_s - \boldsymbol{j}_{qp}. \tag{4.1}$$

The first term is the diamagnetic superfluid flow of the condensate and the second term is the quasiparticle backflow, the paramagnetic current which is given in the BCS form [30]

$$\boldsymbol{j}_{qp} = -2eN_0 \int_{-\infty}^{\infty} \mathrm{d}\epsilon_p \int \frac{\mathrm{d}\theta}{2\pi} \boldsymbol{v}_p f \left[\sqrt{\epsilon_p^2 + \Delta^2(\theta)} + m\boldsymbol{v}_p \cdot \boldsymbol{v}_s \right]. \tag{4.2}$$

The quasiparticle backflow depends nonlinearly on the condensate velocity $\boldsymbol{v}_s$. Unless the depairing critical current is reached, this dependency is small for s-wave superconductors. However, in d-wave superconductors, quasiparticles near the gap nodes lead to an intrinsic nonlinear electromagnetic response [27]. In s-wave superconductors, the magnetic field dependency of the penetration depth correction at low temperatures is quadratic. However, *Yip* and *Sauls* showed that in a d-wave superconductor the nonlinear Meissner effect appears as a linear magnetic field dependence of the penetration depth at low temperatures [27, 28]

$$\frac{\delta\lambda}{\lambda(\boldsymbol{H}=0)} \propto |\boldsymbol{H}|\,.$$

They suggested that measuring such a dependency at very low temperatures in systems without impurities, can provide a tool to determine d-wave pairing.

However, the nonlocal effects are not taken into account in these descriptions. Since in cuprate superconductors $\lambda/\xi_0 \gg 1$, it is reasonable to consider also the nonlocal effects. *Li et al.* [35] showed that the nonlocal effects may mask the nonlinear Meissner effect and make it unobservable. They have shown that there is a crossover magnetic field $\boldsymbol{H}^*$ below which the nonlocal effects may dominate the nonlinear Meissner effect, leading to a quadratic magnetic dependency of the penetration depth: $\delta\lambda \propto \boldsymbol{H}^2$ (see figure 4.1). This crossover field depends on the orientation of the current density with respect to the surface and for most of the cases $|\boldsymbol{H}^*| \geq H_{c1}$. Thus, the nonlinear Meissner effect regime is not accessible in such a case.

Dahm and *Scalapino* suggested a more sensitive method in order to probe the pairing symmetry: temperature dependent intermodulation distortion or harmonic generation experiments [29, 30]. They demonstrated that the temperature dependency of the penetration depth is given by

$$\lambda(j,T) \simeq \lambda(T) \left[1 + \frac{1}{2} b_\Theta(T) \left(\frac{j}{j_c} \right)^2 \right].$$

Here, j_c is the pair breaking current density and $b_\Theta(T)$ is the nonlinear coefficient depending on both the temperature and the direction of the superfluid flow. As shown in figure 4.2(a), for a superconductor with a d-wave pairing the nonlinear response coefficient shows an upturn at low temperatures following a $1/T$ law in a

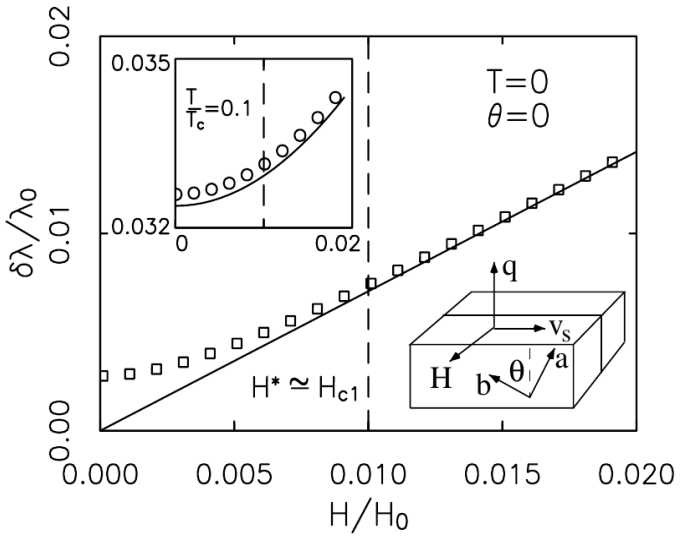

Figure 4.1: Penetration depth correction relative to the external magnetic field at $T = 0$. Here, the applied magnetic field $\boldsymbol{H}$ is parallel to the (010) surface, i.e. $\theta = 0$. θ is the orientation of the crystal b-axis with respect to the surface normal $\hat{q}$. The solid lines are calculations in which the nonlocal effects are neglected. The empty circles and squares are the full response measurements. The sample has the Ginzburg-Landau parameter $\kappa = 100$ and therefore the lower critical field is given by $H_{c1} \sim 0.01 H_0$. It is shown in [35] that in such a geometry with antinodal surface, $|\boldsymbol{H}^*| \sim H_{c1}$. This crossover field is shown with the dashed line. One can see that the linear dependence of $\delta\lambda$ is effectively unobservable. The inset shows the same result for the finite temperature $T = 0.1 T_c$. Additive to the zero temperature case, the thermal effects are also present here and thus the solid curve shows almost a quadratic feature. It means that even for such a low temperature and without nonlocal effects, the nonlinear Meissner effect can not be visible. (Adapted from [35], Copyright © (1998) by the American Physical Society).

clean system (the solid and dotted curves). As a comparison, the nonlinear coefficient for an isotropic s-wave symmetry is also plotted (the dashed curve). It goes to zero for low temperatures, implying the absence of the nodes in the gap.

However, for temperatures lower than $\sim 1/\kappa$, the nonlocal effects [35] as well as the impurity scattering [34] lead to a cut-off in the $1/T$ divergency. In figure 4.2(b) the nonlinear coefficient is shown for different impurity concentrations. It shows a saturation of the $1/T$ upturn due to the scattering process which decreases to lower values with increasing scattering rate.

Such a behavior has been observed in intermodulation distortion experiments on high-T_c cuprate superconductors [31, 32, 61]. In figure 4.3 two experimental examples are given which both neatly confirm the theoretical predictions.

(*a*)

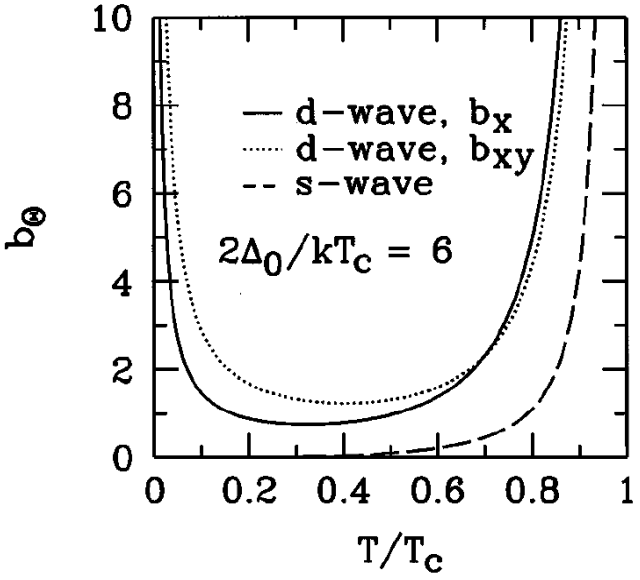

(*b*)

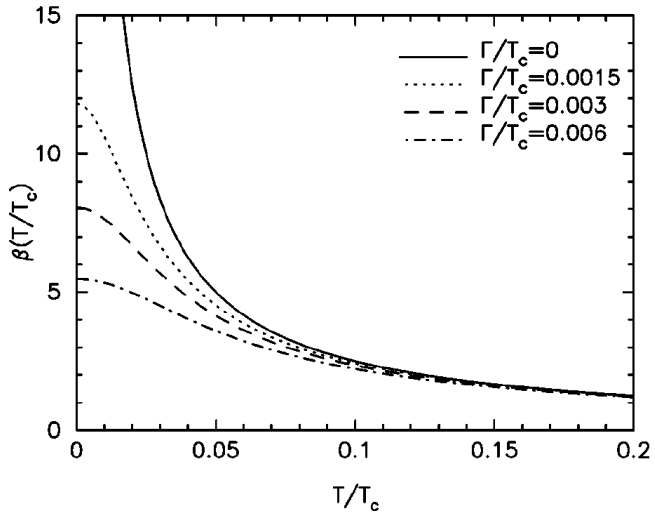

Figure 4.2: (a) Temperature dependence of the nonlinear coefficient $b_\Theta(T)$ for two different directions of $\boldsymbol{j}$ relative to the CuO bonds: along the bond b_x and 45° relative to the bond b_{xy}. The bulk gap is taken to be $2\Delta_0/k_BT_c = 6$. At low temperatures, down to the temperatures of the order $1/\kappa$ where the nonlocal effects or impurity effects become dominant, an upturn following a $1/T$ law is obtained. The saturation of the coefficient at low temperatures for an isotropic s-wave pairing is shown for comparison. (Adapted from [30], Copyright © 1997 American Institute of Physics). (b) Impurity dependence of the nonlinear coefficient at low temperatures. It shows a saturation of the $1/T$ law due to the impurity scattering effect. Increasing the scattering rate Γ reduced the nonlinearity and therefore the saturation amplitude decreases to smaller values at low temperature. (Adapted from [34], Copyright © (1999) by the American Physical Society).

(*a*)

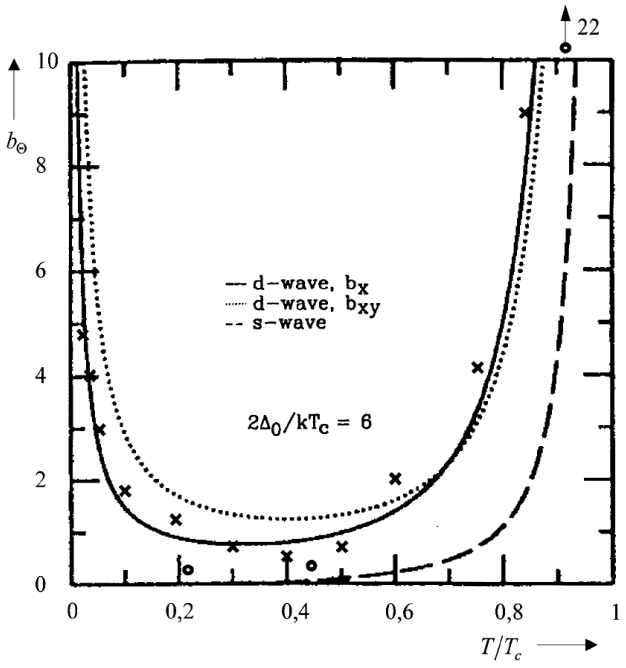

(*b*)

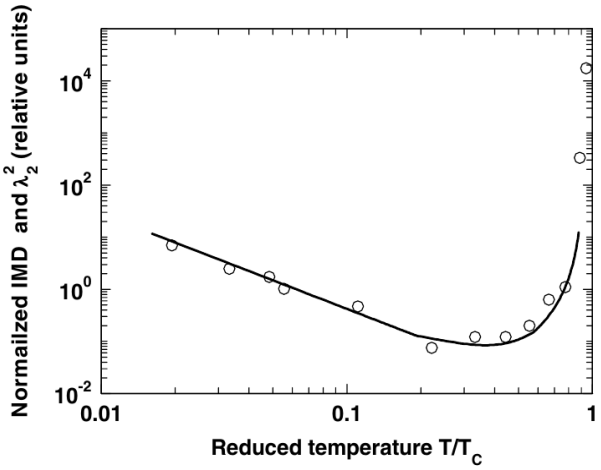

Figure 4.3: (a) The intermodulation product measurements of the nonlinearity factor b_θ versus normalized temperature T/T_c for YBCO as a d-wave sample (crosses) and for Niobium as a s-wave one (open circles). The measurements are compared with the calculations by Dahm and Scalapino (the solid and dashed lines respectively) [30]. A good agreement between both results is observed. (Adapted from [32], Copyright © 2001 Elsevier B.V). (b) Experimental evidence for observation of nonlinear Meissner effect in high quality epitaxial YBCO thin films by measuring the intermodulation distortion (IMD) at microwave frequencies versus temperature (open circles). It shows an increase in nonlinearity at low temperatures as predicted by the nonlinear Meissner effect. The solid curve is again the calculation from [30]. (Adapted from [31], Copyright © (2004) by the American Physical Society).

4.2 Nonlinear Meissner effect at the surface of d-wave superconductors

Having discussed the bulk nonlinear response, in this section we want to study the contribution of the surface Andreev bound states to the nonlinear Meissner effect. Our calculations are done in the local approximation limit, i.e. when the d-wave Cooper pairs are assumed to respond to the electromagnetic field at a single point at the center of the pair. Such an approximation is normally justified in type-II superconductors, where $\lambda \gg \xi$.

Using equation (2.24), the y component of the current density can be transformed by contour integration and analytic continuation to the real axis [28, 34]:

$$j(x) = \frac{1}{\pi} e N_0 v_F \int_{-\infty}^{\infty} \mathrm{d}E \int_0^{\pi} \mathrm{d}\theta \, \sin\theta \, f(E) \left[N_+(E, x, \theta) - N_-(E, x, \theta) \right], \tag{4.3}$$

where $f(E) = \frac{1}{1+e^{E/T}}$ is the Fermi function and $N_\pm$ denotes the normalized density of states for comoving and countermoving quasiparticles relative to the condensate flow, i.e., $N_+(E, x, \theta) = N_-(E, x, \theta - \pi)$.

After determining the current density distribution $j(x)$, the vector potential $A(x)$ and the magnetic field $B(x)$ are obtained from integration of the Maxwell's equation (3.2). Since $\kappa = \lambda/\xi_0$, for superconductors with a large value of κ the London penetration depth is much larger than the coherence length. Since the vector potential varies on the length scale of the London penetration length and the Eilenberger propagator g, and consequently the current density $j(x)$, on the length scale of the coherence length, the vector potential remains almost uniform in calculating equation (4.3). Such a local calculation of the angle resolved density of states $N_\pm(E, x, \theta)$, can be well approximated for temperatures $T/T_c \gtrsim 1/\kappa$ by a local Doppler shift of the nonlocal Eilenberger propagator g in the absence of a vector potential, i.e.

$$N_\pm(E, x, \theta) = N(E \pm e\boldsymbol{v}_F \cdot \boldsymbol{A}(x), x, \theta). \tag{4.4}$$

The Doppler shift calculation is done in the limit $\boldsymbol{A}(x) = 0$, but includes the surface Andreev bound states through the angle resolved evaluation. As in chapter 3, a real gauge is chosen in these calculations.

In order to determine the lowest order nonlinear response, we will expand the current density equation (4.3) in terms of the vector potential $A(x)$

$$j(x) = \frac{\partial j}{\partial A} \mid_{A=0} \cdot A(x) + \frac{1}{2!} \frac{\partial^2 j}{\partial A^2} \mid_{A=0} \cdot A^2(x) + \frac{1}{3!} \frac{\partial^3 j}{\partial A^3} \mid_{A=0} \cdot A^3(x) + \cdots . \tag{4.5}$$

Substituting equation (4.4) in equation (4.3), the first term is determined as

$$\frac{\partial j}{\partial A} \mid_{A=0} = \frac{1}{\pi} e N_0 v_F \int d\theta \, \sin\theta \int dE \, f(E) \, \frac{\partial (N_+ - N_-)}{\partial A}. \tag{4.6}$$

Using

$$\frac{\partial(N_+ - N_-)}{\partial A} = ev_F \sin\theta \frac{\partial(N_+ + N_-)}{\partial E} \tag{4.7}$$

and partial integration, we obtain

$$\begin{aligned}
\frac{\partial j}{\partial A}\mid_{A=0} &= \frac{1}{\pi} e^2 N_0 v_F^2 \int_0^\pi d\theta \, \sin^2\theta \int_{-\infty}^{\infty} dE \, f(E) \frac{\partial(N_+ + N_-)}{\partial E} \\
&= -e^2 v_F^2 N_0 \left(1 + \frac{1}{\pi}\int_0^\pi d\theta \, \sin^2\theta \int_{-\infty}^{\infty} dE \, \frac{\partial f}{\partial E}\,(N_+ + N_-)\right) \\
&= -e^2 v_F^2 N_0 \left(1 + \frac{2}{\pi}\int_0^\pi d\theta \, \sin^2\theta \int_{-\infty}^{\infty} dE \, \frac{\partial f}{\partial E}\, N(E,x,\theta)\right). \qquad (4.8)
\end{aligned}$$

The second derivative and generally all the even terms will cancel out due to the symmetry. For the third term we obtain similarly to the first term

$$\begin{aligned}
\frac{\partial^3 j}{\partial A^3}\mid_{A=0} &= \frac{1}{\pi} e N_0 v_F \int_0^\pi d\theta \, \sin\theta \int_{-\infty}^{\infty} dE \, f(E) \frac{\partial^3(N_+ - N_-)}{\partial A^3} \\
&= \frac{1}{\pi} e^4 N_0 v_F^4 \int_0^\pi d\theta \, \sin^4\theta \int_{-\infty}^{\infty} dE \, f(E) \frac{\partial^3(N_+ + N_-)}{\partial E^3} \\
&= -\frac{1}{\pi} e^4 N_0 v_F^4 \int_0^\pi d\theta \, \sin^4\theta \int_{-\infty}^{\infty} dE \, \frac{\partial^3 f(E)}{\partial E^3}\,(N_+ + N_-) \\
&= -\frac{2}{\pi} e^4 N_0 v_F^4 \int_0^\pi d\theta \, \sin^4\theta \int_{-\infty}^{\infty} dE \, \frac{\partial^3 f(E)}{\partial E^3}\, N(E,x,\theta), \qquad (4.9)
\end{aligned}$$

where we have used the relation

$$\frac{\partial^3(N_+ - N_-)}{\partial A^3} = e^3 v_F^3 \sin^3\theta \frac{\partial^3(N_+ + N_-)}{\partial E^3}. \tag{4.10}$$

Defining the dimensionless expansion coefficients

$$\eta_1 = 1 + \frac{2}{\pi}\int_0^\pi d\theta \sin^2\theta \int_{-\infty}^{\infty} dE \frac{\partial f}{\partial E} N(E,x,\theta) \tag{4.11}$$

and

$$\eta_3 = -\Delta_0^2 \frac{2}{\pi}\int_0^\pi d\theta \sin^4\theta \int_{-\infty}^{\infty} dE \frac{\partial^3 f}{\partial E^3} N(E,x,\theta), \tag{4.12}$$

the following expression for the current density is found

$$j(x) = -e^2 v_F^2 N_0 \eta_1(x) A(x) + \frac{e^4 v_F^4 N_0}{6\Delta_0^2}\eta_3(x) A^3(x) + \mathcal{O}(A^5). \tag{4.13}$$

Here, Δ_0 is the bulk amplitude of the pairing potential at zero temperature. The coefficient η_1 describes the linear response, while the coefficient η_3 determines the lowest order nonlinear response. In the following, the behavior of these two coefficients are discussed for two limiting cases: an antinodal surface $\alpha = 0$ and a nodal surface $\alpha = \pi/4$.

4.2.1 At an antinodal surface

Since the Andreev bound states are absent at the surface with $\alpha = 0$, one expects to obtain the bulk results. To test this consistency criterion, we have plotted the spatial variation of both η_1 and η_3 at a given temperature $T = 0.1T_c$, figure 4.4. Both expansion coefficients are constant over the whole superconducting area, confirming the known bulk calculations [30, 34].

Furthermore, the linear response η_1 shows a linear temperature dependence while the nonlinear coefficient η_3 follows a $1/T$ law at low temperatures. These results which are also consistent with the bulk properties are shown in figure 4.5, where the modulus of both parameters is plotted in a double logarithmic scale.

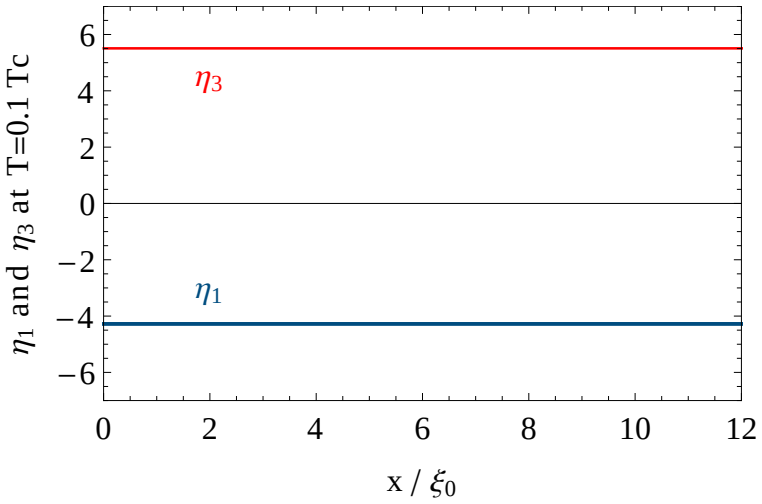

Figure 4.4: Spatial variation of the linear and nonlinear coefficients η_1 and η_3 for a surface with $\alpha = 0$ and at $T = 0.1T_c$. Similar to the bulk behavior, both coefficients are constant for all the distances from the surface.

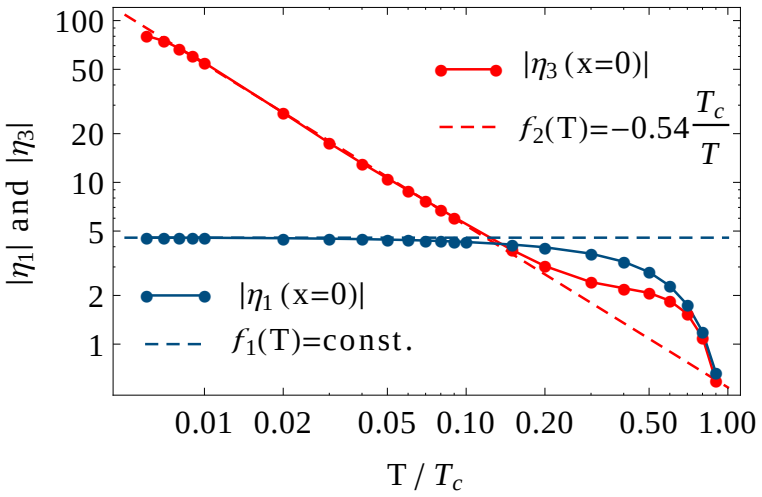

Figure 4.5: Double logarithmic plot of the temperature dependence of the linear (blue) and nonlinear (red) coefficients η_1 and η_3 at the surface. The plots are for the pairing orientation $\alpha = 0$ and at the surface. Due to the absence of the surface effects, the expected bulk results are achieved; η_1 shows a linear behavior while η_3 follows a $1/T$ law towards low temperatures. The blue and red dashed lines are the functions $f_1(T) = const.$ and $f_2(T) = -0.54T_c/T$ respectively.

4.2.2 At a nodal surface

Both the linear response coefficient η_1 as well as the nonlinear coefficient η_3 show a completely different behavior when the surface has a nodal direction, as is shown in figure 4.6.

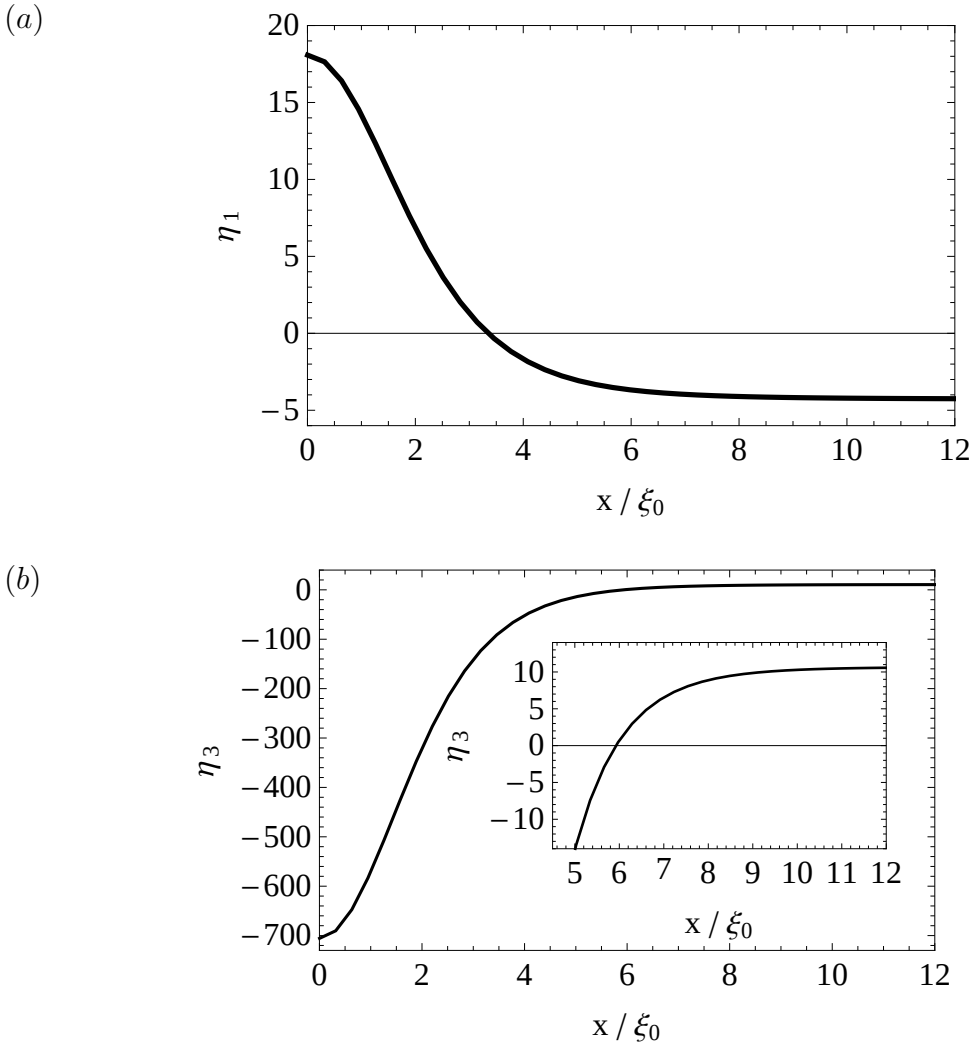

Figure 4.6: Spatial dependence of the linear and nonlinear coefficient η_1 (a) and η_3 (b) at $T = 0.1T_c$ and $\alpha = \pi/4$. Both have a bulk constant value which changes the sign when reaching surface within a few coherence lengths. The sign of the coefficients changes and they gradually reach a higher magnitude at the surface, the amount of which is extremely large for η_3. Inset in (b): larger scale for $x > 4\xi_0$, highlighting the sign change of η_3.

There, the spatial variation of both coefficients at temperature $T = 0.1T_c$ is plotted. Up to a distance of a few coherence lengths from the surface, the Andreev

bound states are present. One can see that both parameters have constant bulk values until they approach this region. At this point they change sign and gradually reach a higher magnitude at the surface, the amount of which is extremely large for η_3. The bulk value of η_3 is consistent with the low temperature value $\Delta_0/2T$ known from earlier work [30].

In the next step, we study the temperature dependence of both coefficients at the surface. The double logarithmic figure 4.7 shows the variation of the linear

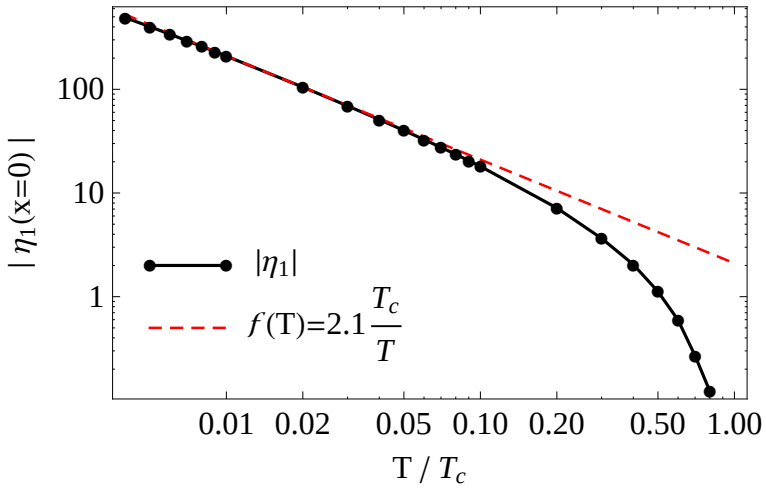

Figure 4.7: Double logarithmic plot of the modulus $|\eta_1|$ as a function of temperature. The dashed line is $f(T) = 2.1T_c/T$, implying a $1/T$ dependence of this coefficient at low temperatures.

response η_1 at the surface. The dashed line is a temperature dependence function $f(T) = 2.1T_c/T$. One can see that the linear coefficient follows a $1/T$ behavior in the low temperature regime, confirming previous results [33, 62].

The nonlinear response however, shows a completely different behavior. The detailed behavior is presented in figure 4.8. Right at the surface, the contribution of Andreev bound states results in a $1/T^3$ behavior (part (a) in figure 4.8). In the bulk however, it returns to the known results and follows a $1/T$ law (part (c) in figure 4.8). An intermediate position $x = 8\xi_0$ is also shown in figure 4.8(b), which demonstrates the transition from bulk to surface behavior. A dip in the logarithmic plot indicates that at a certain temperature η_3 changes sign; for higher temperatures, it follows a $1/T$ law and for lower temperatures a $1/T^3$ law. This result clearly shows that the nonlinear response is due to the surface area, where the Andreev bound states exist. It confirms also that the nonlinear response at the surface is much stronger than the nonlinear response in the bulk and with an opposite sign.

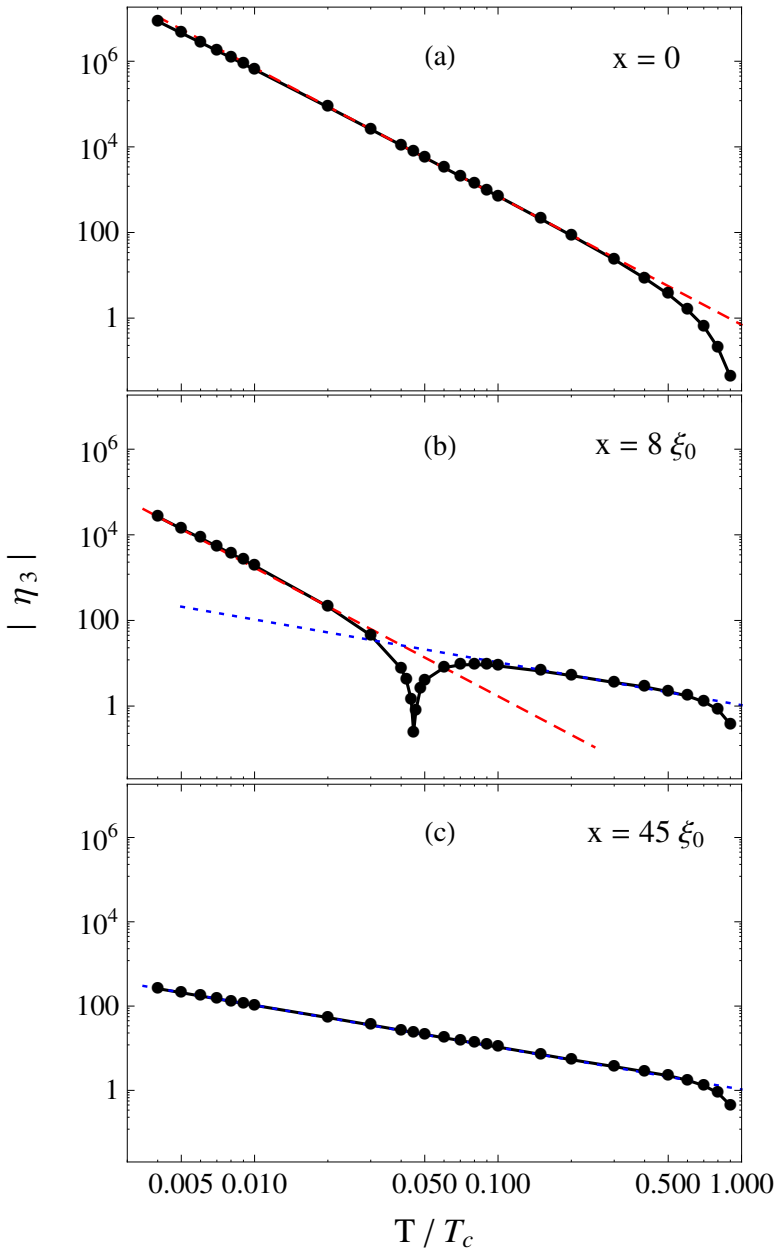

Figure 4.8: Double logarithmic plot of the modulus $|\eta_3|$ as a function of temperature T/T_c for three selected positions: (a) $x = 0$, (b) $x = 8\xi_0$, and (c) $x = 45\xi_0$. The nonlinear response in the bulk shows a $1/T$ behavior (the blue dotted line), it changes the sign (the dip in part (b)) and follows a $1/T^3$ behavior close to the surface (the red dashed line). This comparison shows that the nonlinear response is coming from the surface area, where the Andreev bound states are present. Furthermore, the nonlinear contribution at the surface has an opposite sign compared to the one in the bulk and is much stronger.

4.3 Intermodulation: total nonlinear response

In a typical intermodulation experiment only the total response of the system is probed. The quantity that is observed is the nonlinear change of the total inductance of the system. Therefore, it is useful to study the influence of the surface contribution to the intermodulation response.

In order to find the energy density in superconductors, we start from the Maxwell's equations:

$$\begin{aligned} \boldsymbol{E}\cdot\boldsymbol{\nabla}\times\boldsymbol{B}-\boldsymbol{B}\cdot\boldsymbol{\nabla}\times\boldsymbol{E} &= \frac{1}{2}\left(\mu_0\varepsilon_0\frac{\partial\boldsymbol{E}^2}{\partial t}+\frac{\partial\boldsymbol{B}^2}{\partial t}\right)+\mu_0\boldsymbol{J}\cdot\boldsymbol{E} \\ \boldsymbol{\nabla}\cdot(\boldsymbol{B}\times\boldsymbol{E}) &= \frac{\partial}{\partial t}\left(\frac{\varepsilon_0\mu_0}{2}\boldsymbol{E}^2+\frac{1}{2}\boldsymbol{B}^2\right)+\mu_0\boldsymbol{J}\cdot\boldsymbol{E}, \end{aligned}$$

which leads to

$$\boldsymbol{\nabla}\cdot\boldsymbol{S}+\frac{\partial}{\partial t}\left(\frac{\varepsilon_0}{2}\boldsymbol{E}^2+\frac{1}{2\mu_0}\boldsymbol{B}^2\right)=-\boldsymbol{J}\cdot\boldsymbol{E}., \tag{4.14}$$

Here, $\boldsymbol{S}$ is the Poynting vector, and $\boldsymbol{J}\cdot\boldsymbol{E}$ is the work which both electric and magnetic fields exert on the electric charges. The dissipative term on the right hand side of the equation (4.14) can be decomposed into two parts, using the first London equation: a dissipative term due to the normal current and a kinetic energy density due to the supercurrent:

$$\begin{aligned} \boldsymbol{J}\cdot\boldsymbol{E} &= \boldsymbol{J}_s\cdot\boldsymbol{E}+\boldsymbol{J}_n\cdot\boldsymbol{E} \\ &= \frac{\partial}{\partial t}\left(\frac{1}{2}\mu_0\lambda_L^2\boldsymbol{J}_s^2\right)+\boldsymbol{J}_n\cdot\boldsymbol{E}. \end{aligned}$$

The energy equation (4.14) is therefore given by the following form

$$\boldsymbol{\nabla}\cdot\boldsymbol{S}+\underbrace{\frac{\partial}{\partial t}\left(\frac{\varepsilon_0}{2}\boldsymbol{E}^2+\frac{1}{2\mu_0}\boldsymbol{B}^2+\frac{1}{2}\mu_0\lambda_L^2\boldsymbol{J}_s^2\right)}_{\partial_t u}=-\boldsymbol{J}_n\cdot\boldsymbol{E}. \tag{4.15}$$

In the absence of electric fields, the energy density in a superconductor is found from equation (4.15)

$$u=\frac{1}{2\mu_0}\boldsymbol{B}^2+\frac{1}{2}\mu_0\lambda_L^2\boldsymbol{J}_s^2=\frac{1}{2\mu_0}\left(\boldsymbol{B}^2-\mu_0\boldsymbol{J}_s\cdot\boldsymbol{A}\right). \tag{4.16}$$

In our calculations with a cylindrical Fermi surface, we assume translational invariance along both z and y directions. The calculated quantities therefore only depend

on x. From equation (4.16), the total inductance L can be calculated considering both the total kinetic and magnetic field energy per area in the system

$$\frac{1}{2}LI^2 = \int u\,dx = \frac{1}{2\mu_0}\int_0^\infty dx\left(B^2(x) - \mu_0 j(x)A(x)\right), \tag{4.17}$$

where $I = \int_0^\infty dx j(x)$ is the total current per unit length.

Using $B(x) = dA(x)/dx$ and $dB(x)/dx = -\mu_0 j(x)$, equation (4.17) can be brought by partial integration into a more convenient form as follows

$$\begin{aligned} L &= \frac{1}{I^2\mu_0}\left[\int_0^\infty dx\left(B^2(x) - \mu_0 j(x)A(x)\right)\right] \\ &= \frac{1}{I^2\mu_0}\left[\int_0^\infty dx\, B^2(x) + \int_0^\infty dx\,\frac{dB(x)}{dx}A(x)\right] \\ &= \frac{-B_{ext}A_0}{I^2\mu_0}, \end{aligned} \tag{4.18}$$

where $B_{ext} = B(x=0)$ and $A_0 = A(x=0)$.

Unlike the antinodal surfaces, the magnetic field dependence of the inductance shows a remarkable behavior in the presence of the Andreev bound states; at a special temperature, the curvature of the inductance in a nodal surface changes the sign. Figure 4.9 shows this behavior. For low temperatures the curvature is negative.

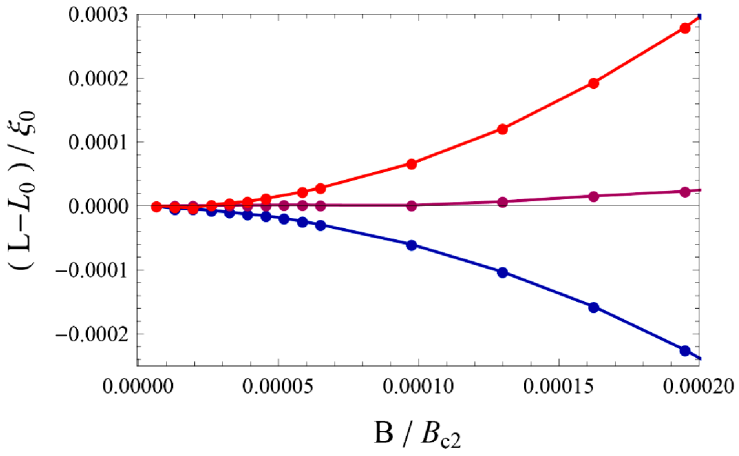

Figure 4.9: Curvature change of the Inductance L as a function of the external magnetic field for $T = 0.7T_c$ (red), $T = 0.3T_c$ (purple) and $T = 0.2T_c$ (blue). The calculations are done for the case of $\alpha = \frac{\pi}{4}$ and $\kappa = 63$. One can see that the curvature changes its sign at a temperature $T/T_c \approx 2.4/\sqrt{\kappa} \sim 0.3$. L_0 is the inductance for $B \to 0$.

With increasing temperature, the modulus of the curvature gradually reduces until a temperature is reached, at which it changes the sign and becomes positive. For

the given $\kappa = 63$, the sign change appears at a temperature of $T/T_c \sim 0.3$. The temperature at which the sign change happens, depends on the Ginzburg-Landau parameter κ and decreases by increasing κ. Later in chapter 5 we will show that this dependence is found to have the form $T/T_c \approx 2.4/\sqrt{\kappa}$.

Since the intermodulation response is proportional to the nonlinear coefficient $\frac{\partial^2 L}{\partial I^2}\ |_{I=0}$, it is necessary to study the Andreev bound states contribution to the second derivative of inductance. To do so, first we simplify equation (4.18) as follows. Integrating the Maxwell's equation $\boldsymbol{\nabla} \times \boldsymbol{B} = \mu_0 \boldsymbol{j}$ for $\boldsymbol{B} = B(x)\,\hat{e}_z$, and using the fact that the magnetic field vanishes in the bulk, results in $B_{ext} = \mu_0 I$. Substituting this relation into equation (4.18), one obtains

$$L = -\frac{A_0}{I}. \tag{4.19}$$

To lowest order in A_0 the total current I generally will be of the form

$$I = a_1 A_0 + a_3 A_0^3 + \mathcal{O}(A_0^5), \tag{4.20}$$

where a_1 and a_3 are determined from our numerical solutions of Eilenberger equations (see equation (4.13)). Thus, the total inductance can be written as

$$L = -\frac{A_0}{a_1 A_0 + a_3 A_0^3}.$$

As the next step, we differentiate L with respect to the total current I:

$$\frac{\partial L}{\partial I} = \frac{2a_3 A_0^3}{\left(a_1 A_0 + a_3 A_0^3\right)^2} \frac{\partial A_0}{\partial I}$$

and

$$\frac{\partial^2 L}{\partial I^2} = \frac{\left(\frac{\partial A_0}{\partial I}\right)^2 \left(2a_3 a_1 A_0^3 - 6a_3^2 A_0^5\right)}{\left(a_1 A_0 + a_3 A_0^3\right)^3} + \frac{\partial^2 A_0}{\partial I^2} \frac{2a_3 A_0^3}{\left(a_1 A_0 + a_3 A_0^3\right)^2}. \tag{4.21}$$

On the other hand, taking the derivative with respect to I on both sides of equation (4.20), one obtains

$$\frac{\partial A_0}{\partial I} = \frac{1}{a_1 + 3a_3 A_0^2} \tag{4.22}$$

and

$$\frac{\partial^2 A_0}{\partial I^2} = \frac{-6a_3 A_0}{\left(a_1 + 3a_3 A_0^2\right)^3}. \tag{4.23}$$

Substituting (4.22) and (4.23) in equation (4.21), we obtain

$$\frac{\partial^2 L}{\partial I^2} = \frac{2a_3 a_1^2 - 18a_3^3 A_0^4 - 12a_1 a_3^2 A_0^2 - 12a_3^3 A_0^4}{\left(a_1 + 3a_3 A_0^2\right)^3 \left(a_1 + a_3 A_0^2\right)^3}.$$

Finally at $I = 0$, i.e. $A_0 = 0$, one finds

$$\left.\frac{\partial^2 L}{\partial I^2}\right|_{I=0} = \frac{2a_3 a_1^2}{a_1^3 a_1^3} = \frac{2a_3}{a_1^4}. \tag{4.24}$$

Determining a_1 and a_3 from numerical solution of Eilenberger's equations, we determined the temperature dependence of the nonlinear coefficient $\left|\frac{\partial^2 L}{\partial I^2}\right|_{I=0}$ which is presented in figure 4.10 on a double logarithmic scale. Taking into account the

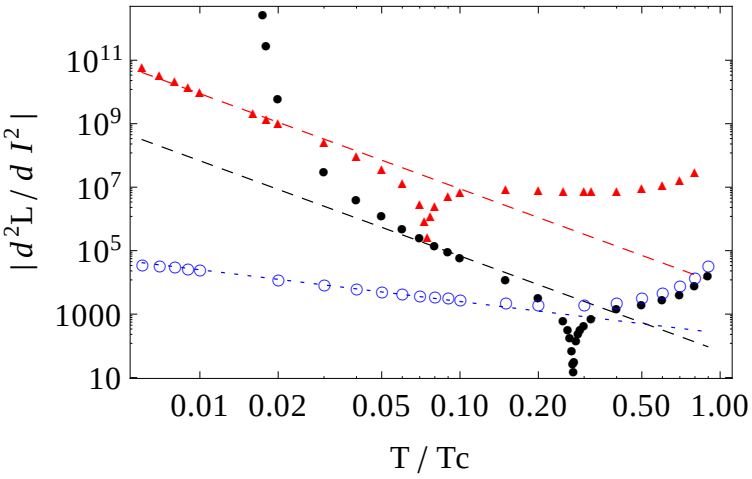

Figure 4.10: Double logarithmic plot of $\left|\frac{\partial^2 L}{\partial I^2}\right|_{I=0}$ as a function of temperature T/T_c for $\kappa = 63$ and $\alpha = \frac{\pi}{4}$ (solid black circles), for $\kappa = 1000$ and $\alpha = \frac{\pi}{4}$ (solid red triangles), and for $\kappa = 63$ and $\alpha = 0$ (open blue circles). The dashed lines show a $1/T^3$ behavior, and the dotted line a $1/T$ behavior. It is seen that the low temperature nonlinearity varies as $1/T^3$ for $\alpha = \pi/4$ and as $1/T$ for $\alpha = 0$. Increasing the value of κ leads to a wider range with $1/T^3$ dependence.

case of $\kappa = 63$ and $\alpha = \pi/4$ (the solid black circles), we can see that decreasing the temperature from T_c, leads to a reduction of the nonlinear coefficient until a temperature of about $T/T_c \approx 2.4/\sqrt{\kappa}$. There, it changes sign which is visible as a dip in the double logarithmic plot. Below this temperature, the nonlinear coefficient increases following a $1/T^3$ law. It diverges finally at temperatures around $T/T_c \approx 1/\kappa$, due to the break down of the local approximation. The temperature range between $T/T_c \approx 2.4/\sqrt{\kappa}$ and $T/T_c \approx 1/\kappa$ is readily available in intermodulation experiments. With a knowledge about this temperature range, observation of such a $1/T^3$ behavior may make them a tool to study the Andreev bound states.

Increasing the value of κ (for example $\kappa = 1000$ in figure 4.10, indicated by solid red triangles), results in a shift in both limiting temperatures to lower values. The general properties of the effect remain unchanged. However, the $1/T^3$ law dependency is obtained on a larger temperature range.

For comparison, the behavior of $\kappa = 63$ and $\alpha = 0$ is also shown (open blue circles). In absence of the bound states, there is no sign change in the nonlinear coefficient and it follows a $1/T$ law at low temperatures, as is known from the bulk results.

Chapter 5

An analytical solvable model

In order to check the validity of the numerical calculations discussed in chapter 4 and to obtain a physical understanding of the results, we made an analytical calculation of a solvable model, which we present in this chapter [63].

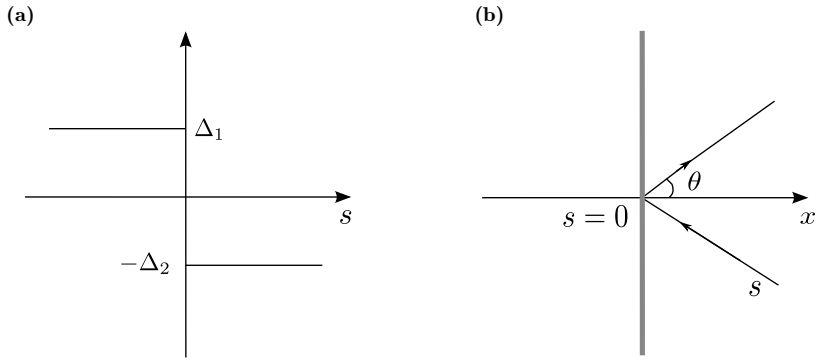

Figure 5.1: (a) The sketch of the spatially constant order parameter for one trajectory, with a sign change at the surface. (b) The trajectory path for a reflecting angle θ at $s = 0$ at the surface.

In this model, we have assumed a piecewise constant gap which changes sign at the surface, as is shown in figure 5.1(a). The quasiparticles run through the trajectory's path s, which originates at the reflecting point at the surface (figure 5.1(b)). Therefore,

$$\Delta = \begin{cases} -\Delta_2 & s > 0 \\ \Delta_1 & s \leq 0 \end{cases}, \tag{5.1}$$

where both Δ_1 and Δ_2 are positive quantities.

In the first section, we calculate at first the angle-resolved density of bound states. For a constant gap, Eilenberger equations can be solved analytically [46, 47]. In this way, the residue of the zero-energy pole of the Eilenberger propagator is determined analytically, which contains the contributions from the zero energy bound states

at the surface. The bound state contribution to the density of states is found as a spectral weight of a δ function. This spectral weight is used to determine the local density of states at the surface. Due to the importance of the nodal surfaces, we focus on the special case of $\alpha = \pi/4$ and continue with this orientation angle. The total bound state contribution obtained from the first section is used in the second section in order to find the bound state contribution on the current density, which in turn is used to calculate the linear and nonlinear responses. Finally the total inductance and the nonlinear response is calculated. The results are in good agreement with the numerical results presented in chapter 4.

5.1 Local density of bound states at the surface

5.1.1 Angle resolved density of bound states

In order to find the bound states, one needs to solve the Riccati equations. The initial values for the Riccati amplitudes $a(s)$ and $b(s)$ is given by

$$\begin{cases} b\,(s) = b_0 = \frac{-\Delta_2}{\varepsilon_n + \sqrt{\varepsilon_n^2 + \Delta_2^2}} & s > 0 \\ a\,(s) = a_0 = \frac{\Delta_1}{\varepsilon_n + \sqrt{\varepsilon_n^2 + \Delta_1^2}} & s \leq 0 \end{cases}. \tag{5.2}$$

The problem can be discussed for two different cases: $s > 0$ and $s < 0$.

The case of $s > 0$

For $s > 0$, the parameter b is given by $b(s) = b_0$. For a piecewise constant gap function, the Riccati equation (2.30) can be solved analytically [64], resulting in

$$a\,(s) = \frac{1}{-c_a + A\,e^{cs}} + a_{0,+}, \tag{5.3}$$

where

$$c_a = \frac{-\Delta_2}{2\sqrt{\varepsilon_n^2 + \Delta_2^2}} \quad \text{and} \quad c = \frac{2}{\hbar v_F}\sqrt{\varepsilon_n^2 + \Delta_2^2}. \tag{5.4}$$

$a_{0,+}$ is a known solution to the equation (5.3) which can be chosen to be the bulk value of the Parameter $a(s)$ for $s > 0$ [64], i.e.:

$$a_{0,+} = \frac{-\Delta_2}{\varepsilon_n + \sqrt{\varepsilon_n^2 + \Delta_2^2}} = b_0. \tag{5.5}$$

Using the boundary condition $a(s = 0) = a_0$ in equation (5.3), the coefficient A is found to be

$$A = \frac{1}{a_0 - b_0} + c_a. \tag{5.6}$$

The local density of states for the considered trajectory is given by the analytic continuation $\varepsilon_n \to -iE + \delta$ as

$$N(E,s) = \mathrm{Re}\frac{1 - a(s)\,b(s)}{1 + a(s)\,b(s)} = -1 + 2\mathrm{Re}\frac{1}{1 + a(s)\,b(s)}. \tag{5.7}$$

Considering the special case $E = 0$, one finds: $a_0|_{E=0} = 1$, $b_0|_{E=0} = -1$, $c_a|_{E=0} = -1/2$ and $A|_{E=0} = 0$. This set of parameters results in a singularity in the density of states at $E = 0$, since the term $1 + a(s)\,b(s)$ vanishes at this energy. To find the amplitude of this singularity we calculate the residue of the function $\frac{1}{1+a(s)b(s)}$ at the singularity point:

$$r = \lim_{E\to 0}\left(E \cdot \frac{1}{1 + a(s)\,b(s)}\right) = \frac{1}{\frac{\partial}{\partial E}\left[1 + a(s)\,b(s)\right]_{E=0}}. \tag{5.8}$$

Thus

$$\begin{aligned}
\frac{1}{r} &= \left[\frac{\partial b(s)}{\partial E} - \frac{\partial a(s)}{\partial E}\right]_{E=0} \\
&= \left[\frac{\partial b_0}{\partial E} - \frac{\partial}{\partial E}\left[\frac{1}{-c_a + Ae^{cs}}\right] - \frac{\partial b_0}{\partial E}\right] \\
&= 4\left[-\frac{\partial c_a}{\partial E} + \frac{\partial A}{\partial E}e^{cs}\right]_{E=0}.
\end{aligned} \tag{5.9}$$

On the other hand, taking the derivative of equation (5.6) results in

$$\left.\frac{\partial A}{\partial E}\right|_{E=0} = \left.\frac{\partial c_a}{\partial E}\right|_{E=0} - \frac{1}{4}\left.\frac{\partial\left(a_0 - b_0\right)}{\partial E}\right|_{E=0}. \tag{5.10}$$

Furthermore, the derivatives of the parameters a_0, b_0 and c_a with respect to E after analytic continuation in the limit of $\delta \to 0$, are given by

$$\left.\frac{\partial a_0}{\partial E}\right|_{E=0} = \frac{i}{\Delta_1}, \quad \left.\frac{\partial b_0}{\partial E}\right|_{E=0} = -\frac{i}{\Delta_2} \quad \text{and} \quad \left.\frac{\partial c_a}{\partial E}\right|_{E=0} = 0. \tag{5.11}$$

Inserting these relations into equation (5.10), results in

$$\left.\frac{\partial A}{\partial E}\right|_{E=0} = -\frac{1}{4}\left(\frac{i}{\Delta_1} + \frac{i}{\Delta_2}\right) = \frac{-i}{4}\frac{\Delta_1 + \Delta_2}{\Delta_1\Delta_2}. \tag{5.12}$$

The residue in equation (5.9) is then obtained from

$$r = i\frac{\Delta_1\Delta_2}{\Delta_1 + \Delta_2}e^{-c_0 s}, \tag{5.13}$$

where

$$c_0 = c\,(E=0) = \frac{2\Delta_2}{\hbar v_F}. \tag{5.14}$$

Around $E = 0$, one can make the approximation discussed below:

$$\mathrm{Re}\ \frac{1}{1+a\,(s)\,b\,(s)} \simeq \mathrm{Re}\ \frac{r}{E+i\delta} = \frac{E}{E^2+\delta^2}\mathrm{Re}\ r + \frac{\delta}{E^2+\delta^2}\mathrm{Im}\ r, \tag{5.15}$$

what in the limit of $\delta \to 0$ will have the form

$$\mathrm{Re}\ \frac{1}{1+a\,(s)\,b\,(s)} \simeq \frac{\mathrm{Re}\ r}{E} + \pi\delta\,(E)\,\mathrm{Im}\ r. \tag{5.16}$$

Thus, equation (5.7) leads to

$$N\,(r) \simeq -1 + \frac{2\mathrm{Re}\ r}{E} + \underbrace{2\pi\mathrm{Im}\ r\,(s)\,\delta\,(E)}_{\text{bound state part}}. \tag{5.17}$$

Since the residue given in equation (5.13) is purely imaginary, the bound states contribution to the density of states at zero energy is obtained from

$$N_{\mathrm{bs}}\,(E,s) = 2\pi\mathrm{Im}\ r\,(s)\,\delta\,(E) = 2\pi\frac{\Delta_1\Delta_2}{\Delta_1+\Delta_2}e^{-c_0 s}\delta\,(E) \qquad \text{for } s>0. \tag{5.18}$$

The case of $s < 0$

Now we look at the case in which $s < 0$. Similar to the case $s > 0$, one finds

$$a\,(s) = \frac{\Delta_1}{\varepsilon_n + \sqrt{\varepsilon_n^2+\Delta_1^2}} = a_0, \tag{5.19}$$

$$b\,(s) = \frac{1}{-c_b + Be^{-\tilde{c}s}} + b_{0,-}, \tag{5.20}$$

where

$$c_b = \frac{\Delta_1}{2\sqrt{\varepsilon_n^2+\Delta_1^2}} \quad \text{and} \quad \tilde{c} = \frac{2}{\hbar v_F}\sqrt{\varepsilon_n^2+\Delta_1^2}. \tag{5.21}$$

$b_{0,-}$ is also a known solution to the equation (5.20) which is chosen to be the bulk value of the Parameter $b(s)$ for $s < 0$, i.e.

$$b_{0,-} = \frac{\Delta_1}{\varepsilon_n + \sqrt{\varepsilon_n^2+\Delta_1^2}} = a_0. \tag{5.22}$$

The initial condition $b\,(s=0) = b_0$ leads to

$$B = \frac{1}{b_0 - a_0} + c_b. \tag{5.23}$$

This parameter vanishes when $\varepsilon_n = 0$, since $a_0 = 1$, $b_0 = -1$, $c_b = \frac{1}{2}$.

In order to find the bound states contribution, analogous to $s > 0$, we need to calculate the residue of the function $\frac{1}{1+a(s)b(s)}$ at the singularity point $E = 0$

$$\begin{aligned}\frac{1}{r} &= \frac{\partial}{\partial E}\left[1 + a\left(s\right) b\left(s\right)\right]_{E=0} \\ &= \frac{\partial}{\partial E}\left[\frac{1}{-c_b + Be^{-\tilde{c}s}}\right]_{E=0} \\ &= -4\frac{\partial}{\partial E}\left[-c_b + Be^{-\tilde{c}s}\right]_{E=0} \\ &= -i\frac{\Delta_1 + \Delta_2}{\Delta_1 \Delta_2} e^{-\tilde{c}_0 s}, \end{aligned} \tag{5.24}$$

where

$$\tilde{c}_0 = \tilde{c}\left(E = 0\right) = \frac{2\left|\Delta_1\right|}{\hbar v_F}. \tag{5.25}$$

This results in a pure imaginary term for the residue

$$r = i\frac{\Delta_1 \Delta_2}{\Delta_1 + \Delta_2} e^{\tilde{c}_0 s}. \tag{5.26}$$

Therefore, the contribution to the density of states is given by

$$N_{\text{bs}}\left(E, s\right) = 2\pi \text{Im}\; r\left(s\right) \delta\left(E\right) = 2\pi \frac{\Delta_1 \Delta_2}{\Delta_1 + \Delta_2} e^{\tilde{c}_0 s} \delta\left(E\right) \qquad \text{for } s < 0. \tag{5.27}$$

5.1.2 Total density of bound states

The next step is to consider all trajectory directions. In this case, both Δ_1 and Δ_2 depend on the trajectory orientation. Trajectories are divided into two groups, depending on their orientation relative to the surface normal, θ:

For $\theta \in \left[-\frac{\pi}{2}, \frac{\pi}{2}\right]$,

$$\Delta_1 = \Delta_0 \cos\left(2\left(\pi - \theta - \alpha\right)\right) = \Delta_0 \cos\left(2\left(\theta + \alpha\right)\right) \tag{5.28}$$

$$-\Delta_2 = \Delta_0 \cos\left(2\left(\theta - \alpha\right)\right) \quad \Rightarrow \Delta_2 = -\Delta_0 \cos\left(2\left(\theta - \alpha\right)\right). \tag{5.29}$$

The density of bound states in this case is obtained from equation (5.18), using $s = \frac{x}{\cos\theta} > 0$ and $c_0 = \frac{2\Delta_2}{\hbar v_F} = -\frac{2\Delta_0}{\hbar v_F} \cos\left(2\left(\theta - \alpha\right)\right)$:

$$2\pi \frac{\Delta_1 \Delta_2}{\Delta_1 + \Delta_2} e^{-c_0 s} = \frac{\pi}{2} \Delta_0 \frac{\cos 4\alpha + \cos 4\theta}{\sin 2\theta \sin 2\alpha} e^{\frac{2\Delta_0}{\hbar v_F} \cos(2(\theta-\alpha)) \frac{x}{\cos\theta}} \tag{5.30}$$

On the other hand, this relation should fulfill the initial conditions $\Delta_1 > 0$, $\Delta_2 > 0$, $\theta \in \left[-\frac{\pi}{2}, \frac{\pi}{2}\right]$ and $\alpha \in \left[0, \frac{\pi}{4}\right]$. Therefore, one obtains

$$\Delta_1 > 0 \Rightarrow \cos\left(2\left(\theta+\alpha\right)\right) > 0, \tag{5.31}$$

$$\begin{aligned} \Delta_2 > 0 \quad &\Rightarrow \quad \cos\left(2\left(\theta-\alpha\right)\right) < 0 \\ &\Rightarrow \quad \cos\left(2\left(\theta-\alpha\right)\right) = -\left|\cos\left(2\left(\theta-\alpha\right)\right)\right|, \end{aligned} \tag{5.32}$$

$$\begin{aligned} \theta \in \left[-\frac{\pi}{2}, \frac{\pi}{2}\right] \quad &\Rightarrow \quad \cos\,\theta > 0 \\ &\Rightarrow \quad \cos\,\theta = \left|\cos\,\theta\right|, \end{aligned} \tag{5.33}$$

$$\begin{aligned} \Delta_1\Delta_2 > 0 \quad &\Rightarrow \quad \cos\left(2\left(\theta+\alpha\right)\right)\,\cos\left(2\left(\theta-\alpha\right)\right) < 0 \\ &\Rightarrow \quad \cos\,4\theta < -\cos\,4\alpha, \end{aligned} \tag{5.34}$$

$$\alpha \in \left[0, \frac{\pi}{4}\right] \quad \Rightarrow \quad \sin\,2\alpha > 0, \tag{5.35}$$

$$\begin{aligned} \Delta_1 + \Delta_2 > 0 \quad &\Rightarrow \quad -2\sin\,2\theta \sin\,2\alpha > 0 \\ &\Rightarrow \quad \sin\,2\theta < 0 \\ &\Rightarrow \quad \sin\,2\theta = -\left|\sin\,2\theta\right|. \end{aligned} \tag{5.36}$$

Taking all these conditions into account, the density of bound states will be given by

$$N_{\mathrm{bs}}\left(E,x,\theta\right) = \delta\left(E\right)\begin{cases} -\frac{\pi}{2}\Delta_0 \frac{\cos\,4\alpha+\cos\,4\theta}{\left|\sin\,2\theta\right|\sin\,2\alpha} e^{\frac{-2\Delta_0}{\hbar v_F}\left|\cos(2(\theta-\alpha))\right|\frac{x}{\left|\cos\,\theta\right|}} & \text{for } \cos\,4\theta < -\cos\,4\alpha \\ 0 & \text{elsewhere} \end{cases} \tag{5.37}$$

Using the same procedure for $\theta \in \left[\frac{\pi}{2}, \frac{3\pi}{2}\right]$, and taking into account that in this case, $s = \frac{x}{\cos\,\theta} = -\frac{x}{\left|cos\theta\right|} < 0$ and $\tilde{c}_0 = \frac{2\left|\Delta_1\right|}{\hbar v_F} = \frac{2\Delta_0}{\hbar v_F}\left|\cos\left(2\left(\theta-\alpha\right)\right)\right|$, one obtains the same result as in equation (5.37).

5.1.3 Density of bound states for a special case of $\alpha = \frac{\pi}{4}$

As is discussed in the previous chapters, the maximum contribution to the bound states is obtained at the nodal surfaces, where all the trajectories experience a change in the phase of the order parameter. Therefore, the pairing orientation $\alpha = \frac{\pi}{4}$ is of interest. At this pairing orientation, the angle resolved density of states (5.37) will have the following form

$$\begin{aligned} N_{\mathrm{bs}}\left(E,x,\theta\right) &= \pi\Delta_0\left|\sin\,2\theta\right| e^{\frac{-4\Delta_0}{\hbar v_F}\left|\sin\,\theta\right| x}\delta\left(E\right) \\ &= \pi\Delta_0\left|\sin\,2\theta\right| e^{-(4/\pi)\left|\sin\,\theta\right|(x/\xi_0)}\delta\left(E\right). \end{aligned} \tag{5.38}$$

The local density of states is obtained by integrating over all the possible trajectory directions

$$\begin{aligned} N_{\mathrm{bs}}(E,x) &= \frac{2}{\pi}\int_0^{\pi/2} \mathrm{d}\theta\, N_{\mathrm{bs}}(E,x,\theta) \\ &= 4\Delta_0 \int_0^{\pi/2} \mathrm{d}\theta \sin\theta \cos\theta\, e^{-(4/\pi)|\sin\theta|(x/\xi_0)} \delta(E). \end{aligned} \tag{5.39}$$

The δ function shows that the bound states are only present at zero energy. The exponential factor drops off on the length scale of the coherence length, showing that these states are localized at the surface. Changing the variables by $u = \sin\theta$ and defining the parameter $\gamma = \frac{-4x}{\pi\xi_0}$, one finds

$$\begin{aligned} N_{\mathrm{bs}}(E,x) &= 4\Delta_0 \int_0^1 \mathrm{d}u\, u\, e^{\gamma u}\delta(E) = 4\Delta_0\delta(E)\frac{e^{\gamma}(\gamma-1)+1}{\gamma^2} \\ &\simeq 4\Delta_0\delta(E)\left(\frac{1}{2}+\frac{\gamma}{3}+\frac{\gamma^2}{8}+O\left(\gamma^3\right)\right). \end{aligned} \tag{5.40}$$

5.2 Bound states contribution to the current density

Substituting equation (5.39) in equation (4.3), one can find the contribution of the bound states to the current density

$$\begin{aligned} j_{\mathrm{bs}}(x) &= \frac{1}{\pi} e N_0 v_F \int_{-\infty}^{\infty} \mathrm{d}E \int_0^{\pi} \mathrm{d}\theta \sin\theta \cdot f(E) \\ &\quad \times \left[N_{\mathrm{bs}}(E + \frac{e}{c} v_F A(x) \sin\theta, x, \theta) - N_{\mathrm{bs}}(E - \frac{e}{c} v_F A(x) \sin\theta, x, \theta) \right] \\ &= 4eN_0 v_F \Delta_0 \int_0^{\pi/2} \mathrm{d}\theta \sin^2\theta \cos\theta\, e^{-(4/\pi)|\sin\theta|(x/\xi_0)} \\ &\quad \times \left[f(-\frac{e}{c} v_F A(x) \sin\theta) - f(\frac{e}{c} v_F A(x) \sin\theta) \right]. \end{aligned} \tag{5.41}$$

It is to be mentioned that the calculation above is for the nodal direction $\alpha = \frac{\pi}{4}$.

5.2.1 Linear response at the surface

In order to find the linear response, one needs to find the first derivative of the current density with respect to the vector potential in the limit of $\gamma \to 0$. It results in

$$\begin{aligned} \left[\frac{\partial j_{\mathrm{bs}}(x)}{\partial A(x)}\right]_{A(x)=0,\gamma\to 0} &= \lim_{\gamma\to 0}\left[\frac{-2}{\mu_0\lambda_L^2}\frac{\Delta_0}{T}\frac{1}{\gamma^4}\left[6 - e^{-\gamma}\left(6+6\gamma+3\gamma^2+\gamma^3\right)\right]\right] \\ &= \frac{-1}{\mu_0\lambda_L^2}\frac{\Delta_0}{2T}, \end{aligned} \tag{5.42}$$

where λ_L is the London penetration depth and is given by $\frac{1}{\lambda_L^2} = \mu_0 \frac{e^2}{c} N_0 v_F^2$. Similar to the numerical results presented in chapter 4, the linear response at the surface follows a $1/T$ law.

5.2.2 Nonlinear response at the surface

To find the nonlinear response, we need to calculate $\left[\frac{\partial^3 j_{\rm bs}(x)}{\partial A^3(x)}\right]_{A(x)=0}$. Using equation (5.41), the nonlinear response can be obtained from

$$\begin{aligned}
&\left[\frac{\partial^3 j_{\rm bs}(x)}{\partial A^3(x)}\right]_{A(x)=0} \\
&= 4eN_0 v_F \Delta_0 \int_0^{\pi/2} {\rm d}\theta \sin^2\theta \cos\,\theta e^{-(4/\pi)|\sin\theta|(x/\xi_0)} \frac{\partial^3}{\partial A^3}\left[f\left(-\frac{e}{c}v_F A\right) - f\left(\frac{e}{c}v_F A\right)\right]_{A=0} \\
&= -\frac{1}{T^3}\frac{e^4 v_F^4}{c^3} N_0 \Delta_0 \int_0^1 du\, u^5 e^{-\gamma u}. \quad (5.43)
\end{aligned}$$

At the surface,i.e. for $\gamma \to 0$, the nonlinear contribution is given by

$$\left[\frac{\partial^3 j_{\rm bs}(x)}{\partial A^3(x)}\right]_{A(x)=0,\gamma\to 0} = -\frac{1}{6}\frac{e^4 v_F^4}{c^3} N_0 \Delta_0 \frac{1}{T^3}, \quad (5.44)$$

which shows the $1/T^3$ behavior of the nonlinearity, consistent with our numerical calculations.

5.3 Nonlinear inductance

In order to find the inductance given by equation (4.24), we need to determine the coefficients a_1 and a_3. To do so, we should integrate the current density equation (4.13), using the following approximations.

For $\kappa = \lambda_L/\xi_0 \gg 1$ we can assume that the vector potential varies exponentially on the length scale of the penetration length λ_L. Thus it is possible to make the ansatz

$$A(x) = \underbrace{A_0(x)}_{\mathcal{O}(B_{ext})} + \underbrace{\epsilon(x)}_{\mathcal{O}(B_{ext}^3)}, \quad (5.45)$$

where

$$A_0(x) = A_0 e^{-x/\lambda_L} \quad (5.46)$$

is the linear term and

$$\epsilon(x) = \epsilon_1 e^{-x/\lambda_L} + \epsilon_3 e^{-3x/\lambda_L} \quad (5.47)$$

is a correction due to the nonlinear term. The boundary conditions are given by $dA_0(x)/dx|_{x=0} = B_{ext}$, $\lim_{x\to\infty} A_0(x) = 0$, $d\epsilon(x)/dx|_{x=0} = 0$ and $\lim_{x\to\infty}\epsilon(x) = 0$.

Furthermore, the functions $\eta_1(x)$ and $\eta_3(x)$ both vary on the length scale of the coherence length ξ_0, which is much smaller than λ_L. Therefore, we can approximate them as

$$\eta_1(x) = c_1\delta(x) + \eta_{1b} \tag{5.48}$$
$$\eta_3(x) = c_3\delta(x) + \eta_{3b}. \tag{5.49}$$

Here, η_{1b} and η_{3b} are the bulk values of $\eta_1(x)$ and $\eta_3(x)$, respectively. The coefficients c_1 and c_3 describe the contributions of the surface bound states. They are obtained by substituting equation (5.38) into equations (4.11) and (4.12) and integrating over x from 0 to ∞. This yields

$$c_1 = -\frac{\pi\Delta_0}{6T}\xi_0 \tag{5.50}$$
$$c_3 = -\frac{\pi\Delta_0^3}{20T^3}\xi_0. \tag{5.51}$$

The next step is to find the coefficients ϵ_1 and ϵ_3. Inserting the ansatz (5.45) into the equation (4.13), together with the Maxwell's equation $\partial^2 A(x)/\partial x^2 = \mu_0 j(x)$, we obtain

$$\frac{\partial^2 A_0(x)}{\partial x^2} + \frac{\partial^2 \epsilon(x)}{\partial x^2} = \\ -2\mu_0 e^2 v_F^2 N_0 \eta_1(x)\left(A_0(x)+\epsilon(x)\right) + \frac{2\mu_0 e^4 v_F^4 N_0}{\Delta_0^2}\eta_3(x)\left(A_0(x)+\epsilon(x)\right)^3. \tag{5.52}$$

Using equation (5.46), together with

$$\left[A_0(x)+\epsilon(x)\right]^3 = \underbrace{A_0^3(x)}_{\mathcal{O}(B_{ext}^3)} + \underbrace{3A_0^2(x)\,\epsilon(x)}_{\mathcal{O}(B_{ext}^5)} + \underbrace{3A_0(x)\,\epsilon^2(x)}_{\mathcal{O}(B_{ext}^7)} + \underbrace{\epsilon^3(x)}_{\mathcal{O}(B_{ext}^9)} \simeq A_0^3(x), \tag{5.53}$$

results in the following equation for $\epsilon(x)$:

$$\left[\frac{\partial^2}{\partial x^2} + 2\mu_0 e^2 v_F^2 N_0 \eta_1(x)\right]\epsilon(x) = \frac{2\mu_0 e^4 v_F^4 N_0}{\Delta_0^2}\eta_3(x) A_0^3(x). \tag{5.54}$$

We discuss this equation for two different boundary conditions: in the presence of the surface nonlinearity $x = 0$ and for the bulk linear case $x > 0$.

- For $x > 0$, only the bulk contribution to the $\eta_1(x)$ and $\eta_3(x)$ is present. Therefore, the equation (5.54) is given by

$$\left[\frac{\partial^2}{\partial x^2} + 2\mu_0 e^2 v_F^2 N_0 \eta_{1b}\right]\epsilon(x) = \frac{2\mu_0 e^4 v_F^4 N_0}{\Delta_0^2}\eta_{3b} A_0^3 e^{-3x/\lambda_L}. \tag{5.55}$$

On the other hand, substituting the ansatz (5.47) into equation (5.54), leads to

$$\left[\frac{\partial^2}{\partial x^2}+2\mu_0 e^2 v_F^2 N_0 \eta_{1b}\right]\epsilon\left(x\right) = \left(2\epsilon_1\mu_0 e^2 v_F^2 N_0\eta_{1b}+\frac{\epsilon_1}{\lambda_L^2}\right)e^{-x/\lambda_L}+\left(2\epsilon_3\mu_0 e^2 v_F^2 N_0\eta_{1b}+\frac{9\epsilon_3}{\lambda_L^2}\right)e^{-3x/\lambda_L}. \tag{5.56}$$

Comparing with equation (5.55), the coefficient ϵ_3 can be determined as

$$\epsilon_3 = -\frac{1}{8}\frac{e^2 v_F^2 \eta_{3b}}{\Delta_0^2\eta_{1b}}A_0^3. \tag{5.57}$$

- For the case of $x=0$, the jump condition yields to

$$\int_{0^-}^{0^+}\mathrm{d}x\frac{\mathrm{d}^2\epsilon}{\mathrm{d}x^2}=\frac{\mathrm{d}\epsilon\left(0^+\right)}{\mathrm{d}x}-\frac{\mathrm{d}\epsilon\left(0^-\right)}{\mathrm{d}x}=\frac{\mathrm{d}\epsilon\left(0^+\right)}{\mathrm{d}x}. \tag{5.58}$$

The left hand side is obtained from integrating the equation (5.54)

$$\begin{aligned}\int_{0^-}^{0^+}\mathrm{d}x\frac{\mathrm{d}^2\epsilon}{\mathrm{d}x^2} &= -\int_{0^-}^{0^+}\mathrm{d}x\,2\mu_0 e^2 v_F^2 N_0\left(c_1\delta(x)+\eta_{1b}\right)\epsilon\left(x\right)\\ &\quad+\int_{0^-}^{0^+}\mathrm{d}x\,\frac{2\mu_0 e^4 v_F^4 N_0}{\Delta_0^2}\left(c_3\delta(x)+\eta_{3b}\right)A_0^3 e^{-3x/\lambda_L}\\ &= -2\mu_0 e^2 v_F^2 N_0 c_1\epsilon\left(0\right)+\frac{2\mu_0 e^4 v_F^4 N_0}{\Delta_0^2}c_3 A_0^3\\ &= -2\mu_0 e^2 v_F^2 N_0 c_1\left(\epsilon_1+\epsilon_3\right)+\frac{2\mu_0 e^4 v_F^4 N_0}{\Delta_0^2}c_3 A_0^3.\end{aligned} \tag{5.59}$$

The right hand side is simply found from equation (5.47)

$$\frac{\mathrm{d}\epsilon(0^+)}{\mathrm{d}x}=-\frac{\epsilon_1}{\lambda_L}-\frac{3\epsilon_3}{\lambda_L}. \tag{5.60}$$

Using equations (5.59) and (5.60), together with the equation (5.57), the coefficient ϵ_1 can be determined as

$$\begin{aligned}\epsilon_1 = &\frac{1}{-2\mu_0 e^2 v_F^2 N_0 c_1+\frac{1}{\lambda_L}}\\ &\times\left[\left(2\mu_0 e^2 v_F^2 N_0 c_1-\frac{3}{\lambda_L}\right)\left(-\frac{1}{8}\frac{e^2 v_F^2\eta_{3b}}{\Delta_0^2\eta_{1b}}A_0^3\right)-\frac{2\mu_0 e^4 v_F^4 N_0}{\Delta_0^2}c_3 A_0^3\right].\end{aligned} \tag{5.61}$$

Finally, integrating equation (4.13) over x from 0 to ∞ and comparing with $I = a_1 A_0 + a_3 A_0^3$, we find

$$a_1 = -2e^2 v_F^2 N_0 \left(c_1 + \lambda \eta_{1b}\right) \tag{5.62}$$

$$a_3 = \frac{2e^4 v_F^4 N_0}{\Delta_0^2} \left(c_3 + \frac{\lambda}{4}\eta_{3b}\right). \tag{5.63}$$

Using the low temperature limiting expressions $\eta_{1b} \sim 1$ and $\eta_{3b} \sim \Delta_0/2T$ finally the nonlinear coefficient to the inductance, equation (4.24), leads to

$$\left.\frac{\partial^2 L}{\partial I^2}\right|_{I=0} = \frac{2a_3}{a_1^4} = \frac{1}{16e^4 v_F^4 N_0^3 \Delta_0^2 \lambda_L^3} \frac{\frac{1}{2}\frac{\Delta_0}{T} - \frac{\pi}{5}\frac{1}{\kappa}\frac{\Delta_0^3}{T^3}}{\left(1 - \frac{\pi}{6}\frac{1}{\kappa}\frac{\Delta_0}{T}\right)^4}. \tag{5.64}$$

The nonlinear behavior obtained in chapter 4 can be well interpreted from equation (5.64). It shows that for high temperatures near T_c, the total nonlinear response of the system follows a $1/T$ increase (first term in the numerator). This is due to the bulk nonlinearities. At a temperature of the order of $T/T_c \sim 2.4/\sqrt{\kappa}$ the nonlinearities of the surface states become comparable with the bulk contributions and cancel them (second term in the numerator). Below that temperature the $1/T^3$ increase with the opposite sign dominates due to the surface states. Finally, at a temperature of the order of $T/T_c \sim 1/\kappa$ the nonlinear response diverges (denominator).

Figure 5.2 compares equation (5.64) with the numerical results obtained in chapter 4. Despite the approximations made, the results are in quite good agreement with the numerical results at low temperatures.

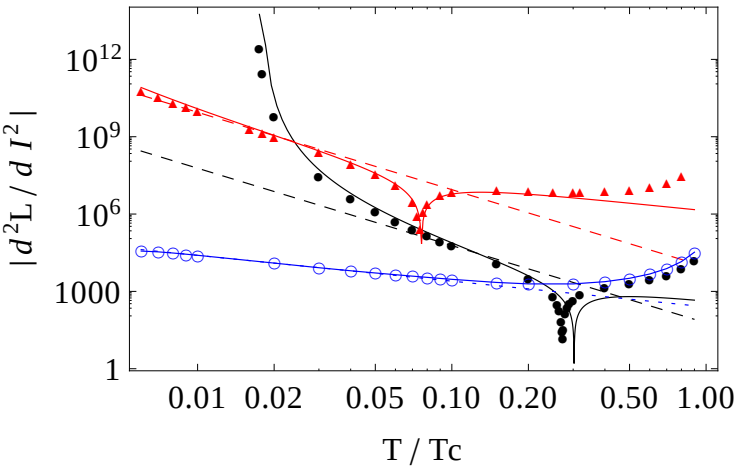

Figure 5.2: Double logarithmic plot of $\left|\frac{\partial^2 L}{\partial I^2}\right|_{I=0}$ as a function of temperature T/T_c for $\kappa = 63$ and $\alpha = \frac{\pi}{4}$ (solid black circles), for $\kappa = 1000$ and $\alpha = \frac{\pi}{4}$ (solid red squares), and for $\kappa = 63$ and $\alpha = 0$ (open blue circles). The dashed lines show a $1/T^3$ behavior, and the dotted line a $1/T$ behavior. The solid lines show the approximation. A fairly good agreement is achieved for low temperatures.

Chapter 6

Summary

In this work the surface of d-wave superconductors is studied. In the superconductors with nodes in the gap function, zero-energy Andreev bound states may appear at the surface depending on the orientation of the d-wave with respect to the surface normal. Existence of these states influences the properties of the superconductor on the length scale of the coherence length ξ_0, the spatial extension of the bound states. Surface roughness, surface disorder, or diffuse scattering as well as the external magnetic field at the surface may affect the bound states and consequently the surface properties; impurity scattering in the bulk of the superconductor is known to broaden the Andreev bound states [21, 22], while the screening current in the presence of an external magnetic field leads to a splitting of these states [23–25]. For this reason, we discuss the problem in three different cases: in the presence of impurities, in the presence of an external magnetic field, and a combination of these two cases. Based on Eilenberger equations, our self-consistent calculations are summarized as follows.

The superconductor in the presence of impurity scattering

In the high-T_c cuprate compounds it is believed that scatterers within the CuO_2 planes act as unitary scatterers, while the scatterers sitting between the CuO_2 planes are poorly screened and act as Born scatterers [51, 53, 54]. On the other hand, it has been shown previously that impurity scattering in the Born limit is much more effective in broadening the Andreev bound states than impurity scattering in the unitarity limit [21, 22]. Therefore, in this work we focus on the influence of bulk impurity scattering in the self-consistent Born approximation.

Confirming the reduction of bulk gap amplitude by increasing the impurity concentration, in section 3.4 we observe that superconducting behavior is destroyed already when the mean free path becomes comparable to the coherence length. This implies that there exists no dirty limit for d-wave superconductors. We show that the impurity scattering around zero energy is significantly increased near the surface as compared to the bulk due to the presence of Andreev bound states. This

leads to a larger broadening of the Andreev bound states than expected from the scattering rate in the bulk and consequently a decrease of the peak height of the local density of states at zero energy $N(E = 0)$. We show that the scaling behavior of the peak height is $\sim \sqrt{\ell}$ instead of the $\sim \ell$ behavior one would have expected from bulk scattering.

In an isotropic s-wave superconductor Anderson's theorem asserts that the renormalization of the pairing potential due to the anomalous self-energy Σ^Fexactly compensates the renormalization due to the normal self-energy Σ^G, such that the density of states and T_c remain unaffected by impurity scattering. However, this does not necessarily hold anymore in an anisotropic superconductor [58]. In the bulk of a d-wave superconductor the anomalous self-energy Σ^F is known to vanish. We find here that this is not generally the case near to a surface because of broken translational symmetry. We show that a nonzero renormalization of the pairing potential appears near the surface unless the orientation of the surface is highly symmetric with respect to the orientation of the d-wave.

Electromagnetic responses in a clean superconductor

Confirming the anomalous Meissner current at the nodal surface which was predicted before [23, 26], we show in subsection 3.5.1 that it persists throughout the full temperature range between $0.01T_c$ and $0.9T_c$. With the anomalous Meissner current flowing, the magnetic field initially increases before the normal Meissner screening sets in and eventually screens out the magnetic field exponentially. The field increase is stronger at low temperatures and leads to an increase in the modulus of the vector potential towards low temperatures. On the other hand due to the divergence of the penetration depth near T_c and due to the fact that the vector potential is the integral of the magnetic field, one expects an increasing vector potential with increasing penetration depth. The result is a nonmonotonous temperature dependence of the vector potential at the surface (figure 3.17). Since the vector potential is proportional to the superfluid velocity, the size of the peak splitting in the local density of states predicted in reference [23] is directly influenced by the nonmonotonous behavior of the vector potential. We observe that the splitting is large both for low temperatures and close to T_c. As a result also the peak height has a nonmonotonous temperature dependence. The observation of such an increase of the peak splitting toward low temperatures could be an experimental signature of the anomalous Meissner currents. It should be pointed out, however, that this effect becomes less pronounced the larger the κ value of the material.

The presence of the surface Andreev bound states also has a significant influence on the nonlinear Meissner effect. The nonlinear response coefficient in the bulk of a d-wave superconductor is known to show an upturn at low temperatures following a $1/T$ law in a clean system down to temperatures of the order of $1/\kappa$ [29, 31, 32, 61]. However, we can observe in figure 3.18 that the linear response properties are modified in the presence of Andreev bound states. We show in chapter 4 that

the contribution of the surface Andreev bound states to the nonlinear response coefficient follows a $1/T^3$ law, which will ultimately dominate the bulk $1/T$ behavior at sufficiently low temperatures. Our calculations in this part are done in the local approximation limit, which is normally justified when $\lambda_L \gg \xi_0$.

Considering the total inductance L, a quantity which actually is probed in typical intermodulation experiments, we show that the crossover from bulk dominated behavior to surface dominated behavior occurs at a comparatively high temperature of $T/T_c \sim 2.4/\sqrt{\kappa}$. Also at this point the nonlinear coefficient changes the sign. Such temperatures are readily available in intermodulation experiments and make them a tool to study surface Andreev bound states. The fingerprint of the Andreev bound state should be a $1/T^3$ temperature dependence and a sign change (180° relative phase change) in the nonlinear part of the inductance.

In order to check the validity of the numerical calculations and obtain a physical understanding of the results, in chapter 5 we present a model to solve the problem analytically. For low temperatures, the results are in good agreement with the numerical results.

Influence of the impurity scattering on the electromagnetic responses

Considering the Born impurity scattering in the presence of an external magnetic field, we show in subsection 3.5.2 that the peak height in the local density of states at the surface is strongly reduced due to the scattering rate. The peak width also grows with decreasing mean free path. However, the size of the peak splitting remains almost unaffected. It results from the fact that due to the peak splitting the available phase space for scattering processes is strongly reduced at low energies. This in turn means that the quasiparticle scattering rate at small energies remains small even when the mean-free path becomes small. This leads to a self-stabilization of the peak splitting making it robust against impurity scattering.

Furthermore, in the presence of the magnetic field, the anomalous self energy Σ^F is nonzero, even for the highly symmetric orientation $\alpha = \pi/4$. The reason is that the special reflection symmetry of the case $\alpha = \pi/4$ is broken by the direction of the current flow.

Bibliography

[1] P. G. De Gennes, *Superconductivity of Metals and Alloys*, W. A. Benjamin, Inc. New York, 1966.

[2] D. A. Ivanov, *Phys. Rev. Lett.*, **86**, 268 (2001). Non-Abelian Statistics of Half-Quantum Vortices in p-Wave Superconductors.

[3] J. D. Sau, R. M. Lutchyn, S. Tewari, and S. Das Sarma, *Phys. Rev. Lett.*, **104**, 040502 (2010). Generic New Platform for Topological Quantum Computation Using Semiconductor Heterostructures.

[4] J. Alicea, *Phys. Rev. B*, **81**, 125318 (2010). Majorana Fermions in a Tunable Semiconductor Device.

[5] M. Duckheim and P. W. Brouwer, *Phys. Rev. B*, **83**, 054513 (2011). Andreev Reflection from Noncentrosymmetric Superconductors and Majorana Bound-State Generation in Half-Metallic Ferromagnets.

[6] Y. Tsutsumi, T. Kawakami, T. Mizushima, M. Ichioka, and K. Machida, *Phys. Rev. Lett.*, **101**, 135302 (2008). Majorana Bound State in Rotating Superfluid 3 He-A between Parallel Plates.

[7] B. Dora, M. Gulacsi, and P. Sodano, *Phys. Status Solidi PRL*, **3**, 169 (2009). Majorana Zero Modes in Graphene with Trigonal Warping.

[8] C.-R. Hu, *Phys. Rev. Lett.*, **72**, 1526 (1994). Midgap Surface States as a Novel Signature for $d_{x_a^2-x_b^2}$-Wave Superconductivity.

[9] Y. Tanaka and S. Kashiwaya, *Phys. Rev. Lett.*, **74**, 3451 (1995). Theory of Tunneling Spectroscopy of d-Wave Superconductors.

[10] L. J. Buchholtz, M. Palumbo, D. Rainer, and J. A. Sauls, *J. Low Temp. Phys.*, **101**, 1079 (1995). Thermodynamics of a d-Wave Superconductor near a Surface .

[11] S. Kashiwaya and Y. Tanaka, *Rep. Prog. Phys.*, **63**, 1641 (2000). Tunnelling Effects on Surface Bound States in Unconventional Superconductors.

[12] M. Covington, M. Aprili, E. Paraoanu, L. H. Greene, F. Xu, J. Zhu, and C. A. Mirkin, *Phys. Rev. Lett.*, **79**, 277 (1997). Observation of Surface-Induced Broken Time-Reversal Symmetry in $YBa_2Cu_3O_7$ Tunnel Junctions.

[13] B. Chesca, M. Seifried, T. Dahm, N. Schopohl, D. Koelle, R. Kleiner, and A. Tsukada, *Phys. Rev. B*, **71**, 104504 (2005). Observation of Andreev Bound States in Bicrystal Grain-Boundary Josephson Junctions of the Electron-Doped Superconductor $La_{2-x}Ce_xCuO_{4-y}$.

[14] G. Deutscher, *Rev. Mod. Phys.*, **77**, 109 (2005). Andreev–Saint-James Reflections: A Probe of Cuprate Superconductors.

[15] M. Wagenknecht, D. Koelle, R. Kleiner, S. Graser, N. Schopohl, B. Chesca, A. Tsukada, S. T. B. Goennenwein, and R. Gross, *Phys. Rev. Lett.*, **100**, 227001 (2008). Phase Diagram of the Electron-Doped $La_{2-x}Ce_xCuO_4$ Cuprate Superconductor from Andreev Bound States at Grain Boundary Junctions (and references therein).

[16] U. Shigehiro, K. Satoshi, T. Norio, K. Masao, T. Yukio, and K. Koji, *J. Phys. Chem. Solids*, **59**, 2081 (1998). Scanning Tunnelling Spectroscopy of $YBa_2Cu_3O_{7-\delta}$ Thin Films.

[17] A. Abrikosov, L. Gorkov, and E. Dzyloshinsky, *Methods of the Quantum Theory of Fields in Statistical Physics*, Prentice-Hall, Englewood Vliffs, New Jersey, 1963.

[18] G. Rickayzen, *Green's Functions and Condensed Matter*, Academic Press Limited, 1988.

[19] Y. S. Barash, H. Burkhardt, and D. Rainer, *Phys. Rev. Lett.*, **77**, 4070 (1996). Low-Temperature Anomaly in the Josephson Critical Current of Junctions in *d*-wave Superconductors.

[20] M. S. Kalenkov, M. Fogelström, and Y. S. Barash, *Phys. Rev. B*, **70**, 184505 (2004). Two Regimes for Effects of Surface Disorder on the Zero-Bias Conductance Peak of Tunnel Junctions involving *d*-Wave Superconductors.

[21] A. Poenicke, Y. S. Barash, C. Bruder, and V. Istyukov, *Phys. Rev. B*, **59**, 7102 (1999). Broadening of Andreev bound states in $d_{x^2-y^2}$ superconductors.

[22] Y. Tanaka, Y. Tanuma, and S. Kashiwaya, *Phys. Rev. B*, **64**, 054510 (2001). Influence of Impurity Scattering on Tunneling Conductance in Normal-Metal–*d*-Wave Superconductor Junctions.

[23] M. Fogelström, D. Rainer, and J. A. Sauls, *Phys. Rev. Lett.*, **79**, 281 (1997). Tunneling into Current-Carrying Surface States of High- T_c Superconductors.

[24] M. Aprili, E. Badica, and L. H. Greene, *Phys. Rev. Lett.*, **83**, 4630 (1999). Doppler Shift of the Andreev Bound States at the YBCO Surface.

[25] R. Krupke and G. Deutscher, *Phys. Rev. Lett.*, **83**, 4634 (1999). Anisotropic Magnetic Field Dependence of the Zero-Bias Anomaly on In-Plane Oriented [100] $Y_1Ba_2Cu_3O_{7-x}$ In Tunnel Junctions.

[26] H. Walter, W. Prusseit, R. Semerad, H. Kinder, W. Assmann, H. Huber, H. Burkhardt, D. Rainer, and J. A. Sauls, *Phys. Rev. Lett.*, **80**, 3598 (1998). Low-Temperature Anomaly in the Penetration Depth of $YBa_2Cu_3O_7$ Films: Evidence for Andreev Bound States at Surfaces.

[27] S.-K. Yip and J. A. Sauls, *Phys. Rev. Lett.*, **69**, 2264 (1992). Nonlinear Meissner effect in CuO superconductors.

[28] D. Xu, S. K. Yip, and J. A. Sauls, *Phys. Rev. B*, **51**, 16233 (1995). Nonlinear Meissner Effect in Unconventional Superconductors.

[29] T. Dahm and D. J. Scalapino, *Appl. Phys. Lett.*, **69**, 4248 (1996). Theory of Microwave Intermodulation in a High T_c Superconducting Microstrip Resonator .

[30] T. Dahm and D. Scalapino, *J. Appl. Phys.*, **81**(4), 2002 (1997). Theory of Intermodulation in a Superconducting Microstrip Resonator.

[31] D. E. Oates, S.-H. Park, and G. Koren, *Phys. Rev. Lett.*, **93**, 197001 (2004). Observation of the Nonlinear Meissner Effect in YBCO Thin Films: Evidence for a *d*-Wave Order Parameter in the Bulk of the Cuprate Superconductors.

[32] G. Benz, S. Wünsch, T. Scherer, N. M., and W. Jutzi, *Physica C*, **356**, 122 (2001). Measured Temperature Dependence of the Intermodulation Product of Coplanar Waveguides with *s*- and *d*- Wave Superconductors.

[33] C. Iniotakis, T. Dahm, and N. Schopohl, *Phys. Rev. Lett.*, **100**, 037002 (2008). Effect of Surface Andreev Bound States on the Bean-Livingston Barrier in *d*-Wave Superconductors.

[34] T. Dahm and D. J. Scalapino, *Phys. Rev. B*, **60**, 13125 (1999). Nonlinear Current Response of a *d*-Wave Superfluid.

[35] M.-R. Li, P. J. Hirschfeld, and P. Wölfle, *Phys. Rev. Lett.*, **81**, 5640 (1998). Is the Nonlinear Meissner Effect Unobservable?

[36] T. Matsubara, *Prog. Theor. Phys.*, **14**, 351 (1955). A new Approach to Quantum-Statistical Mechanics.

[37] D. N. Zubarev, *Soviet Physics Uspekhi*, **3**, 320 (1960). Double-Time Green Functions in Statistical Physics.

[38] L. P. Gor'kov, *Sov. Phys. JETP*, **7**, 505 (1958). On the Energy Spectrum of Superconductors.

[39] L. P. Gor'kov, *Sov. Phys. JETP*, **36**, 1364 (1959). Microscopic Derivation of the Ginzburg-Landau Equations in the Theory of Superconductivity.

[40] N. Schopohl unpublished (2002).

[41] G. D. Mahan, *Many-Particle Physics*, Kluwer Academic / Plenum Publishers, New York, 2000.

[42] N. Kopnin, *Theory of Nonequilibrium Superconductivity*, Oxford University Press Inc., New York, 2001.

[43] R. D. Mattuck, *A Guide to Feynman Diagrams in the Many-Body Problem*, Second edition, Dover Publications (1992), an unabridged and unaltered republication of the work first published in 1967 by The McGraw-Hill Book Co., New York, New York, second ed., 1992.

[44] G. Eilenberger, *Z. Phys.*, **214**, 195 (1968). Transformation of Gorkov's Equation for Type II Superconductors into Transport-Like Equations.

[45] A. I. Larkin and N. Ovchinnikov, *Sov. Phys. JETP*, **28**, 1200 (1969). Quasiclassical Method in the Theory of Superconductivity.

[46] N. Schopohl, *arXiv:cond-mat/9804064 v1* (1998). Transformation of the Eilenberger Equation of Superconductivity to a Scalar Riccati Equation.

[47] N. Schopohl and K. Maki, *Phys. Rev. B*, **52**, 490 (1995). Quasiparticle Spectrum Around a Vortex Line in a *d*-wave Superconductor.

[48] P. W. Anderson, *J. Phys. Chem. Solids*, **11**, 26 (1959). Theory of Dirty Superconductors.

[49] K. Bruus, H. und Flensberg, *Many-Body Quantum Theory in Condensed Matter Physics: An Introduction*, Oxford University Press Inc., New York, 2004.

[50] N. Schopohl, *unpublished* (2003). Fermi Liquid Theory of the Vortex State in Metals and Alloys.

[51] T. Dahm, P. J. Hirschfeld, D. J. Scalapino, and L. Zhu, *Phys. Rev. B*, **72**, 214512 (2005). Nodal Quasiparticle Lifetimes in Cuprate Superconductors.

[52] A. Zare, A. Markowsky, T. Dahm, and N. Schopohl, *Physical Review B*, **78**, 104524 (2008). Modification of Born impurity scattering near the surface of d-wave superconductors and influence of external magnetic field.

[53] E. Abrahams and C. M. Varma, *Proc. Natl. Acad. Sci. U.S.A.*, **97**, 5714 (2000). What Angle-Resolved Photoemission Experiments Tell About the Microscopic Theory for High-Temperature Superconductors.

[54] L. Zhu et al., *Phys. Rev. B*, **70**, 214503 (2004). Elastic Forward Scattering in the Cuprate Superconducting State.

[55] T. Dahm, S. Graser, C. Iniotakis, and N. Schopohl, *Phys. Rev. B*, **66**, 144515 (2002). Spectrum of Low-Energy Excitations in the Vortex State: Comparison of the Doppler-Shift Method to a Quasiclassical Approach.

[56] W. H. Press, S. A. Teukolsky, W. T. Vetterling, and B. P. Flannery, *Numerical Recipes in C++* , Second edition, Cambridge University Press, 2002.

[57] A. Markowsky Der Meissner-Effekt in d-Wellen Supraleitern: Einfluß der gebundenen Andreev-Zustände bei E=0 Master's thesis, Institut für Theoretische Physik, Universität Tübingen, (2007).

[58] N. Schopohl and K. Scharnberg, *Solid State Commun.*, **22**, 371 (1997). Tunneling Density of States for the Two-Band Model of Superconductivity (and references therein).

[59] L. Fabrega, B. Martinez, J. Fontcuberta, X. Obradors, and S. Pinol, *Phys. Rev. B*, **46**, 5581 (1992). Critical Fields and Fundamental Lengths in a Superconducting Electron-Doped $Pr_1.85Ce_0.15CuO_{4-y}$ Single Crystal.

[60] A. Zare, T. Dahm, and N. Schopohl, *Phys. Rev. Lett.*, **104**, 237001 (2010). Strong Surface Contribution to the Nonlinear Meissner Effect in d-Wave Superconductors.

[61] K. Leong, J. Booth, and S. Schima, *IEEE Trans. Appl. Supercond.*, **15**, 3608 (2005). A current-Density Scale for Characterizing Nonlinearity in High-T_c Superconductors.

[62] G. Leibovitch, R. Beck, A. Kohen, and G. Deutscher, *arXiv:0901.1774v1* (2009). Bean-Livingston Barrier Enhancement on Nodal Surface of the d-Wave Superconductor $YBa_2Cu_3O_{7-x}$.

[63] This work is originally done by Thomas Dahm.

[64] A. Gumann *Mikroskopische Theorie Geometrischer Josephson-Kontakte* PhD thesis, Institut für Theoretische Physik, Universität Tübingen, (2009).

Acknowledgment

I would like to thank all people who have helped and inspired me during my doctoral study.

First of all I want to thank Prof. Dr. Nils Schopohl for offering me the chance to perform this thesis, for his guidance and for his permanent readiness to help. I am deeply indebted to Prof. Dr. Thomas Dahm whose ceaseless support and well-founded advice aided me throughout my thesis. Without the many fruitful discussions and valuable hints from both it would not have been possible to complete this work.

Furthermore, I thank my colleagues Dr. Andreas Gumann and Alexander Markowsky for useful remarks and a pleasant working atmosphere. Special thanks go to Alexander Markowsky for proofreading my manuscript.

I want to thank all group members for creating such an agreeable and productive work environment.

I express my deepest gratitude to my family for their continuous love and support throughout my life.